Study of coexistence/competition of long-range orders in hard-core-boson systems

By

Amrita Ghosh

Enrolment No.: PHYS05201204020

Saha Institute of Nuclear Physics
Kolkata

A thesis submitted to the
Board of Studies in Physical Science Discipline
In partial fulfillment of requirements
For the Degree of
DOCTOR OF PHILOSOPHY
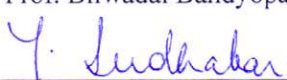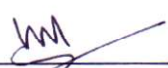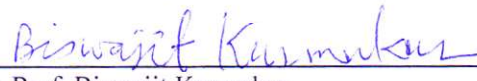*of*
HOMI BHABHA NATIONAL INSTITUTE

March, 2018

Homi Bhabha National Institute

Recommendations of the Viva Voce Committee

As members of the Viva Voce Committee, we certify that we have read the dissertation prepared by Amrita Ghosh entitled "Study of coexistence/competition of long-range orders in hard-core-boson systems" and recommend that it may be accepted as fulfilling the thesis requirement for the award of Degree of Doctor of Philosophy.
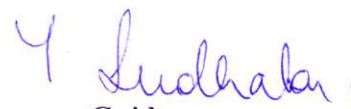
Chairman - Prof. Bilwadal Bandyopadhyay	Date: 22/06/2018
Guide / Convener - Prof. Sudhakar Yarlagadda	Date: 22/6/18
Examiner - Prof. Vijay B. Shenoy	Date: 22 June 2018
Member 1- Prof. Pradeep Kumar Mohanty	Date: 22/06/2018
Member 2- Prof. Biswajit Karmakar	Date: 22/06/18

Final approval and acceptance of this thesis is contingent upon the candidate's submission of the final copies of the thesis to HBNI.

I hereby certify that I have read this thesis prepared under my direction and recommend that it may be accepted as fulfilling the thesis requirement.

Date: 22/6/18

Place: kolkata

Guide

STATEMENT BY AUTHOR

This dissertation has been submitted in partial fulfillment of requirements for an advanced degree at Homi Bhabha National Institute (HBNI) and is deposited in the Library to be made available to borrowers under rules of the HBNI.

Brief quotations from this dissertation are allowable without special permission, provided that accurate acknowledgement of source is made. Requests for permission for extended quotation from or reproduction of this manuscript in whole or in part may be granted by the Competent Authority of HBNI when in his or her judgment the proposed use of the material is in the interests of scholarship. In all other instances, however, permission must be obtained from the author.

AMRITA GHOSH

DECLARATION

I, hereby declare that the investigation presented in the thesis has been carried out by me. The work is original and has not been submitted earlier as a whole or in part for a degree / diploma at this or any other Institution / University.

AMRITA GHOSH

LIST OF PUBLICATIONS ARISING FROM THE THESIS

Peer reviewed journals:

1. "Analysis of the $t_2 - V$ model"

   A. Ghosh and S. Yarlagadda

   Physical Review B **90**, 045140 (2014)

2. "Study of long-range orders of hard-core bosons coupled to cooperative normal modes in two-dimensional lattices"

   A. Ghosh and S. Yarlagadda

   Physical Review B **96**, 125108 (2017)

3. "Study of supersolidity in the two-dimensional Hubbard-Holstein model"

   A. Ghosh, S. Kar and S. Yarlagadda

   Accepted in EPJB [arXiv:1803.03174]

OTHER PUBLICATIONS

a. Book/Book Chapters: NIL

b. Conference/Symposium:

1. **Poster presentation** titled "Study of long-range orders due to cooperative breathing mode in two dimensions" at "Conference: What about U? - Effects of Hubbard Interactions and Hund's Coupling in Solids"
   Held at ICTP, Trieste, Italy, from 17 October 2016 to 21 October 2016.

2. **Poster presentation** titled "Study of long-range orders of hard-core bosons coupled to cooperative normal modes in two-dimensional lattices" at "School and Conference on Frustrated Magnetism"
   Held at IMSc, Chennai, India, from 3 April 2017 to 12 April 2017.

AMRITA GHOSH

To My Loving Family.......

ACKNOWLEDGEMENTS

I always thought that this would be the easiest part of the thesis. But now that I have started writing, I don't know where to start.

Firstly, I would like to thank my supervisor, Prof. Sudhakar Yarlagadda for introducing me to this field of research. Most of the things that I have learned in this period was through discussions with my guide and group members - Satyaki da, Ravindra bhaiya, Amit da and Sanjukta. A special thanks goes to Kausik da for his constant help regarding the computational facilities of our division. I acknowledge the Department of Atomic Energy (DAE), Government of India for the financial support and Saha Institute of Nuclear Physics for the infrastructure during my Ph.D. tenure.

I am blessed with the best family one can ever have. My family supported me whole-heartedly through every decision I took and provided me with the inspiration and motivation to carry on, even in the worst possible situation. My mother is the person with whom I share every minute detail of my life. In fact, it was my mother's dream for me to pursue higher studies and I am happy that I am fulfilling that. Whenever I was in distress, my father gave me the strength to lift myself by sharing the experiences of his own Ph.D. life. I share a very special connection with Didi and no matter what, she is always proud of me. Bivas da, I know you are not much expressive but I am lucky to have your support all the time. Finally, the tiniest yet most important part of my life, Kuhu; you are my joy, my love, you are the cure for all my troubles.

My friends always have been a integral part of my life. Krittika, sometimes I think what would I have done without you. Its your unconditional love and confidence in me that has made me the person I am today. I am extremely lucky and proud to have a wonderful friend

like you through all ups and downs. Pinaki and Bhai (Debashis), although time has taken us to different places, whenever I needed, you were always there for me. In spite of your own busy Ph.D. lives, you two have always given me the strength to overcome the hurdles, whether academic or personal.

While leaving Santiniketan, I never thought that I could make any friend in this professional environment. But to my surprise, the deep friendship that tied our entire Post M.Sc. batch made the professional journey a fun ride. The tours, picnics, movies, dinners and long addas with you guys, is something I will cherish all my life.

You can never describe the fun of a hostel life to someone who has not experienced it. Bini, Suvankar, Tirtha, Sanjukta, Aritra, Sabuj, Chiru, Kuntal - you all have made my first hostel experience extra special. All those midnight addas, birthday parties, boat-rides in Princep Ghat, late night movies, dumb charades, Dixit, Saraswati Puja, Holi, Diwali, new year parties and many more countless memories will remain etched in my heart forever.

My Ph.D. experience would have been incomplete if not for the people of Room No. 445. Sabya da, Sudip, Sanjukta, Sourav da and myself were a gang and we had a lot of fun. I will miss those jokes and lively discussions over almost every topic of the world.

Finally, the person who has truly played the most important role in the last five years in all aspects, is my partner Mugdha. I guess it is normal to expect one's partner to be supportive, but you have literally lived the good and bad times with me. Whenever I struggled, whether with the smallest bug in my code or an important decision of my life, you have always helped me even at the cost of your own work. I can not believe how could someone be so understanding. Without you, this day would not have been possible.

Amrita Ghosh

CONTENTS

SYNOPSIS

In condensed matter physics, understanding the ground state of an interacting many body system is one of the most challenging and non-trivial task. In band theory, instead of taking the interactions explicitly, the electrons are assumed to move in a periodic potential created by the ions and other electrons. Thus the many body effect is taken as an averaged background to which a single electron responds. Despite this simple approach, band theory has been successful in describing the metallic and insulating properties of many real systems, until the transition-metal oxides, with partially-filled 3d bands, showed significant disagreement with it. Later on, it was pointed out that the disregard of strong Coulomb repulsion between the d-electrons caused the failure of band theory. Fermi liquid theory, one of the most successful theories in condensed matter physics, was based on Landau's idea that in a non-interacting Fermi gas, turning on the interactions slowly would transform its ground state into a ground state of an interacting system. However, this theory failed to explain the low lying excitations of one-dimensional systems, demonstrating the importance of dimensionality in determining the ground state of a system.

Since then a number of analytical approaches have been applied to tackle systems of interacting electrons. Due to the non-availability of any analytic solution for most of the

problems, immense effort has gone into the development of various numerical approaches. A number of numerical techniques are available, applicable to different types of problems, but each of them has its own advantages and disadvantages. For example, very large system sizes can be accessed using density matrix renormalization group (DMRG) technique; but the method works well in one dimension. Quantum Monte Carlo (QMC) is a very powerful method to handle large system sizes; but unfortunately comes with a "sign problem" in case of fermions. On the other hand, exact diagonalization (ED) methods can give accurate results; however they can not handle large systems. Therefore, a complete theoretical understanding of the ground state properties of a strongly correlated system is still a challenge.

In strongly correlated systems, the electron-phonon (e-ph) interaction plays an important and interesting role. On one hand, at low temperatures, e-ph interaction is the main reason behind the formation of Cooper pairs which give rise to low temperature superconductivity; whereas at high temperatures, the same interaction is responsible for electrical resistivity in metals. Electron-phonon interaction is also responsible for a very peculiar feature of one-dimensional metals, first pointed out by Rudolf Peierls in 1930 [1]. Even in the presence of a weak e-ph coupling, a one-dimensional metal undergoes a spontaneous lattice distortion, thereby opening up a gap in the single particle energy dispersion curve at Fermi wave vector k_F. The formation of this gap is associated with the formation of charge modulation with period $2k_F$, known as the charge-density-wave (CDW). The presence of the gap in the energy dispersion curve makes the CDW an insulating state.

A new fascinating phenomenon, called supersolidity [2], has intrigued many researchers since its first theoretical prediction. Supersolidity is defined as the homogeneous coexistence of CDW and superfluidity. The situation may appear puzzling because CDW is an insulating state of solid phase; whereas superfluidity is a special property of some liquids

where the constituent atoms (or molecules) flow together without any friction. The first question that then comes to one's mind is that how can these two order parameters coexist in a single phase. The basic idea behind this unusual situation can be understood as follows. The constituent atoms (or molecules) of a classical liquid move in a random fashion, making the liquid viscous. However, in a superfluid the atoms move coherently forming a macroscopic wave of matter. As a consequence, a superfluid kept in a slowly rotating bucket does not rotate with the walls of the bucket, rather stays at rest. In a classical solid, the particles are localized at different sites. Kept in a rotating box, a classical solid is forced to rotate with its walls. On the other hand, quantum solids portray quite a different picture. The particles in a quantum solid fluctuate around their mean positions and vacancies can be created in the system. Now, these vacancies can eventually exchange positions with the particles by hopping to neighboring sites. If this exchange does not cost energy, then the vacancies can flow with the solid maintaining its overall structure. If somehow this flow becomes a superflow, we can have a solid with a part of it being a superfluid; thus, a supersolid is realized.

The homogeneous coexistence of superfluidity and crystalline order in continuous space is referred as continuous-space supersolidity. In this case the lattice constant can be adjusted continuously. In 2004, the first experimental claim for the observation of continuous-space supersolidity in helium-4 was made by Kim and Chan [3]. Despite the controversies created, it certainly enhanced the debate and interest in understanding this new phase among the researchers. On the other hand, lattice-supersolidity is defined as the the single-phase coexistence of superconductivity/superfluidity and CDW realized in discrete lattices. A wide variety of systems in three dimensions (such as doped $BaBiO_3$ [4, 5]), quasi-two dimensions (for example the layered dichalcogenides [6] and molecular crystals [7]) and quasi-one dimension (such as doped trichalcogenide $NbSe_3$ [8] and doped

spin ladder $Sr_{14}Cu_{24}O_{41}$ [9, 10]) display this novel phenomenon. While phenomenological pictures exist [4, 11] to explain lattice-supersolidity, a microscopic theory that explains the homogeneous coexistence has been elusive.

As far as the artificially engineered systems are concerned, cold bosonic atoms in optical lattices emerge as potential candidates for realizing lattice-supersolid phases. In fact only recently, supersolidity was experimentally produced in an optical lattice inside an optical cavity with effective long-range interactions generated by a vacuum mode of the cavity [12]. On the theoretical side, a number of bosonic models have produced lattice supersolidity in two-dimensional (2D) square [13–22], triangular [23–29] and honeycomb lattices [30, 31] as well as in a one-dimensional lattice [32, 33].

As suggested by the title, the main purpose of this thesis is to study the possible manifestations of long-range orders, including lattice-supersolid phases with differently broken symmetry in hard-core-boson (HCB) models (which are the effective Hamiltonian for systems with strong HCB-phonon or e-ph coupling) and understand the underlying mechanism.

Many oxides with the formula ABO_3 assume perovskite structure and involve strong e-ph interaction. In these systems a common oxygen atom is shared by two adjacent BO_6 octahedra. As a result, the octahedral distortions are of cooperative nature rather than being independent. For example, in barium bismuthate ($BaBiO_3$), only the $6s$ electrons are responsible for the transport properties and produce a single normal mode distortion: the breathing mode. In this mode, the oxygen atoms along all the three axes of the BiO_6 octahedra either move outwards or inwards together, thereby mimicking the breathing process. Moreover, the evidence of strong e-ph interaction for pure $BaBiO_3$ is clear from the observation of 10% change in the $Bi - O$ bond length [34]. Because the 6s electrons are the only ones taking part in transport, $BaBiO_3$ can be described as a one-band 3D cooperative

breathing mode (CBM) model. Furthermore, the lattice vibrations in a copper oxide plane of a parent cuprate compound can be described as a one-band (with the orbitals centered on the copper sites) two-dimensional CBM system [35, 36]. In the C-type antiferromagnetic region of the phase diagram of a two-band Jahn-Teller (JT) manganite system (such as $0.65 \leqslant x \leqslant 0.9$ for $La_{1-x}Sr_xMnO_3$ [37]), each ferromagnetic C-chain can be viewed as a one-band (d_{z^2} orbital) one-dimensional CBM system, where the neighboring C-chains are coupled antiferromagnetically.

An important point to note here is that in the case of weak e-ph interaction, a Migdal-type of perturbative treatment can be used; whereas with strong e-ph interaction, even the one-band system needs a nonperturbative approach [38]. In the first two problems of this thesis, we concentrate on the non-adiabatic regime ($t/\omega_0 \leqslant 1$) and strong-coupling region (large g^2), where t is the coefficient of NN hopping, ω_0 is the optical-phonon frequency and g denotes the HCB-phonon interaction strength. To produce an effective polaronic Hamiltonian, a duality transformation is employed which transforms the strong-coupling problem in the original frame of reference [with small parameter $\propto (g\omega_0)/t$] into a weak-coupling problem in a dual frame of reference [with small parameter $\propto t/(g\omega_0)$, i.e., inverse of the small parameter in the original frame of reference]. To achieve the above end, we have modified the Lang-Firsov transformation so as to take into account the cooperative nature of the distortions. The transformed Hamiltonian can then be written as a sum of the unperturbed Hamiltonian and a perturbative term. Using the eigenstates of the unperturbed Hamiltonian, we perform a non-trivial perturbation theory upto second order and get the effective Hamiltonian.

In Ref. [39], starting with an one-band one dimensional system of spinless electrons, where two neighboring electrons are coupled to the in-between oxygen atom via CBM, it was shown that the dominant transport mechanism of the system changes from nearest-

neighbor (NN) hopping to the next-nearest-neighbor (NNN) one. Furthermore, due to incompatibility of distortions produced by cooperative e-ph interaction effects, the NN repulsion between the particles becomes significant, leading to the $t_2 - V$ model as the effective model. In one dimension, using Jordan-Wigner transformation, one can always map the spinless electrons in terms of HCBs. In the first problem of this thesis [40], the $t_2 - V$ model in terms of HCBs has been studied using analytical and numerical approaches. We demonstrate that upon tuning the strength of the NN repulsion, the $t_2 - V$ model manifests a dramatic discontinuous transition from a superfluid to either a CDW or a supersolid. Using Green's function analysis, the exact critical values of the repulsion V_c are obtained for two limiting cases: the two HCB case and the half-filled system. At intermediate fillings, using finite-size scaling analysis, we obtain the V_c values numerically, where a modified version of Lanczos method [41] is used. Furthermore in this study, topological inequivalence of rings with even and odd number of sites is also demonstrated through the differences in the peak value of the structure factor at the transition. Our study shows that, compared to the noncooperative situation, cooperative e-ph interaction produces strikingly different physics. We hope that in the future the Greens function technique used in our study to solve the two limiting cases of the $t_2 - V$ model analytically, will lead to useful approaches to handle more complex problems.

An important member of the valence disproportionated material class is $BaBiO_3$, where the Bi ion, with the electronic configuration $[Xe]4f^{14}5d^{10}6s^26p^3$, displays $3^+(6s^2)$ and $5^+(6s^0)$ valence states, skipping the intermediate 4^+ valence state. Pure $BaBiO_3$ is an insulator with alternate $6s^2$ and $6s^0$ ions forming a CDW, which can be thought of as a system of HCBs occupying alternate sites and coupled to the CBM [42]. Inspired by the doped bismuthate systems, in the next problem [43] of this thesis, we study a 2D system of HCBs in a 2D perovskite lattice, governed by the CBM. At strong HCB-phonon cou-

pling, the effective Hamiltonian is shown to involve NN, NNN, and next-to-next-nearest -neighbor (NNNN) hoppings and repulsions in the form of an extended-boson-Hubbard model $t_1 - t_2 - t_3 - V_1 - V_2 - V_3$. Using QMC simulation employing the stochastic-series-expansion (SSE) technique [44], we construct the phase diagram of the system. Our study shows that with the increase of the coupling strength, the system undergoes a first-order quantum phase transition from a superfluid to a checkerboard solid at half filling and from a superfluid to a diagonal striped solid at one-third filling. Away from these commensurate fillings, checkerboard supersolid is observed near half filling; whereas a rare diagonal striped supersolid is realized in the vicinity of one-third filling. Even though diagonal stripes have been observed in systems such as $La_{2-x}Sr_xNiO_4$ (LSNO) at $x = 1/3$ hole doping [45–51] and predicted theoretically in a lattice gas model with long-range interactions at one-third filling [52], so far the corresponding diagonal striped supersolid (dsSS) has been elusive on a square lattice (that is not subject to an external potential). In this study we identify the $t_1 - V_1 - V_2 - V_3$ model as the minimum model for the diagonal striped supersolid. It is also shown that the charge orders in LSNO can be studied by extending our cooperative HCB-phonon framework. We demonstrate that the diagonal-stripe and checkerboard order observed in LSNO at one-third filling and half filling respectively, can be explained by invoking cooperative Jahn-Teller effect, which resolves a longstanding controversy.

To understand the interplay of electron-electron (e-e) and e-ph interactions, the well-known Hubbard-Holstein model has been studied extensively in one, two and infinite dimensions at various fillings by employing several approaches. In Refs. [53] and [54], a controlled analytic approach (taking the dynamical phonons into account) was applied to the one-dimensional Hubbard-Holstein model in the regimes of strong e-ph coupling ($g > 1$) and strong Coulomb coupling ($U/t > 1$) with U being the onsite Coulomb re-

pulsion between electrons. The model was shown to manifest a correlated singlet phase over a range of U/t values. Concentrating only on this singlet phase, in the last problem of this thesis [55], we study the two-dimensional version of the Hubbard-Holstein model. Now, an important point to note here is that, each NN singlet can be represented as a HCB located at its center. Thus the system of NN singlets on a periodic square lattice transforms into a system of HCBs on a checkerboard lattice governed by a Hamiltonian of the form $t_1 - V_1 - V_2 - V_3$. By investigating the checkerboard lattice at various filling fractions of HCBs, we show (using SSE method) that, in contrast to the one-dimensional results where CDW and superfluidity occur mutually exclusively, a supersolid phase exists on both sides of the CDW observed at $1/8$ filling fraction. Thus our results portray the importance of dimensionality in determining the properties of a system. There have been a number of studies which deal with HCBs on a checkerboard lattice. But the unique feature which distinguishes our model from the myriad models is that, due to the presence of the correlated singlet phase, the checkerboard lattice naturally emerges out of a system of electrons on a periodic square lattice.

Lastly, it is worth mentioning that in our models the parameters [i.e., hopping term, strength of HCB-phonon (e-ph) coupling, and phonon frequency] either can be determined from band-structure calculations or can be obtained from experiments; this sets them apart from the existing lattice models of the extended-boson-Hubbard type. We hope that the works presented in this thesis will shed some light on the mechanism behind the formation of different types of CDWs as well as lattice-supersolids.

LIST OF FIGURES

xiii

LIST OF TABLES

ANALYSIS OF THE $t_2 - V$ MODEL

2.1 Introduction

The last few decades have witnessed numerous studies to fathom the tapestry of exotic phenomena (such as long-range orderings) and interesting functionalities (such as colossal magnetoresistance, multiferroicity, superconductivity, etc.) [81] in bulk transition metal oxides (such as the manganites, cuprates, etc.) and their interfaces. Of considerable interest is the coexistence of diagonal long-range orders [such as the CDW, spin-density-wave (SDW) and orbital-density-wave (ODW) in manganites [82]]; also of immense focus is the coexistence and competition between long-range orders that are diagonal (i.e., CDW or SDW) and off-diagonal (i.e., superconductivity or superfluidity) such as those reported in bismuthates [5], cuprates [9, 10], etc.

To model the emergent ordering and functionality in these complex metal oxides (and guide material synthesis), one needs, as building blocks, effective Hamiltonians for various interactions. Except for the cooperative electron-phonon interaction (EPI), effective Hamil-

tonians, that reasonably mimic the physics, have been derived for all other interactions. For instance, double exchange model approximates infinite Hund's coupling, Gutzwiller approximation or dynamical mean-field theory model Hubbard on-site Coulombic interaction, superexchange describes localized spin interaction at strong on-site repulsion, etc. Many oxides such as cuprates [83–85], manganites [86–88], and bismuthates [34] indicate cooperative strong EPI.

Although definite progress has been made long ago in numerically treating EPI systems [82], only recently has the effective Hamiltonian been derived for the cooperative EPI quantum systems in one-dimension; it has been demonstrated analytically that introducing cooperative effects in the strong EPI limit changes the dominant transport mechanism from one of nearest-neighbor (NN) hopping to that of next-nearest-neighbor (NNN) hopping [39]. Additional NN particle repulsion (due to incompatibility of distortions produced by cooperative EPI effects) leads to the $t_2 - V$ model as the effective model.

The purpose of this work is to study the $t_2 - V$ model and elucidate the consequences of the atypical dominant (NNN) transport mechanism in cooperative strong EPI systems. We demonstrate that the $t_2 - V$ model, upon tuning repulsion, displays a dramatic discontinuous transition from a superfluid to either a CDW or a supersolid wherein the superfluid and the CDW coexist instead of compete. Green's function analysis yields exact critical repulsion values V_c in the two limiting cases; we find $V_c/t_2 = 4$ for the two hard-core-boson (HCB) case and $V_c/t_2 = 2\sqrt{2}$ for the half-filled system. Using finite size scaling analysis, we also obtain V_c values numerically at intermediate fillings. The symmetry difference between rings with odd number of sites (o-rings) and rings with even number of sites (e-rings) is revealed through the ratio of their structure factor peaks at transition being an irrational number $4/\pi^2$.

2.2 Numerical study of the $t_2 - V$ model for e-rings

We begin by identifying the Hamiltonian of the $t_2 - V$ model for HCBs.

$$H_{t_2V} \equiv -t_2 \sum_{j=1}^{N_s} (b_{j-1}^\dagger b_{j+1} + \text{H.c.}) + V \sum_{j=1}^{N_s} n_j n_{j+1}, \qquad (2.1)$$

where b_j is the destruction operator for a HCB, $V \geq 0$, $n_j = b_j^\dagger b_j$, and N_s is the total number of sites. We assume periodic boundary conditions and first study numerically (using modified Lanczos algorithm [41]) the quantum phase transition (QPT) in the $t_2 - V$ model. We will characterize the transition through the structure factor and the superfluid density. The structure factor is given by $S(k) = \sum_{l=1}^{N_s} e^{ikl} W(l)$ where $W(l)$ is the two-point correlation function for density fluctuations of HCBs at a distance l apart (when lattice constant is set to unity): $W(l) = \frac{4}{N_s} \sum_{j=1}^{N_s} [\langle n_j n_{j+l} \rangle - \langle n_j \rangle \langle n_{j+l} \rangle]$. The wavevector $k = \frac{2n\pi}{N_s}$ with $n = 1, 2, ..., N_s$; filling-fraction f $\equiv \langle n_j \rangle = \frac{N_p}{N_s}$ with N_p being the total number of HCBs in the system. For e-rings with $N_s = 2N$ sites, from the definition of the structure factor, for $k = \pi$ we have

$$S(k) = \sum_{l=1}^{2N} (-1)^l W(l). \qquad (2.2)$$

Substituting the expression for the correlation function $W(l)$ and recognizing that $\sum_{l=1}^{2N} e^{i\pi l} = 0$, we get

$$S(k) = \frac{4}{2N} \sum_{j=1}^{2N} \left\langle n_j \sum_{l=1}^{2N} n_{j+l} (-1)^l \right\rangle. \qquad (2.3)$$

51

In the above equation, on taking $j + l = m$ we get

$$S(k) = \frac{2}{N} \sum_{j=1}^{2N} \left\langle n_j(-1)^j \sum_{m=1}^{2N} n_m(-1)^m \right\rangle. \tag{2.4}$$

On defining the number operator which gives the total number of HCBs at even (odd) sites as $\hat{N}_e = \sum_{j \text{even}} n_j$ ($\hat{N}_o = \sum_{j \text{odd}} n_j$), we obtain

$$S(\pi) = \frac{2\langle (\hat{N}_e - \hat{N}_o)^2 \rangle}{N}. \tag{2.5}$$

Due to the presence of only next-nearest-neighbor hopping, both $\hat{N}_e$ and $\hat{N}_o$ commute with the $t_2 - V$ Hamiltonian; hence we obtain the following result

$$S(\pi) = \frac{2(N_e - N_o)^2}{N}, \tag{2.6}$$

where N_e (N_o) are the total number of HCBs at even (odd) sites. Thus the minimum value of $S(\pi) = 0$ corresponds to equal number of particles in both the sublattices whereas the maximum is given by

$$[S(\pi)]_{\max} = \frac{2N_p^2}{N} = \frac{4N_p^2}{N_s}, \tag{2.7}$$

indicating a single sublattice occupancy. To study the QPT, we rescale the value of $S(\pi)$ as $S^*(\pi) = \frac{S(\pi)}{[S(\pi)]_{\max}}$ with $S^*(\pi)$ representing the order parameter that varies from 0 to 1 during the phase transition.

Next, we will outline our procedure for calculating the superfluid density by threading

52

the chain with an infinitesimal magnetic flux θ. The superfluid fraction is given by [21, 89]

$$\rho_s = \frac{N_s^2}{N_p t_{eff}} \left[\frac{1}{2} \frac{\partial^2 E(\theta)}{\partial \theta^2} \right]_{\theta=0}, \tag{2.8}$$

where $E(\theta)$ is the total energy when threaded by flux θ and $t_{\text{eff}} = \hbar^2/2m$ is the effective hopping term which for our $t_2 - V$ model is given by $t_{\text{eff}} = 4t_2$.

The total energy for the case $V > V_c$, when threaded by a flux θ, is expressed as

$$E(\theta) = -2t_2 \sum_k \cos[2(k + \theta/N_s)], \tag{2.9}$$

where $N_s = 2N$. Then, from the above definition of superfluid density ρ_s, for $V > V_c$, we have

$$\rho_s = \frac{1}{N_p} \sum_k \cos(2k). \tag{2.10}$$

Since we consider even values of N_p, the momenta occupied by the HCBs are $k = \frac{(2m+1)\pi}{2N}$ with $-\frac{N_p}{2} \leq m \leq \frac{N_p}{2} - 1$. Summing over these momenta, for the case of single sublattice occupancy (which occurs when $V > V_c$), we have from expression (2.10)

$$\rho_s = \frac{1}{N_p} \frac{\sin\left(\frac{\pi N_p}{N}\right)}{\sin\left(\frac{\pi}{N}\right)}. \tag{2.11}$$

When both the sublattices are equally occupied (i.e., for $V = 0$), in each sublattice of N sites we have $\frac{N_p}{2}$ particles. Thus, the superfluid density in this case takes the form

$$\rho_s = \frac{2}{N_p} \frac{\sin\left(\frac{\pi N_p}{2N}\right)}{\sin\left(\frac{\pi}{N}\right)}. \tag{2.12}$$
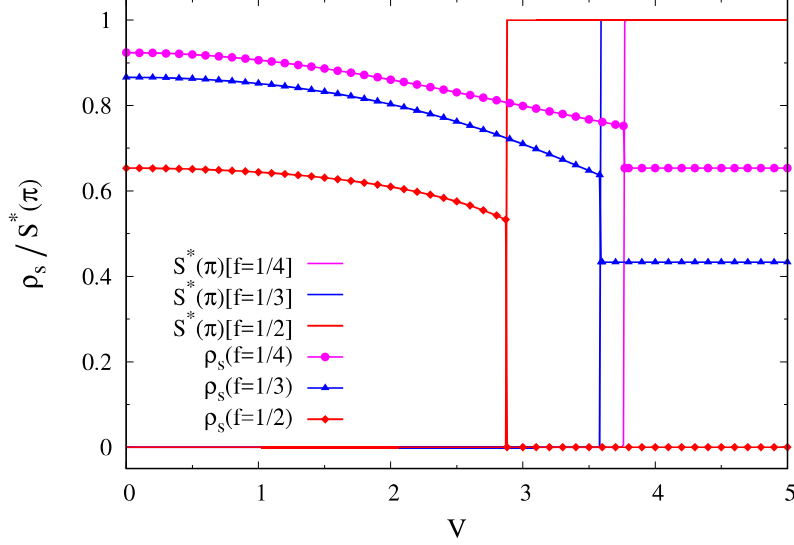
Figure 2.1: Plots of rescaled structure factor $S^*(\pi)$ and superfluid fraction ρ_s at various filling factors f obtained using modified Lanczos technique. The calculations were at f = $1/2, 1/4$ with system size $N_s = 16$ and at f = $1/3$ with $N_s = 12$. At a critical repulsion there is a striking discontinuous transition in both $S^*(\pi)$ and ρ_s; while $S^*(\pi)$ jumps from its minimum to maximum, there is a significant drop in ρ_s.

When e-rings were used, at all fillings f, we found that the order parameter $S^*(\pi)$ jumps from 0 to 1 at a critical value of repulsion V_c indicating that the system transits from equally populated sublattices (i.e., Ising symmetry) case to a single sublattice occupancy, i.e., a period-doubling CDW state [see Fig. 2.1]. Concomitantly, as can be seen from Fig. 2.1, there is a sudden drop in the superfluid fraction ρ_s at the same critical repulsion. At half-filling, where the superfluid fraction vanishes above a critical repulsion because a single sublattice is completely filled, the transition shows that superfluidity and CDW state are mutually exclusive. On the other hand, at all non-half-fillings, we see that the system undergoes a QPT from a superfluid to a supersolid (i.e., a homogeneously coexisting superfluid and CDW) state. In Fig. 2.1, it is of interest to note that the values of ρ_s at $V = 0$ and $V > V_c$ are exactly those predicted by Eq. (2.11) and Eq. (2.12), respectively. Next, for

54
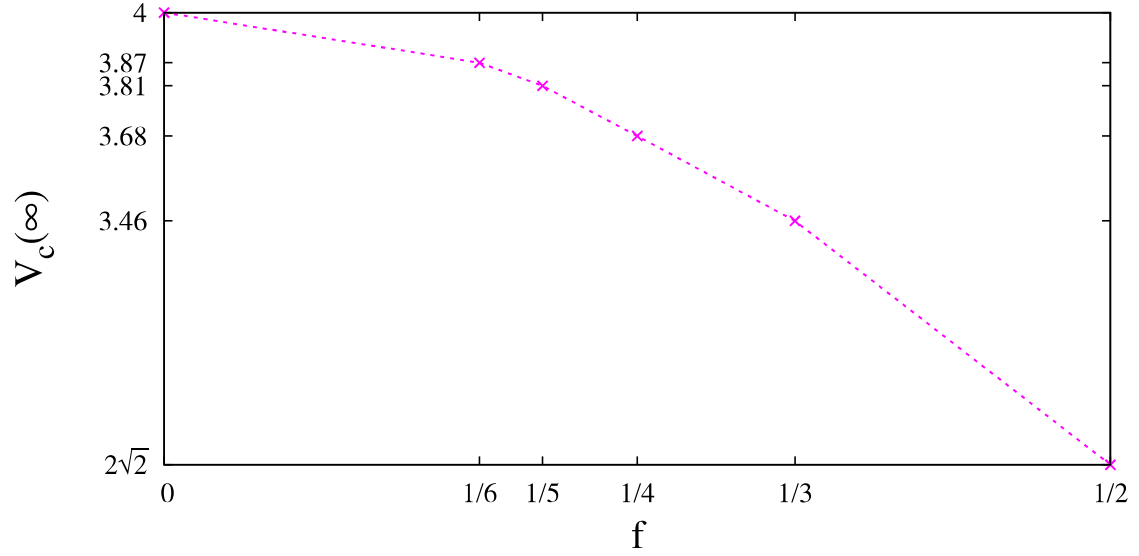
Figure 2.2: Plot of $V_c(\infty)$ (critical repulsion for an infinite system) obtained from Green's function analysis for half-filled (f = 1/2) and two HCB systems (f $\to$ 0) and from finite size scaling at various other fillings f.

e-rings at various fillings, we relate $V_c(2N)$ (critical repulsion at $N_s = 2N$) to $V_c(\infty)$ using finite size scaling analysis (see Appendix A for details) and obtain Fig. 2.2. At half-filling, from finite size scaling analysis we obtain that $V_c(\infty) \approx 2.83$; in the next section, we show (using Green's function analysis) the exact result $V_c(\infty) = 2\sqrt{2}$. For systems with 2 HCB and $N_s = 4, 6, 8, 10, 12, 14, 16, 18$, and 20, we find numerically that $V_c \approx 4.00$; in the next section, we obtain the exact result (using Green's functions) that $V_c(2N) = 4$ for any system size $N_s = 2N \geq 4$.

2.3 Exact instability condition at half-filling in e-rings

We study the following $t_2 - V$ Hamiltonian in rings with even number of sites ($2N$) by considering two sublattices C and D and using periodic boundary conditions:

$$H \equiv -t_2 \sum_{i=1}^{N} (c_i^\dagger c_{i+1} + \text{H.c.}) - t_2 \sum_{i=1}^{N} (d_i^\dagger d_{i+1} + \text{H.c.}) + V \sum_{i=1}^{N} d_i^\dagger d_i (c_i^\dagger c_i + c_{i-1}^\dagger c_{i-1}),$$

(2.13)

where c and d denote destruction operators of HCBs in sublattices C and D, respectively.

To understand the discontinuous phase transition at half-filling, (i.e., the transition from equal occupation of both sublattices to occupation of only one sublattice at a critical V_c) we begin by recognizing that when the system is on the verge of completing the phase transition, the system will pass through the state where there is one HCB in one sublattice and one hole in the other sublattice. Hence, we now consider instability for the case of one particle in sublattice C and one hole [with destruction operator denoted by h ($\equiv d^\dagger$)] in sublattice D; we then rearrange the above equation as

$$H \equiv -t_2 \sum_{i=1}^{N} (c_i^\dagger c_{i+1} + \text{H.c.}) + t_2 \sum_{i=1}^{N} (h_i^\dagger h_{i+1} + \text{H.c.}) - V \sum_{i=1}^{N} (h_i^\dagger h_i - 1)(c_i^\dagger c_i + c_{i-1}^\dagger c_{i-1}).$$

(2.14)

We define the particle-hole Green's function as follows [90]:

$$g_n^h \equiv {}_h\langle k, 0 | G(\omega) | k, n \rangle_h,$$

(2.15)

56

where $G(\omega) \equiv 1/(\omega + i\eta - H)$ and $|k, n\rangle_h$ is the particle-hole state

$$|k, n\rangle_h = \frac{1}{\sqrt{N}} \sum_{j=1}^{N} e^{ik\left(j+\frac{n}{2}\right)} c_j^\dagger h_{j+n}^\dagger |0\rangle, \tag{2.16}$$

with k being the total momentum of the particle-hole system and n the separation between the particle and the hole. Using the condition

$$\delta_{0,n} \equiv {}_h\langle k, 0|G(\omega)(\omega + i\eta - H)|k, n\rangle_h, \tag{2.17}$$

for $n = 0$, we obtain

$$(\omega + i\eta)g_0^h = 1 + {}_h\langle k, 0|G(\omega)(H)|k, 0\rangle_h$$
$$= 1 + Vg_0^h - i2t_2 \sin(k/2)g_1^h + i2t_2 \sin(k/2)g_{-1}^h. \tag{2.18}$$

From Eq. (2.17), for $n = 1$, we get

$$(\omega + i\eta)g_1^h = {}_h\langle k, 0|G(\omega)(H)|k, 1\rangle_h$$
$$= Vg_1^h - i2t_2 \sin(k/2)g_2^h + i2t_2 \sin(k/2)g_0^h. \tag{2.19}$$

Similarly, for $n \neq 0, 1$, we derive

$$(\omega + i\eta)g_n^h = {}_h\langle k, 0|G(\omega)(H)|k, n\rangle_h$$
$$= 2Vg_n^h - i2t_2 \sin(k/2)g_{n+1}^h + i2t_2 \sin(k/2)g_{n-1}^h. \tag{2.20}$$

As V is increased to the critical repulsion V_c, the HCB in sublattice C vacates its sublattice and enters the sublattice D containing the hole; the energy of the system then becomes 0.

Next, we let

$$\frac{\omega + i\eta - 2V}{F_k} \equiv \frac{1}{z} - z, \tag{2.21}$$

where $F_k \equiv i2t_2 \sin(k/2)$. Then, Eq. (2.20) takes the simple form

$$\left(\frac{1}{z} - z\right) g_n^h = g_{n-1}^h - g_{n+1}^h, \tag{2.22}$$

whose solution is of the form

$$g_n^h = \alpha_1^\pm z^n + \frac{\beta_1^\pm}{(-z)^n}, \tag{2.23}$$

where α_1^+ (α_1^-) and β_1^+ (β_1^-) correspond to $n > 1$ ($n < 0$). The transition occurs at the critical value of V that makes the overall energy 0. Let $V = 2t_2\gamma \sin(k/2)$. The overall energy is less than $-4t_2 + 2V$ (for $V > 0$). It is important to note that, for the ground state, $k = \pi$ for any $V \leq V_c$. This can be seen by first noting that when $V = 0$, total momentum in the minimum energy state is π; next, turning on V does not change the total momentum. Then for $k = \pi$, to get overall energy to be 0, we need the inequality $\gamma > 1$. The instability condition corresponds to the case $\omega = 0$ because then the Green's function g_0^h diverges when the energy is zero. It then follows from Eq. (2.21) that

$$i2\gamma = \frac{1}{z} - z, \tag{2.24}$$

which implies that

$$z = i\left(-\gamma + \sqrt{\gamma^2 - 1}\right), \tag{2.25}$$

and hence $|z| < 1$ for $\gamma > 1$. Let us first consider the case $n > 1$. From the above Eq. (2.23), it is clear that, for $n \to \infty$, g_n^h is finite only for $\beta_1^+ = 0$. Thus for $n > 1$,

$$g_{n+1}^h = zg_n^h, \tag{2.26}$$

which implies that $g_3^h = zg_2^h$; then, from Eq. (2.22) it follows that

$$g_2^h = zg_1^h. \tag{2.27}$$

Next, for the case $n < 0$, we see that g_n^h is finite, for $n \to -\infty$, only when $\alpha_1^- = 0$. Thus for $n < 0$,

$$g_{n-1}^h = -zg_n^h, \tag{2.28}$$

which implies that $g_{-2}^h = -zg_{-1}^h$; then from Eq. (2.22) we obtain

$$g_{-1}^h = -zg_0^h. \tag{2.29}$$

From Eqs. (2.18), (2.19), (2.27), and (2.29), we obtain

$$g_0^h = \frac{1}{(\omega + i\eta - V + zF_k) + \frac{F_k^2}{(\omega + i\eta - V + zF_k)}}, \tag{2.30}$$

and

$$g_1^h = \frac{g_0^h F_k}{(\omega + i\eta - V + zF_k)}, \tag{2.31}$$

where $\omega = 0$, $V = 2t_2\gamma$, $z = i(-\gamma + \sqrt{\gamma^2 - 1})$, and $F_k = i2t_2$. It then follows that g_0^h

diverges when $(V - zF_k)^2 + F_k^2 = 0$, i.e., when $\gamma = \sqrt{2}$. Thus the instability condition is $V_c = 2\sqrt{2}t_2$. (We now see that the total energy at transition is indeed less than $-4t_2 + 2V$). It is important to note [as can be seen from Eq. (2.31)] that, when g_0^h diverges, g_1^h also diverges; consequently, from Eqs. (2.26), (2.28), and (2.29) we see that all g_n^h diverge (i.e., even when $n > 1$ and $n < 0$).

2.4   Exact instability condition for two HCBs in e-rings

We now study the non-trivial case of the two-HCB instability for the $t_2 - V$ Hamiltonian [described by Eq. (2.13)] in e-rings. We consider one HCB in sublattice C and one HCB in sublattice D; the corresponding two-particle Green's function is defined as $g_n \equiv \langle k, 0|G(\omega)|k, n\rangle$ with $G(\omega)$ being defined as before and the two-particle state $|k, n\rangle$ being expressed as

$$|k, n\rangle = \frac{1}{\sqrt{N}} \sum_{j=1}^{N} e^{ik\left(j + \frac{n}{2}\right)} c_j^\dagger d_{j+n}^\dagger |0\rangle, \tag{2.32}$$

with k representing the total momentum of the two-particle system. Then, the following equations hold for the Green's functions g_n:

$$(\omega + i\eta - V)g_0 = 1 - 2t_2 \cos(k/2)g_1 - 2t_2 \cos(k/2)g_{-1}, \tag{2.33}$$

$$(\omega + i\eta - V)g_1 = -2t_2 \cos(k/2)g_2 - 2t_2 \cos(k/2)g_0, \tag{2.34}$$

and for $n \neq 0, 1$

$$(\omega + i\eta)g_n = -2t_2 \cos(k/2)g_{n+1} - 2t_2 \cos(k/2)g_{n-1}. \tag{2.35}$$

60

As V increases to the critical V_c, the energy given by Eq. (2.13) becomes $-4t_2 \cos(\pi/N)$ (i.e., the minimum energy of the two HCBs in the same sublattice); this would correspond to the instability where one HCB quits its sublattice and goes into the sublattice of the other particle. Here, we make the key observation that $k = 0$ for the ground state at any V. To understand this, we first note for $V = 0$, the total momentum is zero in the minimum energy state; next, we recognize that turning on V does not change the total momentum. Now, to obtain the instability, we take

$$
\begin{aligned}
\frac{\omega}{(-2t_2)} &= \frac{4t_2 \cos(\pi/N)}{2t_2} = 2\cos(\pi/N) \\
&= e^{i\pi/N} + e^{-i\pi/N} \\
&= z + \frac{1}{z}.
\end{aligned}
\tag{2.36}
$$

We set $z = e^{i\pi/N}$ and also take $V/(2t_2) = 2\gamma$. Then, Eqs. (2.33), (2.34), and (2.35) become

$$
[(z + 1/z) + 2\gamma]g_0 = -1/(2t_2) + g_1 + g_{-1},
\tag{2.37}
$$

$$
[(z + 1/z) + 2\gamma]g_1 = g_2 + g_0,
\tag{2.38}
$$

and for $n \neq 0, 1$

$$
[(z + 1/z)]g_n = g_{n+1} + g_{n-1}.
\tag{2.39}
$$

Without loss of generality, we assume

$$
g_1 = \alpha_2 z + \beta_2/z,
\tag{2.40}
$$

and

$$g_2 = \alpha_2 z^2 + \beta_2/z^2. \tag{2.41}$$

Then using Eqs. (2.39), (2.40), and (2.41), we obtain for $n = 3, 4, ..., N$ the expression

$$g_n = \alpha_2 z^n + \beta_2/z^n. \tag{2.42}$$

It is important to recognize that $|z| = 1$; hence, the Green's functions do not decay with HCB separation n. Next, we note that at $k = 0$, $|k, -n\rangle = |k, N - n\rangle$; consequently, we see that $g_N = g_0$ and $g_{N-1} = g_{-1}$. Then, using Eq. (2.42) and the relation $z = e^{i\pi/N}$, we get

$$g_{-1} = g_{N-1} = \alpha_2 z^{N-1} + \beta_2/z^{N-1} = -(\alpha_2/z + \beta_2 z), \tag{2.43}$$

and

$$g_0 = g_N = \alpha_2 z^N + \beta_2/z^N = -(\alpha_2 + \beta_2). \tag{2.44}$$

We are now ready to solve for the Green's functions g_n using Eqs. (2.37), (2.38), (2.40), (2.41), (2.43), and (2.44). We get the following equations:

$$\alpha_2[z + \gamma] + \beta_2[1/z + \gamma] = 1/(4t_2), \tag{2.45}$$

and

$$\alpha_2[1 + \gamma z] + \beta_2[1 + \gamma/z] = 0. \tag{2.46}$$

62

It then follows from the above two equations that

$$\alpha_2 = \frac{z + \gamma}{4t_2(z^2 + \gamma^2 - 1 - \gamma^2 z^2)}, \tag{2.47}$$

which diverges when $\gamma = \pm 1$. We get $\gamma = 1$ for repulsive V. Furthermore,

$$\beta_2 = -\alpha_2 \frac{1 + \gamma z}{1 + \gamma/z}, \tag{2.48}$$

which for $\gamma = 1$ yields $\beta_2 = -\alpha_2 z$. Thus we see that $g_0 = -(\alpha_2 + \beta_2) = -\alpha_2(1 - z)$ diverges for $\gamma = 1$ or $V_c = 4t_2$. We also find that for $0 \neq n \leq N$

$$g_n = \alpha_2 z^n + \beta_2/z^n = \alpha_2 \left(e^{i\pi n/N} - e^{-i\pi(n-1)/N} \right), \tag{2.49}$$

also diverges since $2n - 1 \neq 2N$. *The instability condition $V_c = 4t_2$ is independent of N and hence is valid for large N as well!* Another interesting observation based on $\beta_2 = -\alpha_2 z$ is that

$$g_{-k} = g_{N-k} = -\alpha_2/z^k - \beta_2 z^k = \beta_2/z^{k+1} + \alpha_2 z^{k+1} = g_{k+1}. \tag{2.50}$$

2.5 Numerical study of the $t_2 - V$ model for o-rings

We calculate the structure factor at large repulsion so that the CDW would be better defined (with larger values for the structure factor) even for finite number of sites. Since the allowed momenta for HCBs in o-rings (with $2N+1$ sites) are $k = \frac{2n\pi}{2N+1}$ with $n = 1, 2, \ldots, 2N+1$;

63

N_p/N_s	Analytical value of $[S(Q)]_{\mathrm{max}}$	Numerical value of $[S(Q)]_{\mathrm{max}}$		
		$V = 50$	$V = 100$	$V = 500$
$\frac{4}{9}$	3.6848	3.6836	3.6845	3.6848
$\frac{6}{13}$	5.2944	5.2935	5.2942	5.2944
$\frac{8}{17}$	6.9095	6.90878	6.9093	6.9095
$\frac{10}{21}$	8.5269	8.5263	8.5267	8.5269

Table 2.1: At filling fraction $\mathrm{f} = \frac{N}{(2N+1)}$, the numerical value of $[S(Q)]_{\mathrm{max}}$ calculated at large V agrees quite well with the analytic value obtained from Eq. (2.54).

the structure factor $S(k)$ will have peaks at $k = Q \equiv \pi \pm \frac{\pi}{2N+1}$; in fact π is not an allowed value for the momentum k!. For $k = Q = \pi + \frac{\pi}{2N+1}$ we have

$$S(Q) = \sum_{l=1}^{2N+1} e^{i\left(\pi + \frac{\pi}{2N+1}\right)l} W(l) = \sum_{l=1}^{2N+1} (-1)^l e^{i\left(\frac{\pi}{2N+1}\right)l} W(l). \qquad (2.51)$$

Substituting the expression for $W(l)$ and ignoring the term $\langle n_j \rangle \langle n_{j+l} \rangle = \langle n_j \rangle^2$ in $W(l)$ $\left(\text{because } \sum_{l=1}^{2N+1} e^{i\left(\pi + \frac{\pi}{2N+1}\right)l} = 0\right)$ we get

$$S(Q) = \frac{4}{2N+1} \sum_{j=1}^{2N+1} \left\langle n_j \sum_{l=1}^{2N+1} n_{j+l} (-1)^l e^{i\left(\frac{\pi}{2N+1}\right)l} \right\rangle. \qquad (2.52)$$

In the above equation, setting $j + l = m$ yields

$$S(Q) = \frac{4}{2N+1} \sum_{j=1}^{2N+1} \left\langle n_j (-1)^j e^{-i\left(\frac{\pi}{2N+1}\right)j} \times \sum_{m=1}^{2N+1} n_m (-1)^m e^{i\left(\frac{\pi}{2N+1}\right)m} \right\rangle. \qquad (2.53)$$

At large repulsion all the particles in o-rings will be confined to N alternate sites similar to the case of e-rings (with $2N$ sites). First, we consider the filling $\mathrm{f} = N/(2N+1)$ (i.e.,

N_p/N_s	Analytical value of $[S(Q)]_{\max}$	Numerical value of $[S(Q)]_{\max}$		
		$V = 50$	$V = 100$	$V = 500$
$\frac{6}{15}$	4.4828	4.4574	4.4618	4.4650
$\frac{6}{17}$	3.8866	3.8634	3.8691	3.8734
$\frac{6}{19}$	3.4302	3.4124	3.4183	3.4228
$\frac{6}{21}$	3.0697	3.0566	3.0623	3.0668
$\frac{8}{19}$	6.0982	6.0702	6.0740	6.0766
$\frac{8}{21}$	5.4572	5.4264	5.4316	5.4355

Table 2.2: At filling fraction $f = \frac{N_p}{(2N+1)}$ with $N_p < N$, the analytical value of $[S(Q)]_{\max}$ [obtained from Eq. (2.54)] approximates reasonably well the numerical value at large V.

$N_p = N$). Consequently, the maximum value of the structure factor is given by

$$
\begin{aligned}
[S(Q)]_{\max} &= \frac{4}{2N+1}\left[\frac{N_p}{N}(-1)e^{-i\frac{\pi}{2N+1}} + \frac{N_p}{N}(-1)^3 e^{-i\frac{3\pi}{2N+1}}\right.\\
&\quad\left. + \cdots + \frac{N_p}{N}(-1)^{2N-1}e^{-i\frac{(2N-1)\pi}{2N+1}}\right]\left[\text{H.c.}\right]\\
&= \frac{2}{2N+1}\left(\frac{N_p}{N}\right)^2\left(\frac{1}{1-\cos\left(\frac{\pi}{2N+1}\right)}\right),
\end{aligned}
\tag{2.54}
$$

with $N_p = N$ for $f = N/(2N+1)$. For the $N_p = N$ case, the above expression for $[S(Q)]_{\max}$ is exact at all values of N (see Table 2.1).

In the thermodynamic limit ($2N + 1 \to \infty$), the above expression for $[S(Q)]_{\max}$ diverges as

$$
[S(Q)]_{\max} = \frac{4}{\pi^2}\left(\frac{4N_p^2}{2N+1}\right) = \frac{4}{\pi^2}\left(\frac{4N_p^2}{N_s}\right).
\tag{2.55}
$$

We rescale $S(Q)$ as

$$
S^*(Q) = \frac{S(Q)}{[S(Q)]_{\max}}.
\tag{2.56}
$$
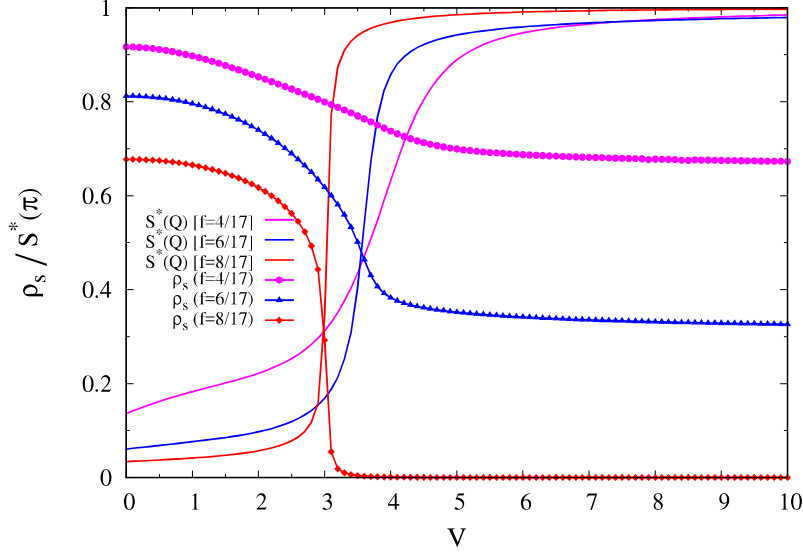
Figure 2.3: Plots of rescaled structure factor $S^*(Q) \equiv S(Q)/[S(Q)]_{\mathrm{max}}$ (with $Q = \pi \pm \frac{\pi}{2N+1}$) and superfluid fraction ρ_s at various fillings f obtained using modified Lanczos method. At a critical repulsion there is a sharp rise in $S^*(Q)$ with a concomitant significant drop in ρ_s.

For $N_p < N$, all the N sites considered for particle occupation would be connected through hopping so that the total energy is minimized, i.e., the potential energy is zero and the kinetic energy is minimized. Next, we assume that the N_p particles are uniformly distributed among these N alternate sites; such an assumption is valid for large values of N as the end effects (i.e., at the boundary of the N alternate sites) is negligible. Then, for $N_p < N$, the expression (2.54) is approximate at finite N (see Table 2.2) and exact for $N \to \infty$. Furthermore, the expression for the peak value of the structure factor for e-rings [given by Eq. (2.7)] differs from that for o-rings [given by Eq. (2.55)] due to the phase factor $e^{-i\left(\frac{\pi}{2N+1}\right)m}$ in Eq. (2.54); interestingly the difference is not negligible in the thermodynamic limit (i.e., $2N + 1 \to \infty$).

Next, we will outline our procedure for calculating the superfluid density for o-rings at $V = 0$. From the definition of superfluid density ρ_s it is obvious that, to calculate ρ_s, all

66

we need is to calculate the total energy $E(\theta)$ which is independent of whether the particles are fermions or hard-core-bosons. So, if we recast our system in terms of fermions, the boundary condition turns out to be

$$e^{ik(2N+1)2} = -1 = e^{i(2m+1)\pi}, \tag{2.57}$$

where m is an integer. The above equation implies that

$$k = \frac{(2m+1)\pi}{2(2N+1)} \quad \text{with} \quad -\frac{N_p}{2} \leq m \leq \frac{N_p}{2} - 1.$$

So, for $V = 0$, we obtain the superfluid density for o-rings

$$\rho_s = \frac{1}{N_p} \sum_{k=-\frac{\pi(N_p-1)}{2(2N+1)}}^{\frac{\pi(N_p-1)}{2(2N+1)}} \frac{(e^{2ik} + e^{-2ik})}{2} = \frac{1}{N_p} \frac{\sin\left(\frac{\pi N_p}{2N+1}\right)}{\sin\left(\frac{\pi}{2N+1}\right)}. \tag{2.58}$$

When o-rings are considered, we find that at all fillings f the structure factor $S^*(Q)$ shows a sharp increase at a critical value of repulsion V_c; concomitantly, there is a sharp drop in the superfluid fraction ρ_s at the same critical repulsion V_c (see Fig. 2.3). For finite systems, at large V, ρ_s values are the same for e-rings and o-rings at fillings f $= N_p/(2N)$ and f $= N_p/(2N+1)$, respectively. In the thermodynamic limit, we expect a first order CDW transition, with the structure factor jumping at a critical V similar to the case in Fig. 2.1 for e-rings (although, magnitude-wise, $[S(Q)]_{\max}$ for o-rings is $\frac{4}{\pi^2}$ of the structure factor $[S(\pi)]_{\max}$ for e-rings); simultaneously, at the same critical V we expect a sudden drop in ρ_s similar to Fig. 2.1. At filling $N/(2N+1)$ the superfluid fraction decreases to zero, whereas at all lower fillings [i.e., $N_p/(2N+1)$ with $N_p < N$] it transits to a nonzero value. Thus, at filling $N/(2N+1)$, superfluidity and CDW state are mutually exclusive; whereas, at all
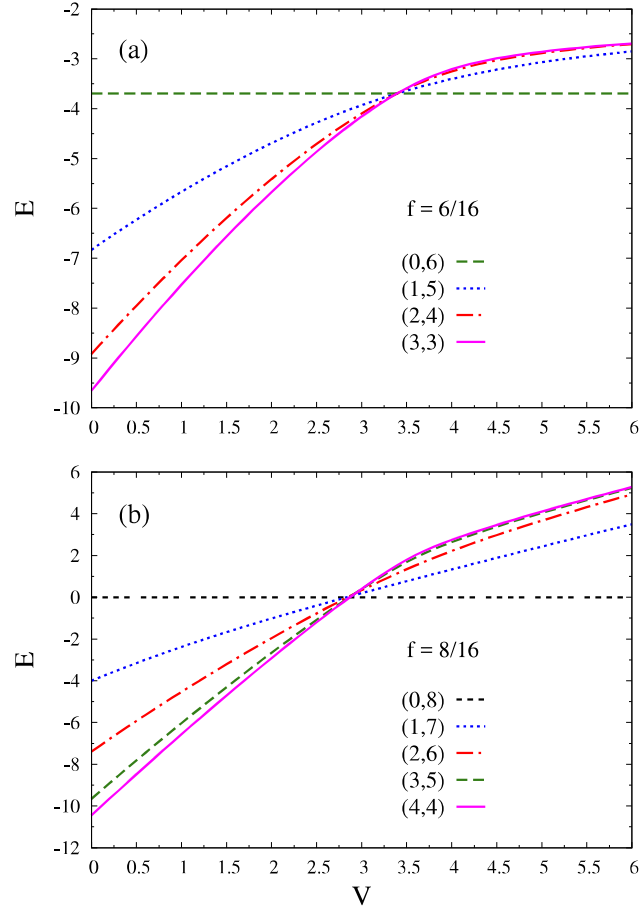
Figure 2.4: Plots of energy E versus repulsion V for (a) the lowest energy states with (m,6-m) particles in e-ring with $N_s = 16$ and $N_p = 6$ (non-half filled case); and (b) the lowest energy states with (m,8-m) particles in e-ring with $N_s = 16$ and $N_p = 8$ (half-filled case).

fillings $N_p/(2N + 1)$ with $N_p < N$ the system undergoes a transition from a superfluid to a supersolid.

2.6   Comparison between e-rings and o-rings

In our $t_2 - V$ model, e-rings have two similar homogeneous Fermi seas whose occupational symmetry is broken at a critical repulsion to populate only one non-interacting Fermi sea
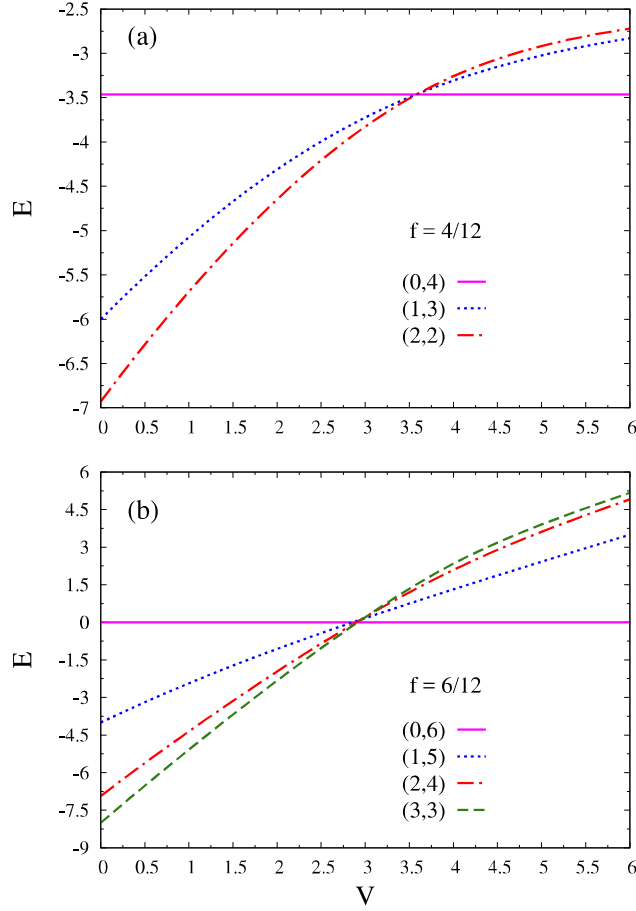
Figure 2.5: Plots of energy E versus repulsion V for (a) the lowest energy states with $(m, 4 - m)$ particles in e-ring with $N_s = 12$ and $N_p = 4$ (non-half filled case); and (b) the lowest energy states with $(m, 6 - m)$ particles in e-ring with $N_s = 12$ and $N_p = 6$ (half-filled case)

thereby producing a supersolid (CDW) at non-half (half) filling. The situation for o-rings, corresponds to a single band breaking up into two bands with a midgap state. From the energy versus V plots for e-rings (in Figs. 2.4 and 2.5), we note that for different finite systems with even number of sites (both for half and non-half fillings) the various lowest energy levels [with particle distribution $(m, N_p - m)$] cross at a critical V; from this and our Green's function analysis above, we conclude that in the thermodynamic limit the system will undergo a first order phase transition at all fillings. On the other hand, for o-rings, since
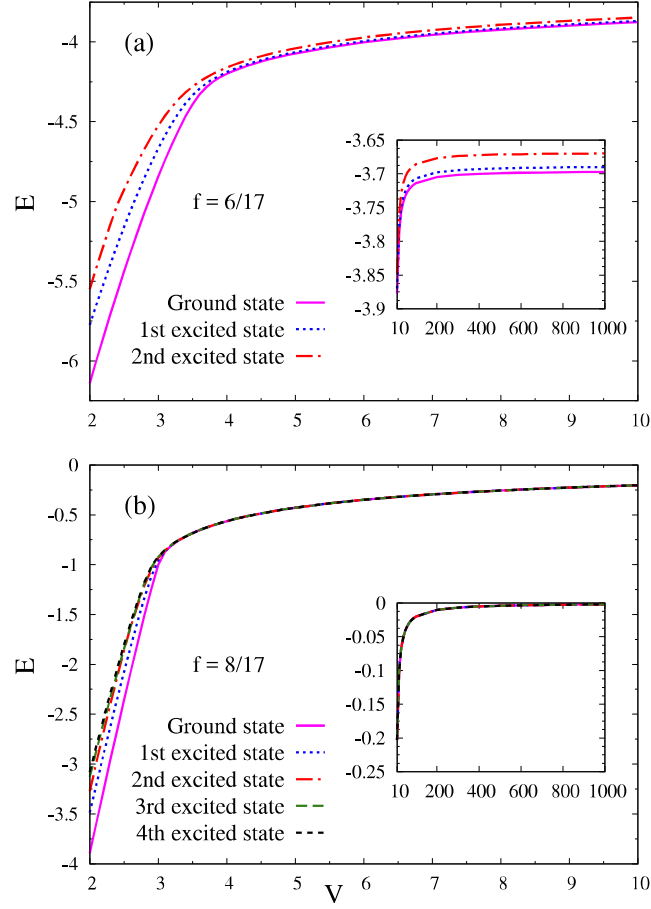
Figure 2.6: Plots of energy E versus repulsion V for (a) the three lowest energy states in o-ring with $N_s = 17$ and $N_p = 6$; and (b) the five lowest energy states in o-ring with $N_s = 17$ and $N_p = 8$.

the system has all sites connected through NNN hopping (much like a Moebius strip), there do not exist two sublattices. Consequently, when we plotted the lowest few energy states for a finite odd number of sites, there is no energy level crossing at any repulsion V for various fillings considered; the curves monotonically increase with repulsion [see Fig. 2.6 and 2.7]. For fillings f $= N/(2N + 1)$, we observe that beyond some critical repulsion (close to the value where levels cross in half-filled e-ring with $N_s = 2N$) all the energy levels merge and become degenerate. For filling fractions f $= N_p/(2N+1)$ (with $N_p < N$),

70
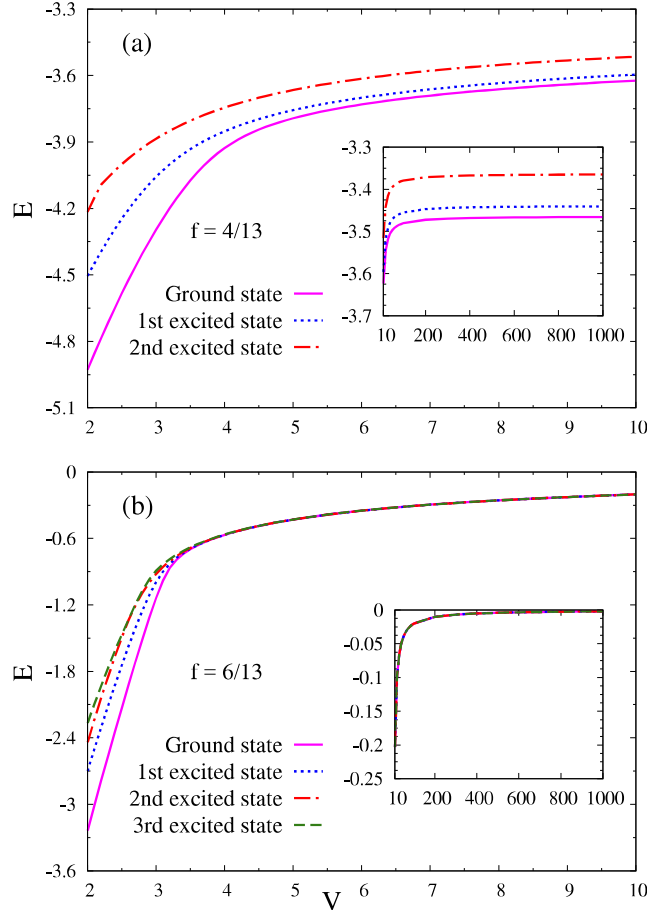
Figure 2.7: Plots of energy E versus repulsion V for (a) the three lowest energy states in o-ring with $N_s = 13$ and $N_p = 4$; and (b) the four lowest energy states in o-ring with $N_s = 13$ and $N_p = 6$.

the energy levels come close to each other at a critical V that is close to the point where levels cross for e-rings with $f = N_p/(2N)$; a little beyond this critical V, the gap between any two energy levels becomes constant and remains the same even at large V. The insets in Figs. 2.6(a), 2.6(b), 2.7(a), and 2.7(b), show that at large V the graphs remain more or less unchanged. Thus, for finite systems with odd number of sites, the energy levels never cross each other. Still, we expect that in the thermodynamic limit the ground state of an o-ring will be similar to that of an e-ring and thus will have a kink at the same critical

71
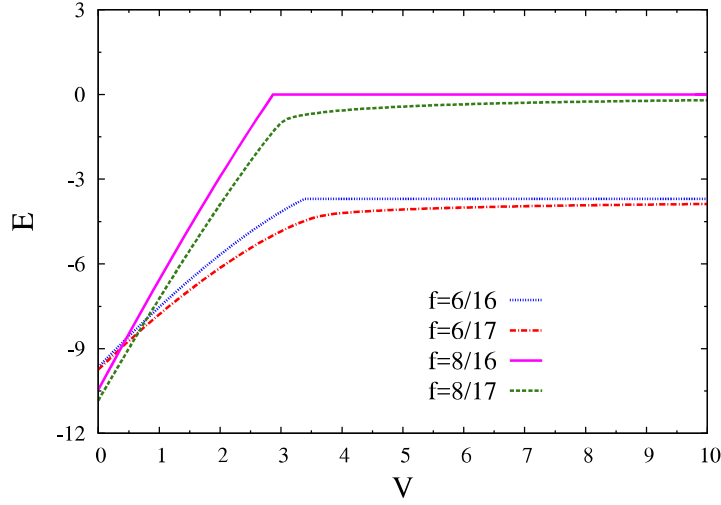
Figure 2.8: Plots of energy E versus repulsion V for ground state at various fillings f $= N_p/N_s$.

repulsion V_c. As a result, in the thermodynamic limit, we expect both the systems to have a similar kind of phase transition. Another important point to note, as $V \to \infty$, is that the ground-state energy of o-rings at f $= N_p/(2N + 1)$ approaches (from below) the ground-state energy of e-rings at f $= N_p/(2N)$ [see Fig. 2.8]. Consequently, the superfluid fraction takes the same value for both the cases in the limit of large V (see Table 2.3).

However, in the macroscopic limit, the energy spectrum is not expected to be the same for the two cases; for instance, there is a mid-gap state for the odd case which is not there for the even case . The key difference between the rings with even and odd number of sites seems to be the difference in the peak value of the structure factor at large V (above critical V) for finite (infinite) systems. In the thermodynamic limit we expect the structure factors for both o-rings and e-rings to diverge, but their ratio will still be $\frac{4}{\pi^2}$. For finite e-rings, it is also important to point out our finding that the energy levels cross each other at approximately the same critical repulsion. From the plots of E versus V at a fixed filling fraction f and different system sizes N_s [such as in Figs. 2.4(b) and 2.5(b)], we observe that

N_p/N_s	Superfluid fraction ρ_s		
	$V = 50$	$V = 100$	$V = 500$
$\frac{6}{16}$	0.3080	0.3080	0.3080
$\frac{6}{17}$	0.3114	0.3096	0.3080
$\frac{6}{18}$	0.4220	0.4220	0.4220
$\frac{6}{19}$	0.4257	0.4240	0.4226
$\frac{4}{16}$	0.6533	0.6533	0.6533
$\frac{4}{17}$	0.6574	0.6554	0.6537
$\frac{4}{20}$	0.7694	0.7694	0.7694
$\frac{4}{21}$	0.7721	0.7708	0.7698

Table 2.3: The superfluid fraction ρ_s for o-ring at filling f $= N_p/(2N + 1)$ approaches the value of the superfluid fraction for e-ring with f $= N_p/(2N)$ in the large-V limit.

the crossing points get closer as the system size increases. From this we can expect that, in the thermodynamic limit, all the energy levels will cross at the same transition point.

2.7 Bose-Einstein condensation

Here, we do not calculate the Bose-Einstein condensate occupation number n_0 because, for a system of HCBs in a one-dimensional tight-binding lattice, it varies as $C(\text{f})\sqrt{N}$ in the thermodynamic limit with the coefficient $C(\text{f})$ depending on filling f [91,92]; consequently, the condensate fraction $n_0/N_p \propto 1/\sqrt{N} \to 0$. Next, in the presence of repulsion (as argued in Ref. [54]), we expect the BEC occupation number n_0 to again scale as $\sqrt{N}$; however, the coefficient of $\sqrt{N}$ will be smaller due to the restriction on hopping imposed by repulsion.

2.8 Connection to other models

Our $t_2 - V$ model can be mapped onto an extremely anisotropic Heisenberg model (with next-nearest-neighbor XY interaction and nearest-neighbor Ising interaction) by identify-
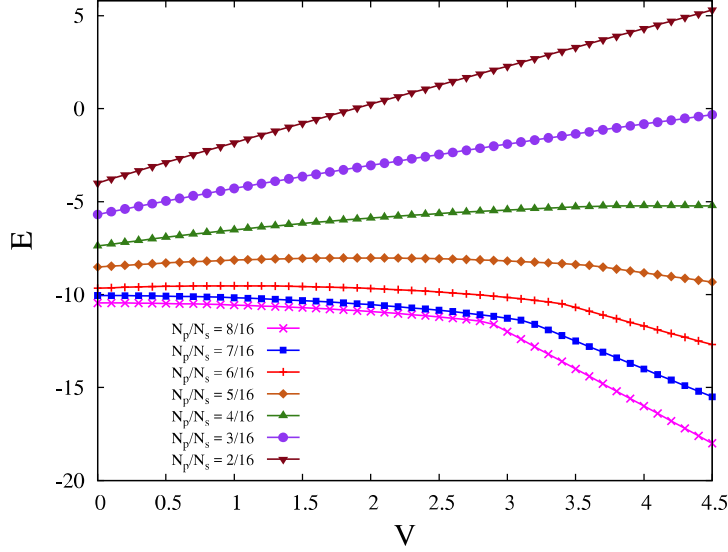
Figure 2.9: Plots of the lowest energy E (obtained using modified Lanczos in a system with $N_s = 16$ sites) for the extremely anisotropic NNN Heisenberg model at various normalized magnetizations $(N_s - 2N_p)/N_s$ corresponding to fillings f $= N_p/N_s$ for the $t_2 - V$ model.

ing $S^+ = b^\dagger$, $S^- = b$, and $S^z = n - \frac{1}{2}$. The resulting spin Hamiltonian is of the form

$$-t_2 \sum_{i=1}^{N_s} (S_{i-1}^+ S_{i+1}^- + \text{H.c.}) + V \sum_{i=1}^{N_s} S_i^z S_{i+1}^z. \tag{2.59}$$

While Heisenberg model was amenable to solution through the Bethe ansatz, the addition of next-nearest-neighbor interaction (similar to the case of Majumdar-Ghosh model [93, 94]) requires an alternate route for its solution. Our spin model lends itself to exact instability solutions (by the Green's function method) in the two limiting cases of two-magnons and antiferromagnetic ground state. The energies at various fillings N_p/N_s for the $t_2 - V$ model correspond to various normalized magnetizations $(N_s - 2N_p)/N_s$ for the spin model. From a plot of the lowest energies at various magnetizations of the spin model, as depicted in Fig. 2.9, we see that the energy increases as the normalized magnetization increases with the ground state corresponding to zero magnetization. From the fact that

74

the critical repulsion is always $V_c \leq 4$, it should be clear that the energy at all fillings and system sizes for $V_c > 4$ is obtained from a tight-binding model with N_p particles in one sublattice only. Thus at $V_c > 4$, the energy will certainly increase with the normalized magnetization.

Next, in spite of the fact that the hopping terms are different, we note the semblance between our $t_2 - V$ model and the well-known Su-Schrieffer-Heeger (SSH) model [95,96]. We make the connection that a singlet (formed by two spins on adjacent sites) can be regarded as a HCB located at the center of the singlet [54]. Thus a system of HCBs in one sublattice is transformed to a system of singlets with centers located in one sublattice only. At half-filling, for even number of sites, the ground state of the $t_2 - V$ model at V larger than the critical repulsion can be mapped onto a valence-bond ground state of the Su-Schrieffer-Heeger (SSH) model [95,96]. For an odd number of sites, at filling $N/(2N+1)$, we can map the ground state at large V with two holes on adjacent sites (i.e., a kink) in the $t_2 - V$ model on to the ground state, with a kink or topological defect (with two single bonds on adjacent sites), in the SSH model. For even number of sites as well, the kinks obtained by doping the valence bond state in the SSH model have a counterpart in our $t_2 - V$ model.

2.9 Discussion

Our $t_2 - V$ model is the limiting case of the one-dimensional CBM (cooperative breathing mode) model (i.e., $t_1 - t_2 - V$ model), which depicts a simpler one-band case that is expected to be useful in understanding the CBM physics in real systems such as the bismuthates, the cuprates, and the manganites [39]. An important purpose of studying the $t_2 - V$ model is the fact that exact solutions can be obtained analytically for two limiting

cases of this model. Till now we do not know how to solve the more complex $t_1 - t_2 - V$ model analytically. We hope that in future our way of solving the two limiting cases of the $t_2 - V$ model analytically (using Green's function technique) will lead to useful approaches to handle more complex problems such as the $t_1 - t_2 - V$ model.

In Ref. [39], $t_2 - V$ model was studied for spinless fermions in e-rings; structure factor $S(\pi)$ and ground-state energy were obtained for some filling fractions to show that the system undergoes a discontinuous transition from a Luttinger liquid to a conducting commensurate CDW state away from half filling while at half filling one obtains a Mott insulator. In the present chapter, we recast the $t_2 - V$ model in terms of HCBs. Here, along with the structure factor and the ground-state energy, we additionally calculate the superfluid fraction. In e-rings, we show that the system undergoes a striking discontinuous transition from a superfluid to either a CDW insulator (at half filling) or a supersolid (at non-half fillings).

In Ref. [39], only systems with even number of sites was considered, whereas here we also study systems with odd number of sites; we show that supersolidity is realized in o-rings at large repulsion and fillings $N_p/(2N + 1)$ with $N_p < N$. When o-rings are considered, at all fillings $N_p/(2N + 1)$ with $N_p < N$, the structure factor shows a sharp increase at a critical value of repulsion; simultaneously, there is a sharp drop (to a non-zero value) in the superfluid fraction at the same critical repulsion (see Fig. 2.3). At $V = 0$, we derived an expression for the superfluid fraction [see Eq. (2.58)] which matches with the numerical result in Fig. 2.3. The superfluid fraction, in the limit $V \to \infty$, for o-rings [at fillings $N_p/(2N + 1)$] approaches the value of the superfluid fraction, when $V > V_c$, for e-rings [at fillings $N_p/2N$] — a fact supported by numerical results (see Table 2.3). From the expression for the superfluid fraction in e-rings when $V > V_c$ [see Eq. (2.11)], it is clear that, for all fillings $N_p/(2N + 1)$ with $N_p < N$, we will have non-zero superfluid

76

fraction in o-rings even in the thermodynamic limit. On the other hand, we have also shown that the structure factor $[S(Q)]_{\max}$ calculated analytically for large V agrees quite well with that calculated numerically for sufficiently large systems (see Table 2.2). It is also shown that in the thermodynamic limit, at large V, the structure factor for o-rings appears to be $4/\pi^2$ times the structure factor for e-rings [see Eq. (2.55)]; as a result we expect the structure factor for o-rings to diverge as $N \to \infty$. Hence, we can conclude that in the thermodynamic limit, at all all fillings $N_p/(2N+1)$ with $N_p < N$, the system for o-rings exhibits supersolidity (at large V).

As regards relevant work, in Ref. [97] the authors consider nearest-neighbor hopping (and repulsion) and unfrustrated next-nearest-neighbor hopping (and repulsion) that can be realized in a zigzag ladder with two legs. As pointed out in this chapter, nearest-neighbor hopping and next-nearest-neighbor hopping can be tuned independently. Thus this work also shows that our $t_2 - V$ model is physically realizable.

Also of relevance is the work by Struck et al. [98] where various values (including sign change) of nearest-neighbor coupling J and next-nearest-neighbor coupling J' can be achieved for hard-core-boson systems. Thus, we feel that our $t_2 - V$ model can be simulated experimentally by introducing repulsions and next-nearest-neighbor coupling J'.

Recently, Mishra et al. [32,99] studied a one-dimensional system of HCBs, with nearest-neighbor hopping and interaction and next-nearest-neighbor hopping, described by the Hamiltonian

$$
H = -t_1 \sum_i (b_i^\dagger b_{i+1} + \text{H.c.}) - t_2 \sum_i (b_i^\dagger b_{i+2} + \text{H.c.}) + \sum_i V \left(n_i - \frac{1}{2} \right) \left(n_{i+1} - \frac{1}{2} \right).
$$

$$(2.60)$$

While Pankaj and Yarlagadda [39] considered unfrustrated next-nearest-neighbor hopping,

Misra et al. [32, 99] focussed on frustrated hopping. In Ref. [99], at half filling the authors set $t_1 = 1$ and varied t_2 from 0 to $-t_1$ to obtain the total phase diagram containing superfluid, CDW, and bond-ordered phases. At incommensurate densities (non-half fillings) and with $t_2 = -t_1$, the authors of Ref. [32] found a supersolid phase. In Refs. [32, 99], the competition between two different hopping processes (i.e., hoppings from one site to nearest-neighbor site and to next-nearest-neighbor site with different signs of the hopping terms) gives rise to kinetic frustration in the system. On the other hand, our $t_2 - V$ model depicts the strong EPI limit; as a result there is only one kind of hopping process. Consequently, there is no frustration in our $t_2 - V$ system.

2.10   Conclusions

We investigated a model which captures the essential dominant-transport feature of cooperative strong EPI in all dimensions (and in even non-cubic geometries). Our study shows that, compared to the non-cooperative situation, cooperative EPI produces strikingly different physics such as a dramatic superfluid to a supersolid transition with the order parameter jumping to its maximum value. Understanding one-dimensional strong EPI systems, besides being helpful in designing oxide rings, will be of relevance to predicting and controlling the variation of system properties in the direction normal to the interface in oxide heterostructures; needless to say, oxide rings and oxide heterostructures offer extraordinary scientific and technological opportunities [100].

STUDY OF LONG-RANGE ORDERS OF HARD-CORE BOSONS COUPLED TO COOPERATIVE NORMAL MODES IN TWO-DIMENSIONAL LATTICES

3.1 Introduction

Supersolidity is observed in a variety of lattice systems such as the three-dimensional doped $BaBiO_3$ [4, 5]; the layered dichalcogenides [6] and molecular crystals [7]; and the quasi-one-dimensional doped trichalcogenide $NbSe_3$ [8] and doped spin ladder $Sr_{14}Cu_{24}O_{41}$ [9, 10]. Of importance are the class of materials that display superconductivity and diagonal long-range order due to strong e-ph interaction such as K or Pb doped $BaBiO_3$ (where a 10% change in the $Bi - O$ bond length [34] has been observed) and the alkali

metal fullerides [101–103]. Interestingly, $BaBiO_3$ assumes perovskite structure with two adjacent oxygen octahedra sharing an oxygen leading to a cooperative breathing mode (CBM). Furthermore, $BaBiO_3$ displays valence disproportionation with local cooper pairs [i.e., HCBs] being formed and these HCBs couple to the CBM [42].

As mentioned earlier in Sec. 1.4, a variety of lattice models manifest the existence of supersolid ground state. However, by using extended boson Hubbard models involving HCBs, commensurate supersolid has been unobtainable in unfrustrated systems such as square lattices. On the other hand, supersolids can be realized in square lattices at incommensurate fillings by a mechanism where particles (i.e., interstitials) or holes (i.e., vacancies) doped into a perfect crystal form a condensate by delocalizing in the crystalline order. Furthermore, although striped supersolidity has been achieved in Refs. [15, 17] on square lattices, it is nondiagonal and characterized by density ordering wavevector $(\pi, 0)$ or $(0, \pi)$. Even though diagonal stripes [characterized by crystalline ordering wavevector $(2\pi/3, 2\pi/3)$ or $(2\pi/3, 4\pi/3)$] have been observed in systems such as $La_{2-x}Sr_xNiO_4$ (LSNO) at $x = 1/3$ hole doping [45–51] and predicted theoretically for long-range interactions in a lattice gas model at one-third filling [52], so far the corresponding diagonal striped supersolid (dsSS) has been elusive on a square lattice (that is not subject to an external potential). Additionally, whether a cooperative e-ph interaction (that involves cooperative Jahn-Teller distortions) can explain the observed stripe charge order in LSNO is a controversial issue [104–106].

In the class of extended boson Hubbard models of the type $t_1 - t_2 - ... - t_m - V_1 - V_2 - ... - V_n$ [involving hoppings t_1, t_2, t_3, etc. and interactions V_1, V_2, V_3, etc. of ranges nearest neighbor (NN), next-nearest neighbor (NNN), next-to-next-nearest neighbor (NNNN), etc.] on a square lattice, the minimum model for realizing a checkerboard supersolid (cSS) is the $t_2 - V_1$ model [107, 108]. It has also been shown that star/stripe supersolid [corresponding

to crystalline ordering wavevector $(\pi, 0)$ or $(0, \pi)$] can be realized in a $t_1 - V_1 - V_2$ model; at one-fourth filling, a star solid results which is asymmetric with respect to doping with interstitials and vacancies [15]. Identifying the relevant extended boson Hubbard model for obtaining the dsSS around one-third filling and characterizing the state are still open problems.

In this chapter, inspired by the doped bismuthate systems, we develop a microscopic theory of HCBs strongly coupled to the cooperative breathing mode in a 2D perovskite lattice. The effective Hamiltonian for the HCBs is shown to be an extended boson Hubbard model of the form $t_1 - t_2 - t_3 - V_1 - V_2 - V_3$. The V_1, V_2, and V_3 repulsive interactions correspond to the minimum interactions needed to realize the diagonal striped-order at one-third filling. Unlike many lattice models of the extended boson Hubbard type, the parameters (i.e., hopping term, strength of HCB-ph coupling, and phonon frequency) in our $t_1 - t_2 - t_3 - V_1 - V_2 - V_3$ model either can be determined from band-structure calculations or can be obtained from experiments. Supersolidity in our model results only away from one-third filling and is shown to be asymmetric with respect to doping the commensurate diagonal-striped solid (dsS) with vacancies and interstitials. Although checkerboard supersolidity (away from half-filling) and diagonal striped supersolidity (away from one-third filling) are realized, there is no direct supersolid-supersolid phase transition between the two phases. We also show that our cooperative HCB-ph framework can be extended to study charge order in LSNO; we demonstrate that the observed diagonal-stripe order at one-third filling and the checkerboard order at half filling in LSNO can be explained by invoking cooperative Jahn-Teller effect.

The chapter is organized as follows. In Sec. 3.2, we derive an effective Hamiltonian of the system using a non-perturbative treatment. Next, in Sec. 3.3 we briefly describe the numerical procedure, as well as the quantities/parameters used in our study. Then, we
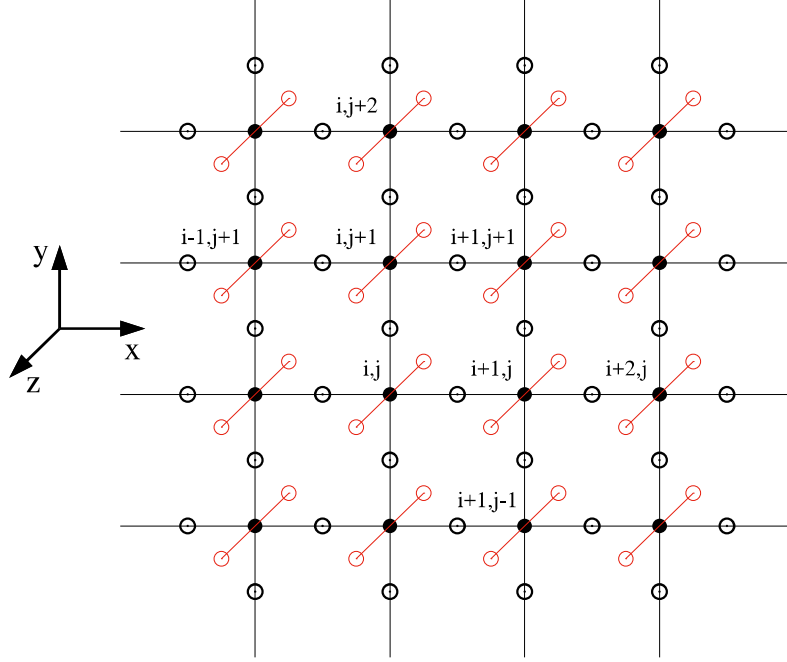
Figure 3.1: Two-dimensional cooperative breathing mode (CBM) system with hopping sites of hard-core-bosons (filled circles), in-plane oxygen atoms (black empty circles) and out-of-plane oxygen atoms (red empty circle). Only the in-plane oxygens are involved in cooperative distortions.

discuss the results in Sec. 3.4, followed by a comparison with experimental observations in Sec. 3.5. Finally, in Sec. 3.6, we conclude.

3.2   Effective Hamiltonian

We start with a 2D model of HCBs depicted in Fig. 3.1. The HCBs interact with the in-plane (xy) oxygen atoms via CBM, whereas the nature of the interaction is noncooperative in the case of the out-of-plane oxygen atoms in the z direction. The Hamiltonian of such a

system can be written as $H = H_t + H_I + H_l$, where the hopping term H_t is given by

$$H_t = -t \sum_{i,j} \left(d_{i+1,j}^\dagger d_{i,j} + d_{i,j+1}^\dagger d_{i,j} + \text{H.c.} \right), \quad (3.1)$$

with $d_{i,j}(d_{i,j}^\dagger)$ being the destruction (creation) operator of a HCB at the hopping site (i,j) and t being the hopping integral. The second term H_I in the Hamiltonian, which represents the HCB-ph interaction, has the form

$$H_I = -g\omega_0 \sum_{i,j} \left[(a_{x;i,j}^\dagger + a_{x;i,j})(n_{i,j} - n_{i+1,j}) + (b_{y;i,j}^\dagger + b_{y;i,j})(n_{i,j} - n_{i,j+1}) \right.$$
$$\left. + \gamma(c_{z;i,j}^\dagger + c_{z;i,j})n_{i,j} \right], \quad (3.2)$$

where $\gamma = \sqrt{2}$, g is the HCB-ph coupling constant, and ω_0 is the optical-phonon frequency. The terms $(a_{x;i,j}^\dagger + a_{x;i,j})/\sqrt{2M\omega_0}$ and $(b_{y;i,j}^\dagger + b_{y;i,j})/\sqrt{2M\omega_0}$ denote the displacement of the oxygen atom that is next to the (i,j)th hopping site and in the positive x and y directions, respectively; here, M is the mass of oxygen atom. The relative displacement of the two out-of-plane oxygens next to the (i,j)th site couples to the HCB at (i,j)th site and is denoted by $(c_{z;i,j}^\dagger + c_{z;i,j})/\sqrt{2\frac{M}{2}\omega_0}$ with $M/2$ being the reduced mass of the oxygen pairs. The expressions $(n_{i,j} - n_{i+1,j})$ and $(n_{i,j} - n_{i,j+1})$ in the first and second terms of Eq. (3.2) take care of the cooperative HCB-ph interaction along the x and y directions, respectively. In the third term, note that we have only $n_{i,j}$ because of the noncooperative nature of the HCB-ph interaction along the z direction. Furthermore, the last term in the Hamiltonian (i.e., the lattice term H_l), representing simple harmonic oscillators, is of the

form

$$H_l = \omega_0 \sum_{i,j} \left(a^\dagger_{x;i,j} a_{x;i,j} + b^\dagger_{y;i,j} b_{y;i,j} + \eta c^\dagger_{z;i,j} c_{z;i,j} \right), \qquad (3.3)$$

with $\eta = 1$. It is important to note that, the above equation for the lattice term H_l treats the displacements $(a^\dagger_{x;i,j} + a_{x;i,j})/\sqrt{2M\omega_0}$ and $(b^\dagger_{y;i,j} + b_{y;i,j})/\sqrt{2M\omega_0}$ as independent variables; this is justified because these displacements depend on the site-occupancy differences $(n_{i,j} - n_{i+1,j})$ and $(n_{i,j} - n_{i,j+1})$ which are independent of each other. A similar consideration lead to a similar lattice term [given by Eq. (4)] in the treatment of cooperative Jahn-Teller distortions in Ref. [109].

We consider systems in the non-adiabatic regime ($t/\omega_0 \leqslant 1$) and strong-coupling region (large g^2). To produce an effective polaronic Hamiltonian, we employ a duality transformation where the strong-coupling problem in the original frame of reference [with small parameter $\propto (g\omega_0)/t$] is transformed into a weak-coupling problem in a dual frame of reference [with small parameter $\propto t/(g\omega_0)$, i.e., inverse of the small parameter in the original frame of reference]. To achieve the above end, we need to modify the Lang-Firsov transformation [110] so as to take into account the cooperative nature of the distortions along the x and y directions and noncooperative nature in the z direction. This involves the following canonical transformation $\tilde{H} = \exp(S)H\exp(-S)$ where S is given by

$$S = -g \sum_{i,j} \left[(a^\dagger_{x;i,j} - a_{x;i,j})(n_{i,j} - n_{i+1,j}) + (b^\dagger_{y;i,j} - b_{y;i,j})(n_{i,j} - n_{i,j+1}) \right.$$
$$\left. + \gamma(c^\dagger_{z;i,j} - c_{z;i,j})n_{i,j} \right]. \qquad (3.4)$$

The transformed Hamiltonian can be written as $\tilde{H} = H_0 + H_1$, where the unperturbed

Hamiltonian is given by

$$H_0 = \omega_0 \sum_{i,j} \left(a^\dagger_{x;i,j} a_{x;i,j} + b^\dagger_{y;i,j} b_{y;i,j} + \eta c^\dagger_{z;i,j} c_{z;i,j} \right) - E_p \sum_{i,j} n_{i,j}$$
$$+ 2V_p \sum_{i,j} \left(n_{i,j} n_{i+1,j} + n_{i,j} n_{i,j+1} \right) - te^{-(E_p+V_p)/\omega_0} \sum_{i,j} \left(d^\dagger_{i+1,j} d_{i,j} + d^\dagger_{i,j+1} d_{i,j} + \text{H.c.} \right),$$

(3.5)

and the perturbation by

$$H_1 = \sum_{i,j} H_{1i,j}$$
$$= -te^{-(E_p+V_p)/\omega_0} \sum_{i,j} \left[d^\dagger_{i+1,j} d_{i,j} \left(\tau^{ij}_{+x}{}^\dagger \tau^{ij}_{-x} - 1 \right) + d^\dagger_{i,j+1} d_{i,j} \left(\tau^{ij}_{+y}{}^\dagger \tau^{ij}_{-y} - 1 \right) + \text{H.c.} \right],$$

(3.6)

where

$$\tau^{ij}_{\pm x} = \exp \left[\pm g(2a_{i,j} - a_{i-1,j} - a_{i+1,j}) \pm g(b_{i+1,j-1} + b_{i,j} - b_{i,j-1} - b_{i+1,j}) \right.$$
$$\left. \pm \gamma g(c_{i,j} - c_{i+1,j}) \right],$$

and

$$\tau^{ij}_{\pm y} = \exp \left[\pm g(2b_{i,j} - b_{i,j-1} - b_{i,j+1}) \pm g(a_{i-1,j+1} + a_{i,j} - a_{i-1,j} - a_{i,j+1}) \right.$$
$$\left. \pm \gamma g(c_{i,j} - c_{i,j+1}) \right].$$

Here $E_p = (4 + \gamma^2)g^2\omega_0$ is the polaronic energy and $2V_p = 2g^2\omega_0$ represents the nearest-neighbor repulsion for the HCBs.

The eigenstates of the unperturbed Hamiltonian H_0, relevant for perturbation theory are $|n, m\rangle = |n\rangle_{hcb} \otimes |m\rangle_{ph}$, with $|0, 0\rangle$ being the ground state with no phonons. The corresponding eigenenergies of such states are given by $E_{n,m} = E_n^{hcb} + E_m^{ph}$. Similar to the case of one-dimensional CBM model [39], we also have $\langle n, 0|H_1|n, 0\rangle = 0$, which yields the first-order perturbation term $\langle 0, 0|H_1|0, 0\rangle = 0$. In the region of interest in the parameter space, we note that $te^{-(E_p+V_p)/\omega_0} << \omega_0$; we perform second order perturbation theory, as discussed in Sec. 1.6, similar to that in the 1D CBM model [39] and obtain the effective Hamiltonian to be

$$H_{\text{eff}} = \langle 0|_{ph} H_0 |0\rangle_{ph} + H^{(2)}, \tag{3.7}$$

where

$$H^{(2)} = \sum_{i,j,k,l} \sum_m \frac{\langle 0|_{ph} H_{1i,j} |m\rangle_{ph} \langle m|_{ph} H_{1k,l} |0\rangle_{ph}}{E_0^{ph} - E_m^{ph}}. \tag{3.8}$$

One can easily see that the first term in H_{eff} is

$$
\begin{aligned}
\langle 0|_{ph} H_0 |0\rangle_{ph} = & - E_p \sum_{i,j} n_{i,j} + 2V_p \sum_{i,j} (n_{i,j} n_{i+1,j} + n_{i,j} n_{i,j+1}) \\
& - te^{-(E_p+V_p)/\omega_0} \sum_{i,j} \left(d_{i+1,j}^\dagger d_{i,j} + d_{i,j+1}^\dagger d_{i,j} + \text{H.c.} \right),
\end{aligned}
\tag{3.9}
$$

whereas the simplification of the second term (i.e, $H^{(2)}$) requires quite a bit of algebra. We extend the derivation of the effective Hamiltonian for the 1D CBM case [39] to our 2D case as well. As shown by using Schrieffer-Wolff transformation in Appendix A of Refs. [53, 54] (also discussed in Sec. 1.6), since $te^{-(E_p+V_p)/\omega_0} << \omega_0$, H_{eff} represents the exact Hamiltonian up to second order in perturbation. The small parameter here is given by

$\left[\frac{t^2}{2(E_p+V_p)\omega_0}\right]^{\frac{1}{2}}$ whose derivation is similar to that in Ref. [111]. For the second term $H^{(2)}$ in H_{eff}, we obtain the terms given in the following subsections.

3.2.1 Nearest-neighbor (NN) repulsion

The NN repulsion term comes from a process where a particle jumps to a neighboring site and comes back. In 2D, this term further consists of two parts: $\sum_{i,j}[n_{i,j}(1-n_{i+1,j}) + n_{i+1,j}(1-n_{i,j})]$ and $\sum_{i,j}[n_{i,j}(1-n_{i,j+1}) + n_{i,j+1}(1-n_{i,j})]$. Following a procedure explained in Appendix B, we get the expression for this process to be

$$-V_z\sum_{i,j}[n_{i,j}(1-n_{i+1,j}) + n_{i,j}(1-n_{i,j+1})], \tag{3.10}$$

with $V_z \approx \frac{2t^2}{2E_p+2V_p}$. The denominator $2E_p + 2V_p$ in V_z is the difference of the energy of the intermediate state (i.e., $E_p + 2V_p$ corresponding to the particle in the intermediate site) and the energy of the initial state ($-E_p$). The exact expression for V_z is derived in Appendix B.

3.2.2 Next-nearest-neighbor (NNN) and next-to-next-nearest-neighbor (NNNN) repulsions

We first make an important point while considering a process of a particle hopping to a neighboring site and coming back. In 2D, excluding the originating site, we must take into account the occupancy information about all the three remaining NN sites of the intermediate site of the hopping process. For example, consider a process where a HCB at site (i,j) hops to its neighboring site $(i+1,j)$ and comes back. For this process, we need to keep in mind the occupancy of the sites $(i+2,j)$, $(i+1,j+1)$ and $(i+1,j-1)$, which are the three

relevant neighboring sites of the intermediate site $(i + 1, j)$ (see Fig. 3.1). Depending on whether these sites are occupied or empty, the coefficient of the process will be modified accordingly. Essentially there are four cases: 1) all the three NN sites are empty ; 2) any one of the three neighboring sites is occupied ; 3) any two of the NN sites are occupied; and 4) all the three neighboring sites are occupied. Considering all the cases above, we end up with the following NNN and NNNN repulsion terms in $H^{(2)}$ as detailed in Appendix C.

A. NNN repulsion along diagonals

The first term is the NNN repulsion which acts along the diagonals of the square lattice; it is given by

$$V_2 \sum_{i,j} \left(n_{i,j} n_{i+1,j+1} + n_{i,j} n_{i-1,j+1} \right), \tag{3.11}$$

where

$$
\begin{aligned}
V_2 = 2t^2 \Bigg[&\left(\frac{1}{2} - m \right)^2 \frac{2V_p}{(E_p + V_p)(E_p + 2V_p)} \\
&+ \left(\frac{1}{4} - m^2 \right) \frac{4E_p V_p}{(E_p + V_p)(E_p + 2V_p)(E_p + 3V_p)} \\
&+ \left(\frac{1}{2} + m \right)^2 \frac{2E_p V_p}{(E_p + 2V_p)(E_p + 3V_p)(E_p + 4V_p)} \Bigg],
\end{aligned}
\tag{3.12}
$$

with m being the magnetization of the system.

B. NNNN repulsion along the x and y axes

We find the second term to be the NNNN repulsion which acts along the x and y axes of the square lattice; it is given by

$$V_3 \sum_{i,j} \left(n_{i,j} n_{i+2,j} + n_{i,j} n_{i,j+2} \right), \tag{3.13}$$

with $V_3 = \frac{V_2}{2}$. It is important to note that, in the absence of the NN repulsion $2V_p$, we obtain expressions for V_z, V_2, and V_3 consistent with the noncooperative treatment of the e-ph interaction in Refs. [20, 21].

3.2.3   NNN and NNNN hoppings

The remaining terms in $H^{(2)}$ are the hoppings of the HCBs to the NNN and NNNN sites. Similar to the NNN and NNNN repulsions, the hopping contributions of the HCBs can also be divided into two types: NNN hopping along the diagonals and NNNN hopping along the x and y axes (see Appendix D for details).

A. NNN hopping along diagonals

While calculating the coefficient of the NNN hopping, we have to keep in mind the fact that the HCB passes through an intermediate site while hopping to its NNN site. So the coefficient must depend on the occupancy of the two neighboring sites of the intermediate site. For example, if a HCB at site (i, j) is hopping to its right-upper diagonal site, i.e., $(i+1, j+1)$, it can follow any one of the two possible paths: a) first going along x-axis to the $(i+1, j)$-th site and then along y-axis to the $(i+1, j+1)$-th site; and b) the interchanged process, i.e., hopping along the y-axis first to the $(i, j+1)$-th site followed by a hop along

89

the x-axis to the $(i+1, j+1)$-th site (see Fig. 3.1). For the first path, the coefficient of the hopping depends on whether the two sites $(i+2, j)$ and $(i+1, j-1)$, which are NN of the intermediate site $(i+1, j)$, are occupied or empty. On the other hand, for the second path, the hopping coefficient depends on the occupancy of the two neighboring sites of the intermediate site $(i, j+1)$, i.e., $(i-1, j+1)$ and $(i, j+2)$. To calculate the NNN hopping coefficient, first we forget about the occupancy of the two neighbors of the intermediate site; then, the NNN hopping along the diagonals is obtained to be

$$-\frac{2t^2 e^{-E_p/\omega_0}}{E_p + 2V_p} \sum_{i,j} \left(d^\dagger_{i+1,j+1} d_{i,j} + d^\dagger_{i-1,j+1} d_{i,j} + \text{H.c.} \right), \qquad (3.14)$$

where the coefficient $\frac{2t^2 e^{-E_p/\omega_0}}{E_p + 2V_p}$ is an approximation with the exact expression being given in Appendix D.

Now, taking the two neighbors of the intermediate site into account, the NNN hopping term along the diagonals of the square lattice gets modified to be

$$-t_2 \sum_{i,j} \left(d^\dagger_{i+1,j+1} d_{i,j} + d^\dagger_{i-1,j+1} d_{i,j} + \text{H.c.} \right), \qquad (3.15)$$

where

$$t_2 = \frac{2t^2 e^{-E_p/\omega_0}}{E_p + 2V_p} \left[\left(\frac{1}{2} - m \right)^2 + \left(\frac{1}{4} - m^2 \right) \frac{2E_p + 4V_p}{E_p + 4V_p} + \left(\frac{1}{2} + m \right)^2 \frac{E_p + 2V_p}{E_p + 6V_p} \right]. \qquad (3.16)$$

B. NNNN hopping along the x and y axes

Next, we consider the hopping of the HCBs to the NNNN sites along the x and y axes of the square lattice. Similar to the previous case, the coefficient of the hopping in this case, depends on the occupancy of the two neighboring sites of the intermediate site. For

example, if a HCB is hopping from site (i, j) to its NNNN site $(i + 2, j)$, it has to pass through the intermediate site $(i + 1, j)$ (see Fig. 3.1). So, the coefficient for this process depends on whether the neighboring sites of site $(i + 1, j)$, i.e., $(i + 1, j + 1)$ and $(i + 1, j - 1)$, are occupied or empty. Taking into account all the occupancy possibilities of the neighboring sites of the intermediate site, we get the NNNN hopping term to be

$$-t_3 \sum_{i,j} \left(d^\dagger_{i+2,j} d_{i,j} + d^\dagger_{i,j+2} d_{i,j} + \text{H.c.} \right), \tag{3.17}$$

with $t_3 = \frac{t_2}{2}$.

Again, it should be pointed out that, in the absence of the NN repulsion $2V_p$, the expressions for t_2 and t_3 simplify to be consistent with the results of the noncooperative analysis of the e-ph interaction in Refs. [20, 21].

Finally, taking all the terms present in $H^{(2)}$ into account, H_{eff} in Eq. (3.7) reduces to

$$
\begin{aligned}
H_{\text{eff}} = &- (E_p + 2V_z) \sum_{i,j} n_{i,j} \\
&- t_1 \sum_{i,j} \left(d^\dagger_{i+1,j} d_{i,j} + d^\dagger_{i,j+1} d_{i,j} + \text{H.c.} \right) \\
&+ V_1 \sum_{i,j} \left(n_{i,j} n_{i+1,j} + n_{i,j} n_{i,j+1} \right) \\
&- t_2 \sum_{i,j} \left(d^\dagger_{i+1,j+1} d_{i,j} + d^\dagger_{i-1,j+1} d_{i,j} + \text{H.c.} \right) \\
&+ V_2 \sum_{i,j} \left(n_{i,j} n_{i+1,j+1} + n_{i,j} n_{i-1,j+1} \right) \\
&- t_3 \sum_{i,j} \left(d^\dagger_{i+2,j} d_{i,j} + d^\dagger_{i,j+2} d_{i,j} + \text{H.c.} \right) \\
&+ V_3 \sum_{i,j} \left(n_{i,j} n_{i+2,j} + n_{i,j} n_{i,j+2} \right), \tag{3.18}
\end{aligned}
$$

where $t_1 = te^{-(E_p + V_p)/\omega_0}$, $V_1 = 2V_p + V_z$, and the expressions for all the remaining terms, V_z, t_2, t_3, V_2, and V_3, being the same as defined earlier.

3.3   Numerical Calculations

To study the phase diagram of our effective Hamiltonian of HCBs, we use quantum Monte Carlo (QMC) simulation adopting the stochastic-series-expansion (SSE) technique [44, 112]; furthermore we employ directed loop update [79, 80]. We find it convenient to rewrite the Hamiltonian in terms of spin-1/2 operators. Identifying the relations between the operators for HCBs and those for spin-1/2 particles as $d_{i,j}^\dagger = S_{i,j}^+$, $d_{i,j} = S_{i,j}^-$ and $n_{i,j} = S_{i,j}^z + \frac{1}{2}$, we recast our effective Hamiltonian for HCBs, in units of $2t_1$, as an extended XXZ spin-1/2 Hamiltonian, given by

$$
H = \sum_{i,j} \left[-\frac{1}{2} \left(S_{i+1,j}^+ S_{i,j}^- + S_{i,j+1}^+ S_{i,j}^- + \text{H.c.} \right) + \Delta_1 \left(S_{i,j}^z S_{i+1,j}^z + S_{i,j}^z S_{i,j+1}^z \right) \right]
$$
$$
+ \sum_{i,j} \left[-\frac{J_2}{2} \left(S_{i+1,j+1}^+ S_{i,j}^- + S_{i-1,j+1}^+ S_{i,j}^- + \text{H.c.} \right) + \Delta_2 \left(S_{i,j}^z S_{i+1,j+1}^z + S_{i,j}^z S_{i-1,j+1}^z \right) \right]
$$
$$
+ \sum_{i,j} \left[-\frac{J_3}{2} \left(S_{i+2,j}^+ S_{i,j}^- + S_{i,j+2}^+ S_{i,j}^- + \text{H.c.} \right) + \Delta_3 \left(S_{i,j}^z S_{i+2,j}^z + S_{i,j}^z S_{i,j+2}^z \right) \right] - h_0 \sum_{i,j} S_{i,j}^z.
$$

(3.19)

Looking at Eqs. (3.18) and (3.19), one can easily see that $J_2 = t_2/t_1$, $J_3 = t_3/t_1$, $\Delta_1 = V_1/(2t_1)$, $\Delta_2 = V_2/(2t_1)$, $\Delta_3 = V_3/(2t_1)$ and $h_0 = E_p + 2V_z - 2V_1 - 2V_2 - 2V_3$; here, J_i and Δ_i are the transverse and longitudinal couplings, respectively.

Now, to figure out the phase diagram of the system, we need to study the Hamiltonian at various filling-fractions of HCBs. To vary the number of HCBs in the system, or in other words to tune the magnetization of the spin-1/2 system, we replace the constant h_0 by a
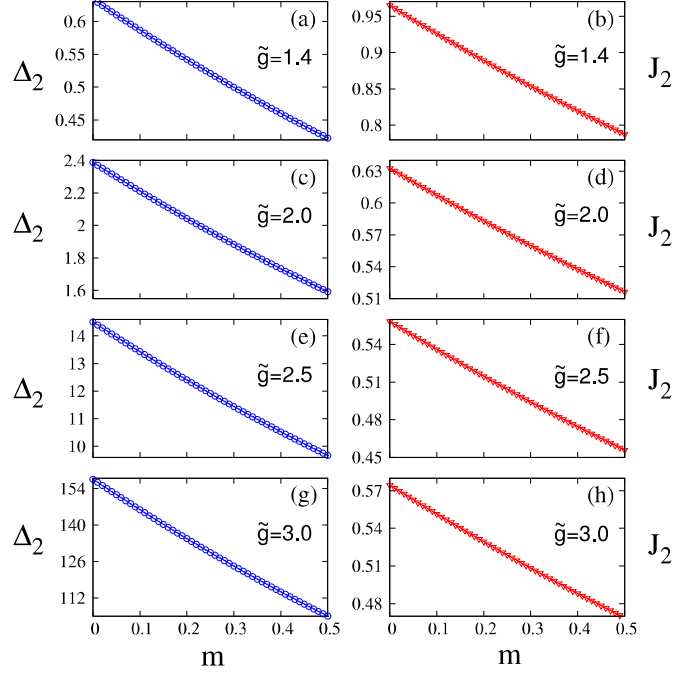
Figure 3.2: Dependence of NNN longitudinal coupling Δ_2 and NNN transverse coupling J_2 on magnetization m as derived from Eqs. (3.12), (3.16), (3.18), and (3.19) for the following cases: (a) & (b) at $\tilde{g} = 1.4$; (c) & (d) at $\tilde{g} = 2.0$; (e) & (f) at $\tilde{g} = 2.5$; and (g) & (h) at $\tilde{g} = 3.0$.

variable h in the term $-h_0 \sum_{i,j} S_{i,j}^z$ of the Hamiltonian H given by Eq. (3.19); here h is taken as the external magnetic field in units of $2t_1$. By tuning the external magnetic field h, we can actually tune the magnetization of the system and study the behavior of the system at various fillings.

To capture the ground-state properties of a $L \times L$ square lattice using SSE, the simulations should be done at low enough temperatures, i.e., the inverse temperature $\beta \sim L$ [113]. For our Hamiltonian, since the numerical calculations for $\beta = 3L/2$ and $\beta = 2L$ produce same results within the error bars of our calculations, we present the results for $\beta = 3L/2$.

We use two kinds of order parameter: structure factor $S(\vec{Q})$ (to identify diagonal long-

$\tilde{g}$	Δ_1	$(\Delta_2)_{max}$	$(J_2)_{max}$
1.0	1.7436	0.4757	1.6486
1.5	5.7744	0.7379	0.8760
1.8	16.6463	1.3791	0.7007
2.0	39.2161	2.3887	0.6327
2.25	131.8584	5.4612	0.5818
2.5	507.9968	14.5044	0.5584
3.0	10896.8217	157.5599	0.5744

Table 3.1: Values of NN longitudinal coupling Δ_1 and maximum values of NNN longitudinal coupling Δ_2 and NNN transverse coupling J_2 for different values of $\tilde{g}$.

range order) and superfluid density ρ_s (to identify off-diagonal long-range order) and construct the phase diagram. The structure factor per site is defined as

$$S(\vec{Q}) = \frac{1}{N_s^2} \sum_{i,j} \sum_{m,n} e^{i\vec{Q}\cdot(\vec{R}_{i,j} - \vec{R}_{m,n})} \langle S_{i,j}^z S_{m,n}^z \rangle, \tag{3.20}$$

with $\langle ... \rangle$ being the ensemble average and N_s the total number of sites. We study $S(\vec{Q})$ at all values of $\vec{Q}$ and identify those that produce peaks in the structure factor. Here we would like to point out that the maximum possible value of $S(\vec{Q})$ is 0.25.

The superfluid density is expressed in terms of the winding numbers, W_x and W_y, in the x and y directions as [112]

$$\rho_s = \frac{1}{2\beta} \langle W_x^2 + W_y^2 \rangle. \tag{3.21}$$

The winding number W_x along the x direction can be calculated as $W_x = \frac{1}{L_x}(N_x^+ - N_x^-)$, where N_x^+ and N_x^- denote the total number of operators transporting spin in positive and negative x directions, respectively and L_x denotes the length of the lattice along the x direction.

We now discuss the values of different parameters in our Hamiltonian given by Eq.
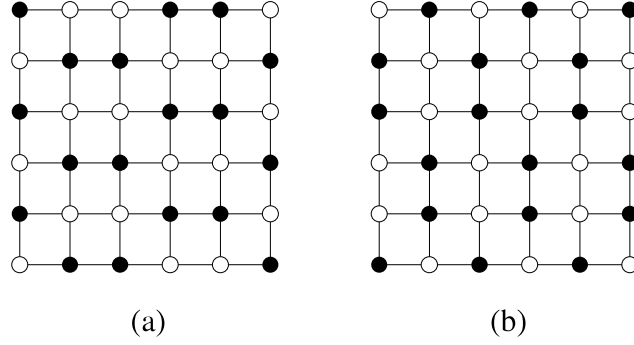
Figure 3.3: Two types of honeycomb-like solid depicted by a peak in (a) $S(\pi/2, \pi)$ and (b) $S(\pi, \pi/2)$.

(3.19) and used in our numerical calculations. We concentrate on the case $t/\omega_0 = 1.0$ for the construction of our phase diagram. Since $\gamma = \sqrt{2}$, we set $\tilde{g}^2 = 7g^2$ so as to get the simple expression $E_p + V_p = \tilde{g}^2\omega_0$. The coefficients $J_2 \,(= 2J_3)$ and $\Delta_2 \,(= 2\Delta_3)$ depend on the magnetization m of the system. While Fig. 3.2 depicts that J_2 and Δ_2 values (at various couplings $\tilde{g}$) monotonically decreases with increasing magnetization m, Table 4.1 shows the values of Δ_1 and the maximum values of Δ_2 and J_2 for different values of $\tilde{g}$. As one can see, $\Delta_1/(\Delta_2)_{\max}$ increases monotonically approximately from 3.665 to 69.159 as $\tilde{g}$ is varied from 1.0 to 3.0. At larger values of $\tilde{g}$, when Δ_1 and Δ_2 assume large values, our numerical calculations suffer from significant slowing down resembling the situation in Ref. [20]; with our computational constraints we cannot use exact values when Δ_1 and Δ_2 assume large values. We can set a cut-off for the parameters Δ_1 and Δ_2 above which the essential physics for our system remains unaltered. Similar to Ref. [20], the upper cut-off for Δ_1 is 16. Furthermore, to identify the cut-off for Δ_2, we need to find out the lowest value of Δ_1/Δ_2 which can be used without changing the essential physics. To this end, we have calculated the superfluid density and structure factor at half-filling (where $\Delta_2 = (\Delta_2)_{\max}$) for the following set of values of $(\Delta_1, (\Delta_2)_{\max})$: $(20, 4)$, $(20, 5)$, $(20, 6)$, $(16, 5)$, $(20, 7)$, $(17, 6)$, $(16, 7)$, and $(20, 9)$ with the value of $\Delta_1/(\Delta_2)_{\max}$ being 5, 4, 3.33,

h	5.0	13.0	15.35	29.50	34.0
τ_{int}	279692	55792	147933	192790	5747

Table 3.2: Autocorrelation times measured for $\tilde{g} = 2.5$ using $\epsilon_1 = 8$, $\epsilon_2 = 5/4$ and $\epsilon_3 = \epsilon_2/2$; chosen magnetic fields are in the vicinity of the transitions as well as away from the transitions (see Fig. 3.8 for details).

3.2, 2.86, 2.83, 2.29, and 2.22, respectively. Numerical results show that for the first four cases, where $\Delta_1 > 3(\Delta_2)_{\max}$, at half-filling the system manifests a checkerboard solid (cS) with a peak in the structure factor $S(\pi, \pi)$. On the other hand, for the last four cases where $2(\Delta_2)_{\max} < \Delta_1 < 3(\Delta_2)_{\max}$, at half-filling the system produces a completely different type of solid depicted in Fig. 3.3 (which we call honeycomb-like solid), indicated by a peak in $S(\pi/2, \pi)$ or $S(\pi, \pi/2)$. The reason can be explained as follows. In the cS phase each particle feels $6(\Delta_2)_{\max}$ amount repulsion, whereas in the honeycomb-like solid the repulsion felt by each particle is $\Delta_1 + 3(\Delta_2)_{\max}$. The checkerboard solid will be favored over the honeycomb-like solid only if $\Delta_1 + 3(\Delta_2)_{\max} > 6(\Delta_2)_{\max}$, i.e., $\Delta_1 > 3(\Delta_2)_{\max}$. Therefore to capture the correct physics of our system, the minimum value of Δ_1/Δ_2 must be greater than 3. Keeping all these facts in mind, we set the cut-off values to be $\Delta_1 = 16$ and $\Delta_2 = 5$ (with $\Delta_3 = \frac{\Delta_2}{2}$), so that the physics of the system still remains the same.

As discussed in Ref. [20], it is important to mention here that the parameter ϵ_i (see Appendix D for details), introduced to make the two-spin matrix elements positive, can affect the autocorrelation time especially for large anisotropies (i.e., large values of Δ_1, Δ_2 and Δ_3). To ensure that the autocorrelation time is much smaller than the bin size used to calculate the observables (in all the cases considered), we compute the autocorrelation time τ_{int} given by the following formula,

$$\tau_{int}[m] = \frac{1}{2} + \sum_{t=1}^{\infty} A_m(t), \tag{3.22}$$
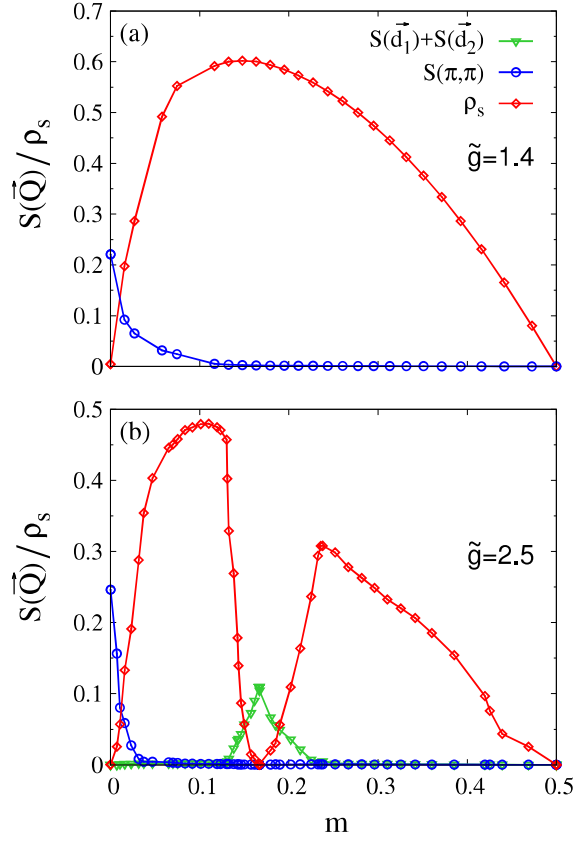
Figure 3.4: Plots of structure factor $S(\vec{Q})$ and superfluid density ρ_s vs magnetization m for HCBs on a 18×18 lattice with $t/\omega_0 = 1.0$ and when (a) $\tilde{g} = 1.4$ and (b) $\tilde{g} = 2.5$. Curves are averaged results from simulations using three different random number seeds.

with

$$A_m(t) = \frac{\langle m(i+t)m(i) \rangle - \langle m(i) \rangle^2}{\langle m(i)^2 \rangle - \langle m(i) \rangle^2}, \tag{3.23}$$

where i and t represent Monte Carlo sweeps and $\langle \cdots \rangle$ denotes average over the time i. Based on our autocorrelation data, we observe that when $\Delta_i \leq 10$, taking $\epsilon_i = \Delta_i/4$ is good enough to keep the autocorrelation time much smaller than the bin size. Given the cut-off values of Δ_2 and Δ_3 mentioned above, we always take $\epsilon_2 = \Delta_2/4$ and $\epsilon_3 =$

$\Delta_3/4$. On the other hand, as Δ_1 increases from 10 to 16 (i.e., cut-off value of Δ_1), ϵ_1 is taken to steadily increase from $\Delta_1/4$ (i.e., 2.5) to $\Delta_1/2$ (i.e., 8). To give an estimate of the autocorrelation time at large Δ_1 values, Table 3.2 shows the autocorrelation times for $\tilde{g} = 2.5$ at magnetic fields chosen in the vicinity of the phase transitions (where the autocorrelation time is expected to be large) as well as in regions far from the transitions. In Table 3.2, the magnetic field $h = 5.0$ corresponds to a point in the cSS region close to the cSS-SF transition; whereas $h = 15.35$ and 29.50 represent points in the dsSS region in the vicinity of the dsSS-SF transition (see Fig. 3.8). On the other hand, $h = 13.0$ and 34.0 correspond to two points in the SF region away from the transitions. The values of the autocorrelation time τ_{int} (listed in Table 3.2) clearly show that close to the transitions the autocorrelation time increases significantly, whereas it remains comparatively small in the regions away from the transitions. The bin size used for all calculations is $20, 00, 000$; this ensures that τ_{int} is well within the bin size.

All numerical results in Figs. 3.4–3.11 have been obtained on a 18×18 lattice with $t/\omega_0 = 1.0$. Furthermore, along with the 18×18 phase diagram, in Fig. 3.6, the phase boundaries for a 12×12 lattice are also plotted.

3.4   Results and Discussions

To determine the various phases of our 2D $t_1 - t_2 - t_3 - V_1 - V_2 - V_3$ model, one needs to understand the interplay between different types of hopping and repulsion. To construct the phase diagram, we vary the magnetization m from 0 to 0.5; this corresponds to varying the particle filling ρ from $1/2$ to 1. Due to particle-hole symmetry of the Hamiltonian, the physics at any filling-fraction for particles is identical to that for holes at the same filling.

Figure 3.4 shows the variation of the structure factor $S(\vec{Q})$ and the superfluid density
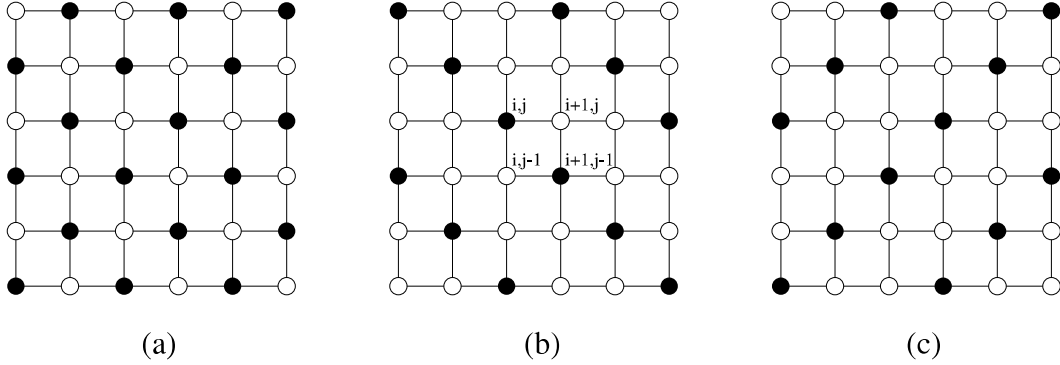
Figure 3.5: Different types of CDWs: (a) checkerboard solid (cS) at half-filling with $S(\vec{Q})$ peaking at $\vec{Q} = (\pi, \pi)$; (b) diagonal striped solid (dsS) indicated by peak in $S(\vec{Q})$ at $\vec{Q} = (2\pi/3, 2\pi/3)$; and (c) dsS characterized by ordering wavevector $\vec{Q} = (2\pi/3, 4\pi/3)$.

ρ_s as a function of the magnetization m, for two different values of $\tilde{g}$, i.e., 1.4 and 2.5. A key point to note here is that, in general, larger values of repulsion aid in the formation of a CDW, whereas larger values of NNN tunneling t_2 help a particle hop in the same sublattice. For $\tilde{g} = 1.4$, at half-filling, the HCBs form a checkerboard solid shown in Fig. 3.5(a) and indicated by a peak in the structure factor $S(\pi, \pi)$. Slightly away from half-filling, a supersolid region develops after which the system retains only its superfluidity. The reason can be understood by examining the coefficients of different terms in the Hamiltonian in Eq. (3.19). Since the NN repulsion dominates over the NNN and NNNN repulsions, at half-filling the system becomes a cS phase to avoid NN occupation, even though the particles experience NNN and NNNN repulsions.

Now, if we add one additional particle to the half-filled system, the extra particle can be at any one of the empty sites; irrespective of the site it resides on, the particle will feel the same extra repulsion $4V_1$. This extra particle can hop to its NNN or NNNN sites, without changing the repulsive interaction in the system which has a checkerboard solid in the background, resulting in the coexistence of superfluidity and CDW state. If we keep on increasing the particle number, after a certain filling-fraction, the checkerboard structure is

lost with the system continuing to be a superfluid.

Now looking at Fig. 3.4(b) for $\tilde{g} = 2.5$, we see that an additional CDW appears at fillings $\rho = 1/3$ and $2/3$. Since the physics pertinent to $\rho = 1/3$ is the same as that for $\rho = 2/3$, we will analyze them interchangeably based on our convenience. At $\rho = 1/3$, the HCBs form a diagonal striped solid manifesting spontaneously broken symmetry and characterized by a peak in the structure factor at wavevector $\vec{d_1} = (2\pi/3, 2\pi/3)$ [corresponding to Fig. 3.5(b)] or $\vec{d_2} = (2\pi/3, 4\pi/3)$ [related to Fig. 3.5(c)]. Although each particle in the stripe experiences a repulsion $2V_2$, it is still the minimum energy state of the system at one-third filling. If we add one extra particle to the system, it occupies any one of the empty sites between the stripes and experiences a repulsion $2V_1 + V_2 + 2V_3$. Now, this extra particle can hop to any of its unoccupied NN, NNN, or NNNN sites without a change in the potential energy of the system; thus, coexistence of stripe order and superfluidity is realized on the interstitial side. On the other hand, if we remove one particle from the system at $\rho = 1/3$, the extra hole (residing in the stripes) can hop along the stripes without altering the potential energy; thus, supersolidity is exhibited on the other (i.e., vacancy) side of the diagonal striped phase as well. Thus, the mechanism governing the existence of a supersolid phase away from commensurate fillings $1/2$ and $1/3$, on our unfrustrated system (i.e., the square lattice), is that interstitials or vacancies can move without frustration, i.e., without a cost in the potential energy.

The complete ground-state phase diagram is depicted in Fig. 3.6 for 12×12 and 18×18 square lattices; we see that the phase diagram is by and large independent of the system size for $6L \times 6L$ square lattices when $L \geq 2$. It should be noted that, for $L \geq 4$, the simulation times are prohibitively large at large repulsions (or anisotropies). We will now proceed to discuss the phase diagram for the 18×18 lattice. The half-filled system shows the signature of a checkerboard solid (cS) for all $\tilde{g}$ values above 1.37. Next to this CDW,
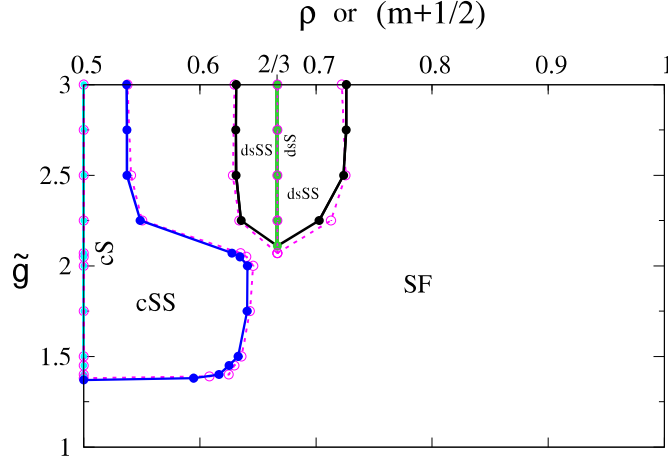
Figure 3.6: Phase diagram in terms of filling-fraction ρ (or magnetization m) for HCBs on a 12×12 and 18×18 lattice with $t/\omega_0 = 1.0$. The magenta dashed lines and open circles represent the phase boundaries for the 12×12 system, whereas the boundaries for the 18×18 lattice are depicted by the solid lines and filled circles (i.e., in cyan, blue, black and green colors). Here cS represents checkerboard solid with cSS being the corresponding supersolid; dsS stands for diagonal striped solid with dsSS being the related supersolid. Plots represent averaged results from simulations employing three different random number seeds.

we have a supersolid region (cSS) where $S(\pi, \pi)$ and ρ_s coexist homogeneously. On the other hand, at filling fraction $\rho = 1/3$, the system realizes a dsS beyond $\tilde{g} = 2.11$. On both sides of this striped solid, we have a region of supersolid (dsSS) which is a homogeneous coexistence of the diagonal striped solid and a superfluid. As we increase $\tilde{g}$ beyond 1.37, the width of the supersolid region cSS increases and attains its maximum at $\tilde{g} = 2.0$. Further increase in $\tilde{g}$ results in a decrease in the width of the cSS region, thereby making way for diagonal stripe supersolid at higher values of $\tilde{g}$. However, we should point out that there is no direct supersolid-supersolid transition. Next, it is interesting to note that there is an asymmetry in the extent of the dsSS region around one-third filling. Thus, there is an asymmetry at $\rho = 1/3$ with respect to doping with interstitials and vacancies similar to the asymmetry at one-fourth filling reported in Ref. [15] for a $t_1 - V_1 - V_2$ model when
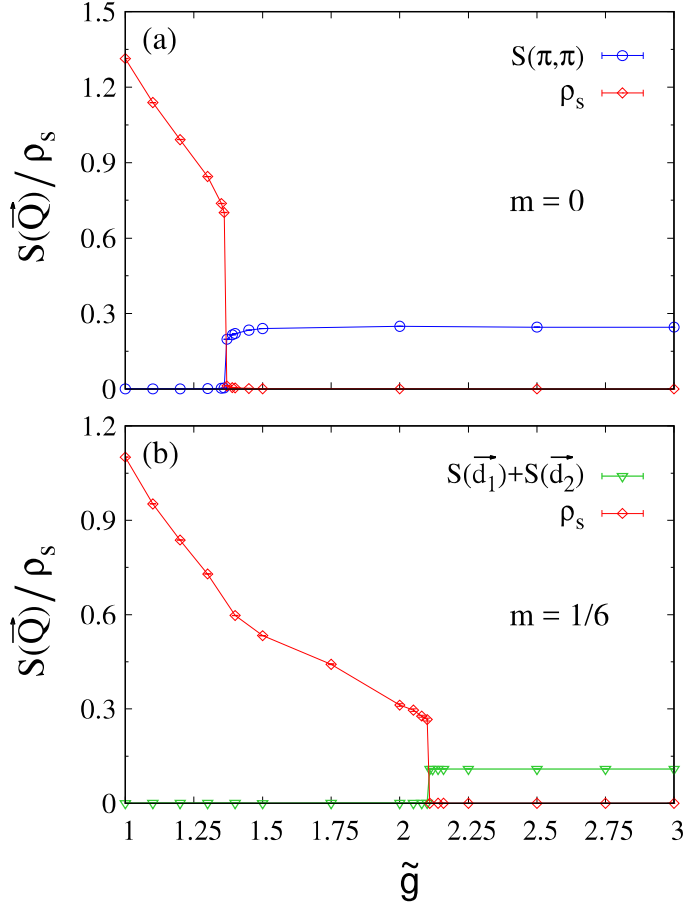
Figure 3.7: Plots of $S(\vec{Q})$ and ρ_s vs coupling strength $\tilde{g}$ depicting first-order transitions at two different magnetization values: (a) $m = 0$ (or half-filling) and (b) $m = 1/6$ (or two-third filling).

$V_1 < 2V_2$. It is also worth noting that, at lower fillings such as $\rho = 1/4$ and $\rho = 1/5$, there is no CDW order.

In a recent study of HCBs on a square lattice with NN hopping and NN repulsion (i.e., in a $t_1 - V_1$ model), when a sizeable external potential is applied along the diagonal stripes in Figs. 3.5(b) and 3.5(c), the authors obtain the corresponding diagonal striped CDW at $\rho = 1/3$ and a striped supersolid phase away from one-third filling [114]. Similar to our case, the physics governing the formation of a supersolid phase is that the interstitial

particles or vacancies in the vicinity of the commensurate filling $\rho = 1/3$ can hop without changing the potential energy of the system.

In our simulations using SSE, we cannot tune the magnetization (density) directly. Instead, we tune the magnetic field which determines the magnetization of the system. For a particular value of the magnetic field, the resulting magnetization generally fluctuates during simulation. As a result, usually it is not possible to study the nature of the phase transitions by keeping the magnetization (filling-fraction) fixed at a particular value and varying $\tilde{g}$. However, when the system is in a CDW state, the magnetization remains constant over a range of magnetic field values; this makes it possible to vary $\tilde{g}$ at a fixed magnetization.

We see from Fig. 3.7(a) that for the half-filled system (i.e., at $m = 0$), as we increase the $\tilde{g}$ value from 1 to 3, the structure factor $S(\pi, \pi)$ jumps from 0 to almost its maximum value and the superfluid density suddenly drops down to zero at $\tilde{g} = 1.37$. In the phase diagram (depicted in Fig. 3.6), this indicates a first-order transition at $\tilde{g} = 1.37$ from a superfluid to a checkerboard solid at filling-fraction $\frac{1}{2}$; since the transition is from a U(1) symmetry breaking state to a translational symmetry breaking state, the order of the transition is consistent with Landau's picture. Furthermore, our observation of discontinuous transition from a superfluid to checkerboard solid is also consistent with the results of Refs. [30, 115]. Similarly at magnetization $m = \frac{1}{6}$ corresponding to filling fraction $\frac{2}{3}$, at $\tilde{g} = 2.11$, Fig. 3.7(b) shows a dramatic jump in the structure factor $S(2\pi/3, 2\pi/3) + S(2\pi/3, 4\pi/3)$ from 0 to its maximum value accompanied by a discontinuous drop in the superfluid density to zero. This signifies a first-order transition as we move along the $\tilde{g}$-axis at $m = 1/6$ in the phase diagram (shown in Fig. 3.6). Thus, consistent with the literature [15, 17, 116], no supersolidity is detected at commensurate fillings in our unfrustrated system. Here it should be pointed out that in Fig. 3.7(a) and 3.7(b), after the transition from superfluid to
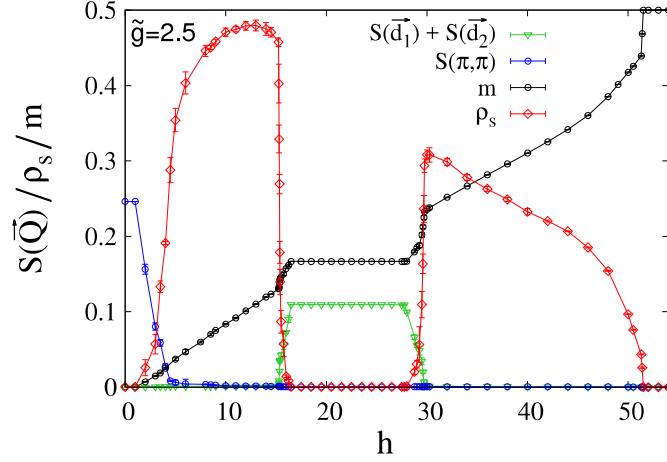
Figure 3.8: Evolution of order parameters $S(\vec{Q})$, ρ_s and m as the magnetic field h is varied at a fixed coupling strength $\tilde{g} = 2.5$. No discontinuous transitions are exhibited.

CDW (cS and dsS) state, the magnetizations can be fixed exactly at $m = 0$ and $m = 1/6$, respectively. But before the transitions, i.e., in the superfluid region, the magnetizations are given by $m = 0 \pm 0.0000006$ and $m = 1/6 \pm 0.00002$.

Next, away from the special points [117] ($\rho = 0.5$, $\tilde{g} = 1.37$) and ($\rho = 2/3$, $\tilde{g} = 2.11$), we will study the nature of the transitions as a function of the magnetization. As seen in Fig. 3.4, the order parameters change continuously, upon tuning the magnetization of the system at a fixed $\tilde{g}$ value, signifying continuous phase transitions between different phases. A more reliable indicator, to detect the nature of the phase transitions along the ρ-axis of the phase diagram, is the behavior of the order parameters (i.e., magnetization, superfluid density and structure factor) as the magnetic field h is varied. In Fig. 3.8, the continuous variation of the order parameters as a function of the magnetic field h clearly eliminates the possibility of a first-order phase transition. Therefore, in the phase diagram displayed in Fig. 3.6, as we move along the ρ-axis at any particular $\tilde{g}$ value, all the different phases are separated from each other via continuous phase transitions, i.e., all supersolid-solid and superfluid-supersolid transitions are continuous.
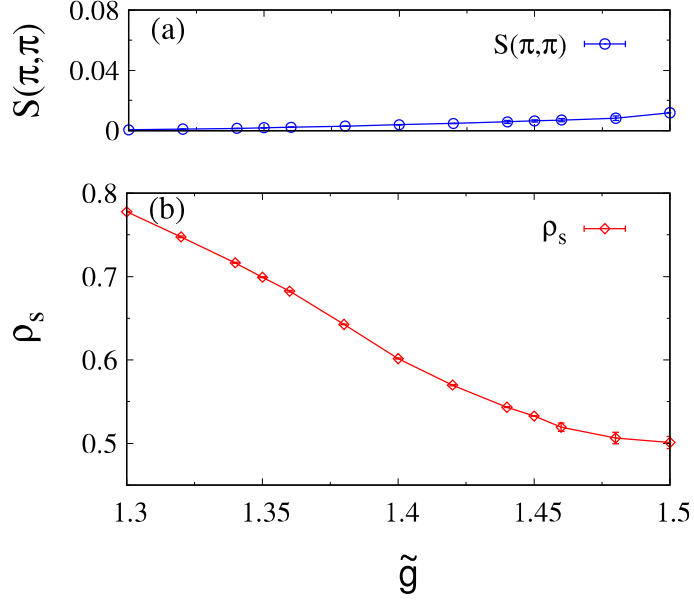
Figure 3.9: Plots of (a) $S(\pi, \pi)$ and (b) ρ_s vs coupling strength $\tilde{g}$, at density $\rho = 0.61635 \pm 0.00007$, depicting a continuous transition from SF to cSS phase as we increase the $\tilde{g}$ value.

As mentioned earlier, at a fixed magnetization, it is difficult to analyze the transition between the superfluid and the supersolid phases as a function of $\tilde{g}$. Now, it is expected that the nature of the transition between the two phases is independent of whether it is driven by the coupling or the density. To demonstrate this, we concentrate on the phase transition between SF and cSS. From the phase diagram in Fig. 3.6, we see that around $\rho \approx 0.616$, a phase transition takes place between SF and cSS as $\tilde{g}$ is varied from 1.35 to 1.40. Therefore, for a number of $\tilde{g}$ values ranging from 1.3 to 1.5, we have varied the magnetic field (in very small steps) so as to obtain the density ρ as close as possible to 0.616 for each $\tilde{g}$. Fig. 3.9 shows the behavior of $S(\pi, \pi)$ and ρ_s as a function of $\tilde{g}$ at density $\rho = 0.61635 \pm 0.00007$. The smooth variation of the order parameters suggest that the nature of the transition between superfluid (SF) and checkerboard supersolid (cSS) is continuous as we move along the $\tilde{g}$-axis in the phase diagram. Similarly, we expect the
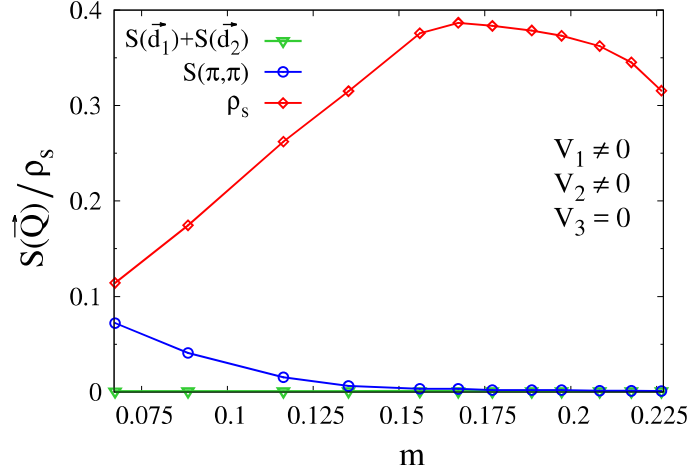
Figure 3.10: Variation of $S(\vec{Q})$ and ρ_s vs magnetization m in the absence of the NNNN repulsion V_3 along x- and y-axes in the $t_1 - t_2 - t_3 - V_1 - V_2 - V_3$ model of Eq. (3.18).

nature of the transition to be also continuous between the superfluid (SF) and diagonal striped supersolid (dsSS) phases as we tune the $\tilde{g}$ value.

We will now identify the minimum model for the diagonal striped supersolid. Compared to the checkerboard supersolid, the dsSS phase is rarely observed. To determine the minimum model for the realization of the dsSS phase, we first identify the necessary repulsions required to observe the diagonal striped solid phase in the $t_1 - t_2 - t_3 - V_1 - V_2 - V_3$ model of Eq. (3.18). From Fig. 3.10, we see that, as soon as we tune the NNNN repulsion V_3 along x and y axes to zero, the structure factor corresponding to the dsS phase completely disappears. This feature can be explained based on Figs. 3.5(b) and 3.5(c). For instance, when the NNNN repulsion V_3 is set to zero in the structure given by Fig. 3.5(b), the particles at sites (i, j) and $(i + 1, j - 1)$ can both be shifted to the neighboring sites (i+1,j) and (i,j-1) without changing the potential energy of the system. This process destroys the striped structure. Thus, it follows that all the three repulsions (i.e., V_1, V_2, and V_3) are necessary to stabilize the dsS structure. A similar argument can be made to destroy the structure given by Fig. 3.5(c).

106
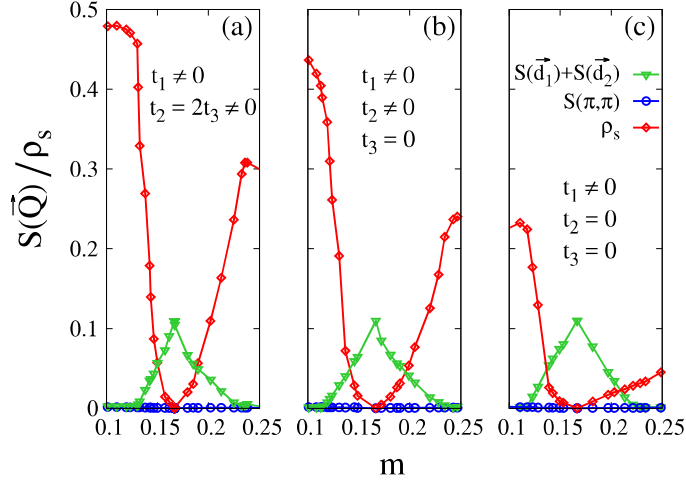
Figure 3.11: Plots of $S(\vec{Q})$ and ρ_s vs magnetization m, in the vicinity of striped phase, for three different cases in the $t_1 - t_2 - t_3 - V_1 - V_2 - V_3$ model of Eq. (3.18): (a) all the three hoppings t_1, t_2, and t_3 are present; (b) NNNN hopping t_3 along x- and y-axes is set to zero; and (c) only NN hopping t_1 is present. The minimum model for diagonal striped solid (dsS) is shown to be $t_1 - V_1 - V_2 - V_3$.

Next, in Fig. 3.11, we focus on the region in the vicinity of the striped phase. Compared to Fig. 3.11(a), in which all the three hopping parameters are non-zero, the superfluid density reduces slightly when the NNNN hopping t_3 is set to zero [as can be seen in Fig. 3.11(b)]. The interesting feature to note is that, even when only NN hopping t_1 is present with the other two hopping parameters t_2 and t_3 being zero [as in Fig. 3.11(c)], we have a diagonal striped supersolid region around $m = 1/6$ with the width of the dsSS being almost unaffected. This elucidates the fact that the minimum model to obtain a dsSS phase is the $t_1 - V_1 - V_2 - V_3$ model.

3.5   Comparison with LSNO experimental results

Stripe-like charge order has been reported in a number of layered transition-metal oxides [45]. Among these compounds, the layered nickelate LSNO is an archetypal system to

exhibit a firm charge stripe order. In $La_{2-x}Sr_xNiO_4$, static checkerboard charge order [such as in Fig. 3.5(a)] is expressed at $x = 1/2$ and static diagonal stripe order [as shown in Figs. 3.5(b) and 3.5(c)] is manifested at $x = 1/3$ with the transition temperatures at these dopings showing local maxima [46–51]. The observed lattice constant ratio c/a in LSNO displays a maximum at $x = 1/2$, thereby indicating that in the region $0 < x < 1/2$ holes are doped into the $d_{x^2-y^2}$ orbitals and in the region $1/2 < x < 1$ holes are doped into the d_{z^2} orbitals [48, 118]. Measurements of Hall coefficient for $La_{2-x}Sr_xNiO_4$ by T. Katsufuji *et al.* [119], revealed that the charge carriers change from electron-like to hole-like while going from the hole density $x < 1/3$ to $x > 1/3$.

In the undoped La_2NiO_4, the oxidation state of nickel is Ni^{2+} with the electronic configuration $[Ar]4s^03d^8$. Hence, only d_{z^2} and $d_{x^2-y^2}$ orbitals are relevant in the doped compound $La_{2-x}Sr_xNiO_4$. The e-ph interaction term of the Hamiltonian is given by

$$H_{ep} = -\frac{g\omega_0}{4}\sum_{i,j}\left(d^\dagger_{z^2;i,j}\ d^\dagger_{x^2-y^2;i,j}\right)\begin{pmatrix} q_{x;i,j} + q_{y;i,j} + 4q_{z;i,j} & -\sqrt{3}q_{x;i,j} + \sqrt{3}q_{y;i,j} \\ -\sqrt{3}q_{x;i,j} + \sqrt{3}q_{y;i,j} & 3q_{x;i,j} + 3q_{y;i,j} \end{pmatrix}\begin{pmatrix} d_{z^2;i,j} \\ d_{x^2-y^2;i,j} \end{pmatrix},$$

$$(3.24)$$

where the distortions $q_{x;i,j} \equiv (a^\dagger_{x;i,j} + a_{x;i,j}) - (a^\dagger_{x;i-1,j} + a_{x;i-1,j})$, $q_{y;i,j} \equiv (b^\dagger_{y;i,j} + b_{y;i,j}) - (b^\dagger_{y;i,j-1} + b_{y;i,j-1})$, and $q_{z;i,j} \equiv (c^\dagger_{z;i,j} + c_{z;i,j})$. In the undoped compound, since both d_{z^2} and $d_{x^2-y^2}$ orbitals are occupied, there are only breathing mode distortions ($4q_{x;i,j} + 4q_{y;i,j} + 4q_{z;i,j}$) and no active Jahn-Teller (JT) distortions. Now, when we introduce holes in the system (by doping with Sr such that $0 < x < 1/2$), the holes occupy the $d_{x^2-y^2}$ orbitals; this is because a site with a single electron in $d_{x^2-y^2}$ orbital will produce in-plane distortions ($3q_x + 3q_y$) which have a greater incompatibility with the breathing mode distortions ($4q_x + 4q_y + 4q_z$) on the adjacent sites and thus cost more energy than a singly

occupied d_{z^2} orbital. These $d_{x^2-y^2}$ holes can hop and are responsible for the transport properties. Each site with a $d_{x^2-y^2}$ hole is JT active.

The Hamiltonian for cooperative Jahn-Teller (CJT) distortions in the two-dimensional LSNO system involves holes in $d_{x^2-y^2}$ orbitals as the active carriers. The starting Hamiltonian H_{LSNO}, describing $\mathrm{La}_{2-x}\mathrm{Sr}_x\mathrm{NiO}_4$ for $0 \le x \le 0.5$, consists of the following terms expressed in terms of the creation (destruction) operator $h^\dagger_{i,j}(h_{i,j})$ for the holes in $d_{x^2-y^2}$ orbitals.

(i) Hopping term

$$H'_t = \frac{3t}{4} \sum_{i,j} \left(h^\dagger_{i+1,j} h_{i,j} + h^\dagger_{i,j+1} h_{i,j} + \mathrm{H.c.} \right); \qquad (3.25)$$

(ii) hole-phonon interaction term:

$$H'_I = \frac{3}{4} g \omega_0 \sum_{i,j} \left[(a^\dagger_{x;i,j} + a_{x;i,j})(n^h_{i,j} - n^h_{i+1,j}) + (b^\dagger_{y;i,j} + b_{y;i,j})(n^h_{i,j} - n^h_{i,j+1}) \right]; \quad (3.26)$$

and (iii) lattice term:

$$H'_l = \omega_0 \sum_{i,j} \left(a^\dagger_{x;i,j} a_{x;i,j} + b^\dagger_{y;i,j} b_{y;i,j} \right), \qquad (3.27)$$

where $n^h_{i,j} \equiv h^\dagger_{i,j} h_{i,j}$.

The Lang-Firsov transformed Hamiltonian is given by $\tilde{H}_{\mathrm{LSNO}} = \exp(S)\, H_{\mathrm{LSNO}} \exp(-S)$ where S has the form

$$S = \frac{3}{4} g \sum_{i,j} \left[(a^\dagger_{x;i,j} - a_{x;i,j})(n^h_{i,j} - n^h_{i+1,j}) + (b^\dagger_{y;i,j} - b_{y;i,j})(n^h_{i,j} - n^h_{i,j+1}) \right]. \qquad (3.28)$$

Setting $t' = -3t/4$ and $g' = -3g/4$, in the non-adiabatic regime ($|t'|/\omega_0 \leqslant 1$) and at

strong coupling (i.e., large g'^2), the transformed Hamiltonian can be split into two terms: the unperturbed Hamiltonian and the perturbation term. These two terms are the same as the ones given by Eqs. (3.5) and (3.6), except that they are written in hole-operator language; both γ and η are set to zero value; and t and g are replaced by t' and g', respectively. If the carriers are taken to be HCBs instead of fermionic holes, then after following the same second-order perturbative procedure as in Sec. 3.2, we end up with an effective Hamiltonian that is exactly the same as that given by Eq. (3.18) with $\gamma = 0 = \eta$ and with t and g being replaced by t' and g', respectively. It is important to note that the small parameter value is again given by $\left[\frac{t^2}{2(E_p + V_p)\omega_0} \right]^{\frac{1}{2}}$ and remains unaltered. Now, since we are dealing with fermionic holes and not HCBs, we get the following effective Hamiltonian:

$$
\begin{aligned}
H'_{\text{eff}} = & -(E_p + 2V_z) \sum_{i,j} n^h_{i,j} \\
& - t_1 \sum_{i,j} \left(h^\dagger_{i+1,j} h_{i,j} + h^\dagger_{i,j+1} h_{i,j} + \text{H.c.} \right) + V_1 \sum_{i,j} \left(n^h_{i,j} n^h_{i+1,j} + n^h_{i,j} n^h_{i,j+1} \right) \\
& - t_2 \sum_{i,j} \left(h^\dagger_{i+1,j+1} (1 - n^h_{i+1,j} - n^h_{i,j+1}) h_{i,j} + h^\dagger_{i-1,j+1} (1 - n^h_{i-1,j} - n^h_{i,j+1}) h_{i,j} + \text{H.c.} \right) \\
& + V_2 \sum_{i,j} \left(n^h_{i,j} n^h_{i+1,j+1} + n^h_{i,j} n^h_{i-1,j+1} \right) \\
& - t_3 \sum_{i,j} \left(h^\dagger_{i+2,j} (1 - 2n^h_{i+1,j}) h_{i,j} + h^\dagger_{i,j+2} (1 - 2n^h_{i,j+1}) h_{i,j} + \text{H.c.} \right) \\
& + V_3 \sum_{i,j} \left(n^h_{i,j} n^h_{i+2,j} + n^h_{i,j} n^h_{i,j+2} \right),
\end{aligned}
\tag{3.29}
$$

with $\gamma = 0 = \eta$ and with t and g being replaced by t' and g', respectively. Since, the interaction terms for the CJT Hamiltonian of LSNO are the same as those for the $t_1 - t_2 - t_3 - V_1 - V_2 - V_3$ Hamiltonian in Eq. (3.18), in LSNO also we expect to get the same charge-ordered phases obtained for the $t_1 - t_2 - t_3 - V_1 - V_2 - V_3$ model. Thus. at hole

110

doping $1/2$ and $1/3$ (i.e., at $x = 1/2$ and $x = 1/3$ in $La_{2-x}Sr_xNiO_4$), we will realize checkerboard solid and diagonal stripes, respectively, which match exactly with the charge ordering obtained for LSNO experimentally.

Now, if we add one extra hole to the system at one-third hole doping (i.e., at $x = 1/3$), then the extra hole will reside in the region between two diagonal stripes. This extra hole can hop anywhere in the region between the stripes without changing the potential energy of the system. Thus, the carriers for the hole doping $x > 1/3$ are holes. On the other hand, adding one electron to the striped phase so that $x < 1/3$ will result in the extra electron occupying any one of the sites along the stripes; this extra electron is free to hop along the stripes without altering the potential energy of the system. This means that electrons are the carriers for the doping $x < 1/3$. Therefore, based on our model we can explain the hole or electron doping (into the charge-ordered Mott insulator $La_{5/3}Sr_{1/3}NiO_4$) that was reported by T. Katsufuji *et al.* [119].

One can obviously ask how a system of HCBs can reproduce some experimental results of a system of electrons. The reason behind the charge orderings at hole-doping values $1/2$ and $1/3$ is repulsion; hopping does not play any role in the ordering. Hence, for these two CDWs, it does not matter whether the carriers of the system are HCBs or electrons. Close to one-third doping, only single carrier physics plays a role; consequently, particle-hole asymmetry is captured. Next, it is important to note that CJT interaction is needed to generate NNN and NNNN repulsions V_2 and V_3 which in turn are needed to explain diagonal stripes. Thus, we see that our work resolves the controversy whether cooperative Jahn-Teller distortions can explain the observed diagonal-stripe charge order at one-third doping in LSNO [104–106]. Lastly, it should also be pointed out that, although experimentally [48] insulating behavior is observed in LSNO for $x \lesssim 0.9$, theoretically we expect metallic nature; we believe, this discrepancy is due to localization effects produced

by disorder in real LSNO systems.

3.6 Conclusions and open problems

To conclude, we investigated a 2D system of HCBs, modulated by the cooperative breathing mode, which is important in real materials such as $BaBiO_3$ and nickelates as well as in artificial cold-atom systems. Using a duality treatment, we obtained the effective Hamiltonian and generated the phase diagram employing the SSE technique.

In the phase diagram displayed in Fig. 3.6, a first-order transition occurs from a superfluid to a checkerboard solid at filling-fraction 1/2 and from a superfluid to a diagonal striped solid at filling 1/3. We interpreted the nature of the transition by invoking Landau's explanation. It would be interesting to verify whether in other unfrustrated lattices, such as the checkerboard lattice, a discontinuous superfluid-solid transition is manifested at commensurate fillings such as 1/4 [116]. Furthermore, at a fixed interaction strength, our $t_1 - t_2 - t_3 - V_1 - V_2 - V_3$ model realizes only continuous transitions (i.e., superfluid-supersolid and supersolid-solid transitions) as density is varied. Contrastingly, the $t_1 - t_2 - t_3 - V_1$ model (pertaining to the strong-coupling case of the Holstein model) manifests a discontinuous superfluid-supersolid transition when density is varied [20, 21]. Thus, more insight is needed to identify which class of models yield what type of superfluid-supersolid transition.

We have identified the $t_1 - V_1 - V_2 - V_3$ model as the minimum model for obtaining a diagonal striped supersolid on a square lattice. It would be exciting to realize this system in a cold-atom system, thereby adding to the understanding of lattice supersolidity generated by long-range interactions [12].

The asymmetry of the supersolid phase about a commensurate filling, such as one third

112

in our case and one fourth in the case of Ref. [15], in a square lattice occurs possibly because particle-hole symmetry is not respected by the Hamiltonian about these fillings. It would be worthwhile to study the nature of such asymmetry in other lattices such as honeycomb, checkerboard, etc.

We have explained the charge ordering in $La_{2-x}Sr_xNiO_4$ at hole-doping $x = 1/2$ and $1/3$ by considering cooperative Jahn-Teller effect. However, studies involving CJT effect are needed at dopings away from these fillings and particularly in the region $x > 1/2$ where holes are doped into the d_{z^2} orbitals. Also of interest would the explanation for the metal-insulator transition observed at $x \sim 0.9$ [48].

In a different but related system $La_{2-x}Sr_xCoO_4$, CDWs similar to those in LSNO are observed. At half doping, there is a signature of checkerboard charge ordering with alternate Co^{2+} and Co^{3+} ions (below $T_{CO} \approx 750K$) [120]. On the other hand, at the doping $x = 1/3$, the holes form a diagonal-stripe pattern similar to the stripes in LSNO at a transition temperature well above the room temperature [121–124]. Furthermore, the presence of substantial disorder in these diagonal stripes has been confirmed by the experiment [124] done by A. T. Boothroyd *et al.* The electronic configuration of cobalt is $[Ar]3d^74s^2$. In $La_{2-x}Sr_xCoO_4$, cobalt shows two different oxidation states: Co^{2+} and Co^{3+}. The Co^{3+} ions are found to have the low-spin ground state (S = 0) [125] with the electronic configuration $[Ar]3d^6$. In this case, all the six d electrons occupy the t_{2g} orbitals and both the e_g orbitals are empty. Therefore, Co^{3+} ions do not cause any Jahn-Teller distortion in the system. On the other hand, in the case of Co^{2+} ions, the electrons are in the high-spin ground state (S = 3/2) with the electronic configuration $[Ar]3d^7$. This state consists of five electrons in the t_{2g} orbitals and two in the e_g orbitals. Two out of the three t_{2g} orbitals are completely filled with four electrons, whereas the remaining orbital contains a single electron. Since both the e_g orbitals are occupied by one electron each, JT distortion comes

into play due to the singly occupied t_{2g} orbital only. Owing to the fact that the JT distortion arising from t_{2g} electrons is weaker than the one arising from e_g electrons, it needs to be examined whether this can explain the disorder in the stripe pattern in $La_{2-x}Sr_xCoO_4$.

CHAPTER 4

STUDY OF SUPERSOLIDITY IN THE TWO-DIMENSIONAL HUBBARD-HOLSTEIN MODEL

4.1 Introduction

Usually, diverse interactions can enrich the quantum phase diagram of the system by producing various competing/cooperating orders. Specifically, strong e-e interactions as well as strong e-ph interactions generate a rich phase diagram in systems such as the cuprates [83, 84], the manganites [86–88] and the fullerides [103]. In these correlated systems, a variety of exotic phases, such as superconductivity, CDW, spin-density-wave (SDW), etc. are manifested as an outcome of the interplay between e-e and e-ph interactions.

A typical and simple model, to study the combined effect of strong e-e and e-ph inter-

actions, is the well-known Hubbard-Holstein model represented by the following Hamiltonian:

$$H_{hh} = -t \sum_{j,\delta,\sigma} c^{\dagger}_{j+\delta\sigma} c_{j\sigma} + \omega_0 \sum_{j} a^{\dagger}_j a_j + g\omega_0 \sum_{j\sigma} n_{j\sigma}(a_j + a^{\dagger}_j) + U \sum_{j} n_{j\uparrow} n_{j\downarrow} \qquad (4.1)$$

where $c^{\dagger}_{j\sigma}$ ($c_{j\sigma}$) denotes the creation (destruction) operator for spin-σ electrons at site j, t is the hopping integral, and the number operator $n_{j\sigma} = c^{\dagger}_{j\sigma} c_{j\sigma}$. Furthermore, $a^{\dagger}_j (a_j)$ corresponds to the creation (destruction) operator of phonons at site j with dispersionless phonon frequency ω_0, g denotes the strength of the e-ph interaction, U is the onsite Coulomb repulsion between electrons, and δ represents the nearest-neighbors (NN).

The Hubbard-Holstein model has been studied extensively in one, two and infinite dimensions at various fillings by employing diverse approaches such as quantum Monte Carlo (QMC) [126–131], exact diagonalization [132–134], density matrix renormalization group (DMRG) [135, 136], dynamical mean field theory (DMFT) [137–145], semi-analytical slave boson approximations [146–150], variational methods based on Lang-Firsov transformation [151, 152], large-N expansion [153], Gutzwiller approximation [154, 155], cluster approximation [156] and static-auxiliary-field approximation [157, 158].

In this chapter, we follow the approach discussed in Refs. [53] and [54] and study the two-dimensional Hubbard-Holstein model. In contrast to Ref. [159], our approach involves the non-adiabatic regime (i.e., $t/\omega_0 \leq 1$). Furthermore, we employ a controlled analytic treatment of the strong coupling regimes for both the e-ph ($g > 1$) and e-e interactions ($U/t > 1$) and take into account the dynamical quantum phonons. The effective Hamiltonian consists of two major competing interactions—antiferromagnetic interaction between NN spins which favors the formation of singlets and NN repulsion between electrons which encourages CDW formation. Now, Ref. [53] showed that the quarter-filled one-

dimensional Hubbard-Holstein model manifests a correlated singlet phase over a range of U/t values, whereas Ref. [54] demonstrated that this phase occurs at other fillings as well. In this work we concentrate only on the correlated singlet phase in the two-dimensional version of the Hubbard-Holstein model. On representing a singlet by a HCB at its center, the system of singlets on a periodic square lattice transforms into a system of HCBs on a checkerboard lattice. Using quantum Monte Carlo (QMC) simulation involving stochastic-series-expansion (SSE) method, we study the system at various filling fractions. Our results for HCBs, at filling $1/8$, indicates CDW order and unlike its one-dimensional analogue, exhibits supersolidity around filling $1/8$. We explain the mechanism responsible for the formation of the CDW as well as the supersolid phase (on the vacancy side and the interstitial side of the CDW). Furthermore, our study at quarter-filling reveals mutually-exclusive existence of valence bond solid (VBS) and superfluid (SF) phase.

The chapter is organized as follows. In Sec. 4.2, we derive the effective Hamiltonian and discuss the various terms. In Sec. 4.3, we show that the Hamiltonian of singlets on a square lattice transforms into a Hamiltonian of HCBs on a checkerboard lattice. Sec. 4.4 deals with the numerical procedure as well as the order parameters used in our study. Next, the results are discussed in Sec. 4.5 and finally, conclusions are presented in Sec. 4.6.

4.2 Effective Hamiltonian

The first step towards obtaining an effective Hamiltonian is to carry out the Lang-Firsov (LF) transformation, $H_{hh}^{\mathrm{LF}} = e^S H_{hh} e^{-S}$ where $S = -g \sum_{j\sigma} n_{j\sigma}(a_j - a_j^\dagger)$ and get the trans-

formed Hamiltonian to be

$$H_{hh}^{LF} = -t \sum_{j,\delta,\sigma} X_{j+\delta}^\dagger c_{j+\delta\sigma}^\dagger c_{j\sigma} X_j + \omega_0 \sum_j a_j^\dagger a_j + (U - 2g^2\omega_0) \sum_j n_{j\uparrow} n_{j\downarrow} - g^2\omega_0 \sum_j (n_{j\uparrow} + n_{j\downarrow}),$$

(4.2)

with $X_j = e^{g(a_j - a_j^\dagger)}$. In terms of the composite fermionic operator, $d_{j\sigma}^\dagger \equiv c_{j\sigma}^\dagger X_j^\dagger$, the LF transformed Hamiltonian can be expressed as

$$H_{hh}^{LF} = -t \sum_{j,\delta,\sigma} d_{j+\delta\sigma}^\dagger d_{j\sigma} + \omega_0 \sum_j a_j^\dagger a_j + U_{eff} \sum_j n_{j\uparrow}^d n_{j\downarrow}^d - g^2\omega_0 \sum_j (n_{j\uparrow}^d + n_{j\downarrow}^d), \quad (4.3)$$

where $n_{j\sigma}^d = d_{j\sigma}^\dagger d_{j\sigma}$ and $U_{eff} = U - 2g^2\omega_0$. Since, the last term represents a constant polaronic energy, we can drop it without affecting the physics of the system. This leaves us with the realization that Eq. (4.3) essentially represents the Hubbard model for composite fermions where the Hubbard interaction is given by $U_{eff} = U - 2g^2\omega_0$. In the limit of large U_{eff}/t, with the help of a standard canonical transformation, the effective Hamiltonian, upto second order in the small parameter t/U_{eff}, can be expressed as

$$H_{t-J-t_3} = P_s \left[-t \sum_{j,\delta,\sigma} d_{j+\delta\sigma}^\dagger d_{j\sigma} + \omega_0 \sum_j a_j^\dagger a_j + \frac{J}{2} \sum_{j,\delta} \left(\vec{S}_j \cdot \vec{S}_{j+\delta} - \frac{n_j^d n_{j+\delta}^d}{4} \right) \right.$$

$$\left. + t_3 \sum_{j,\delta\neq\delta',\sigma} d_{j\bar\sigma}^\dagger d_{j+\delta\sigma} d_{j+\delta'\sigma}^\dagger d_{j\bar\sigma} - t_3 \sum_{j,\delta\neq\delta',\sigma} d_{j\sigma}^\dagger d_{j+\delta\sigma} d_{j+\delta'\bar\sigma}^\dagger d_{j\bar\sigma} \right] P_s, \quad (4.4)$$

with $n_j^d = n_{j\uparrow}^d + n_{j\downarrow}^d$, $J = \frac{4t^2}{U_{eff}}$ and $t_3 = J/4$. In the above expression $\vec{S}_j$ represents the spin operator for a fermion at site j and the operator P_s projects out double occupancy of any site.

In terms of the original fermionic operator, the effective Hamiltonian can be separated

118

into two terms: (i) an unperturbed electronic Hamiltonian H_0 and (ii) a perturbative term H_1 in terms of the composite fermions. Thus,

$$H_{t-J-t_3} = H_0 + H_1 \,, \tag{4.5}$$

where

$$H_0 = -te^{-g^2} \sum_{j,\delta,\sigma} P_s \left(c^\dagger_{j+\delta\sigma} c_{j\sigma} \right) P_s + \omega_0 \sum_j a^\dagger_j a_j + \frac{J}{2} \sum_{j,\delta} P_s \left(\vec{S}_j \cdot \vec{S}_{j+\delta} - \frac{n_j n_{j+\delta}}{4} \right) P_s$$
$$+ \frac{Je^{-g^2}}{4} \sum_{j,\delta \neq \delta',\sigma} P_s \left(c^\dagger_{j\bar\sigma} c_{j+\delta\sigma} c^\dagger_{j+\delta'\sigma} c_{j\bar\sigma} \right) P_s - \frac{Je^{-g^2}}{4} \sum_{j,\delta \neq \delta',\sigma} P_s \left(c^\dagger_{j\sigma} c_{j+\delta\sigma} c^\dagger_{j+\delta'\bar\sigma} c_{j\bar\sigma} \right) P_s,$$

$$\tag{4.6}$$

and

$$H_1 = -te^{-g^2} \sum_{j,\delta,\sigma} P_s \left[c^\dagger_{j+\delta\sigma} c_{j\sigma} \left(Y^{j\dagger}_+ Y^j_- - 1 \right) \right] P_s \,. \tag{4.7}$$

n the above expression, the electron-phonon interaction is depicted by H_1 only through the term $Y^j_\pm \equiv e^{\pm g(a_{j+\delta} - a_j)}$. One should note that since $J/4 \ll t$, we have ignored the following terms in H_1:

$$\frac{Je^{-g^2}}{4} \sum_{j,\delta \neq \delta',\sigma} P_s \left[c^\dagger_{j\bar\sigma} c_{j+\delta\sigma} c^\dagger_{j+\delta'\sigma} c_{j\bar\sigma} \left(Z^{j\dagger}_+ Z^j_- - 1 \right) \right] P_s$$
$$- \frac{Je^{-g^2}}{4} \sum_{j,\delta \neq \delta',\sigma} P_s \left[c^\dagger_{j\sigma} c_{j+\delta\sigma} c^\dagger_{j+\delta'\bar\sigma} c_{j\bar\sigma} \left(Z^{j\dagger}_+ Z^j_- - 1 \right) \right] P_s \,, \tag{4.8}$$

where $Z^j_\pm \equiv e^{\pm g(a_{j+\delta'} - a_{j+\delta})}$. Performing a second order perturbation theory that is similar

to the one outlined in Ref. [53], the effective Hamiltonian is obtained to be

$$H_{hh}^{\text{eff}} \cong -t_{\text{eff}} h_{t_1} + \frac{J}{2} h_S - V h_{nn} - t_2 h_{\sigma\sigma} - (t_2 + J_3) h_{\sigma\bar{\sigma}} + J_3 h'_{\sigma\bar{\sigma}} , \qquad (4.9)$$

where

$$h_{t_1} = \sum_{j,\delta,\sigma} P_s \left(c_{j+\delta\sigma}^\dagger c_{j\sigma} \right) P_s , \qquad (4.10)$$

$$h_S = \sum_{j,\delta} P_s \left(\vec{S}_j \cdot \vec{S}_{j+\delta} - \frac{n_j n_{j+\delta}}{4} \right) P_s , \qquad (4.11)$$

$$h_{nn} = \sum_{j,\delta,\sigma} \left(1 - n_{j+\delta\bar{\sigma}} \right) \left(1 - n_{j\bar{\sigma}} \right) n_{j\sigma} \left(1 - n_{j+\delta\sigma} \right) , \qquad (4.12)$$

$$h_{\sigma\sigma} = \sum_{j,\delta\neq\delta',\sigma} \left(1 - n_{j+\delta\bar{\sigma}} \right) \left(1 - n_{j\bar{\sigma}} \right) \left(1 - n_{j+\delta'\bar{\sigma}} \right) \times \left[c_{j+\delta\sigma}^\dagger \left(1 - 2n_{j\sigma} \right) c_{j+\delta'\sigma} \right] , \qquad (4.13)$$

$$h_{\sigma\bar{\sigma}} = \sum_{j,\delta\neq\delta',\sigma} \left(1 - n_{j+\delta\bar{\sigma}} \right) \left(1 - n_{j+\delta'\sigma} \right) \times \left[c_{j\sigma}^\dagger c_{j+\delta\sigma} c_{j+\delta'\bar{\sigma}}^\dagger c_{j\bar{\sigma}} \right] , \qquad (4.14)$$

and

$$h'_{\sigma\bar{\sigma}} = \sum_{j,\delta\neq\delta',\sigma} \left(1 - n_{j+\delta\bar{\sigma}} \right) \left(1 - n_{j\sigma} \right) \left(1 - n_{j+\delta'\bar{\sigma}} \right) \times \left[c_{j\bar{\sigma}}^\dagger c_{j+\delta\sigma} c_{j+\delta'\sigma}^\dagger c_{j\bar{\sigma}} \right] . \qquad (4.15)$$

The different coefficients for the various terms present in Eq. (4.9) are defined as follows: $t_{\text{eff}} = t e^{-g^2}$, $J \equiv \frac{4t^2}{U - 2g^2\omega_0}$, $V \simeq t^2/2g^2\omega_0$, $t_2 \simeq t^2 e^{-g^2}/g^2\omega_0$ and $J_3 = J e^{-g^2}/4$. Out of the six terms of the effective Hamiltonian H_{hh}^{eff}, four terms contribute to the kinetic energy of the system. However, due to the presence of e^{-g^2} in the coefficients, the contribution of the kinetic terms is small compared to that from the remaining two interaction terms. The first contribution in the kinetic energy is from the NN hopping term $-t_{\text{eff}} h_{t_1}$ in which the hopping coefficient is given by a reduced hopping integral $t_{\text{eff}} = t e^{-g^2}$. Next, the
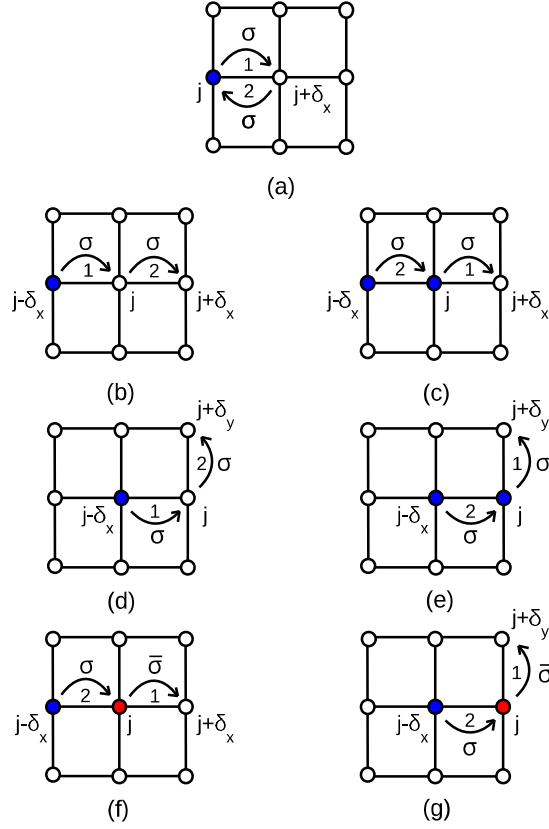
Figure 4.1: Different hopping processes which contribute to second-order perturbation theory: (a) $c_{j\sigma}^\dagger c_{j+\delta_x\sigma} c_{j+\delta_x\sigma}^\dagger c_{j\sigma}$, (b) $c_{j+\delta_x\sigma}^\dagger c_{j\sigma} c_{j\sigma}^\dagger c_{j-\delta_x\sigma}$, (c) $c_{j\sigma}^\dagger c_{j-\delta_x\sigma} c_{j+\delta_x\sigma}^\dagger c_{j\sigma}$, (d) $c_{j+\delta_y\sigma}^\dagger c_{j\sigma} c_{j\sigma}^\dagger c_{j-\delta_x\sigma}$, (e) $c_{j\sigma}^\dagger c_{j-\delta_x\sigma} c_{j+\delta_y\sigma}^\dagger c_{j\sigma}$, (f) $c_{j\sigma}^\dagger c_{j-\delta_x\sigma} c_{j+\delta_x\bar\sigma}^\dagger c_{j\bar\sigma}$, and (g) $c_{j\sigma}^\dagger c_{j-\delta_x\sigma} c_{j+\delta_y\bar\sigma}^\dagger c_{j\bar\sigma}$. Empty circles denote sites without electrons; filled blue and red circles represent sites occupied by electrons with spin σ and spin $\bar\sigma$ respectively.

term $-t_2 h_{\sigma\sigma}$ is represented by the typical processes shown in Figs. 4.1(b), 4.1(c) 4.1(d) and 4.1(e). Figs. 4.1(b) and 4.1(d) depict double hopping of a single particle to next-to-next-nearest-neighbor (NNNN) site and next-nearest-neighbor (NNN) site, respectively; contrastingly, Figs. 4.1(c) and 4.1(e) describe processes where a pair of electrons of spin σ hop sequentially along a straight path and a right-angled path, respectively. The next term $-\left(t_2 + J_3\right) h_{\sigma\bar\sigma}$ is represented by the typical hopping processes in Figs. 4.1(f) and 4.1(g) which are similar to the hopping processes shown in Figs. 4.1(c) and 4.1(e), respectively,

but with the involved pair of electrons now having opposite spins $\sigma\bar{\sigma}$. Lastly, the terms $J_3 h'_{\sigma\bar{\sigma}}$ implies NN spin-pair $\sigma\bar{\sigma}$ hopping similar to that depicted in Figs. 4.1(f) and 4.1(g), respectively, but with the spin-pair $\sigma\bar{\sigma}$ flipping to $\bar{\sigma}\sigma$. Thus, $h'_{\sigma\bar{\sigma}}$ acting on a singlet state results in another singlet state displaced by one NN distance and with a negative sign. Now, the NN spin-spin interaction term $J h_S$ and NN repulsion term $-V h_{nn}$ dominate over the remaining hopping terms in the effective Hamiltonian. As discussed in the Refs. [53] and [54], at larger J values, a phase separated single cluster is formed because the spin-spin interaction dominates over the NN repulsion. As the J/V value is decreased, the system undergoes a first order quantum phase transition to a correlated NN singlet phase where two NN particles pair to form a singlet. This correlated singlet phase persists over a range of J/V values; at even smaller values, a phase with separated spins is realized. It was also shown that the window of J/V, for which the correlated singlet phase exists, is broader for larger g values. Even for the case of the two-dimensional Hubbard-Holstein model, we expect similar results to hold and we present supporting arguments as follows. In the cluster regime, based on Monte Carlo simulation of a two-dimensional Heisenberg antiferromagnet [160], the energy/site $= -0.672J + 2(2V - \frac{J}{4})$. On the other hand, for separated singlets in the correlated singlet phase the energy/site $= -0.375J + \frac{1}{2}(2V - \frac{J}{4})$. Thus the cluster phase prevails when $= -0.672J + 2(2V - \frac{J}{4}) < -0.375J + \frac{1}{2}(2V - \frac{J}{4})$ or equivalently, when $U < 3.792 g^2 \omega_0$. Next, the transition from the correlated-singlet phase to the separated-spin phase occurs when singlets dissociate and is independent of the dimension of the system; this transition occurs when, for the correlated singlet phase, the energy/site $-0.375J + \frac{1}{2}(2V - \frac{J}{4}) \approx 0$, i.e., $U \approx 6 g^2 \omega_0$.

In this work, we concentrate on the region of the parameter space where the correlated singlet phase is manifested.
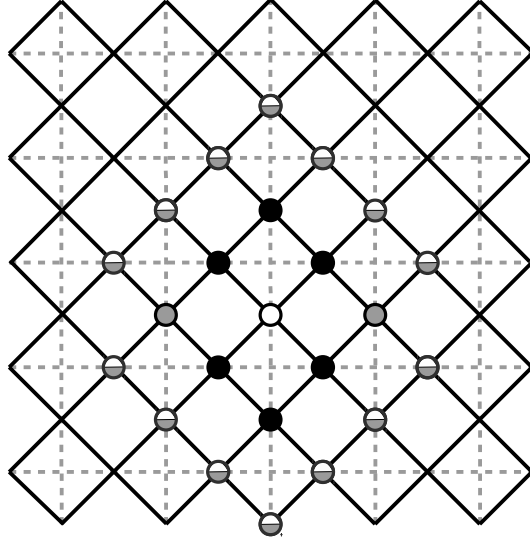
Figure 4.2: Checkerboard lattice constructed by joining the midpoints of the edges of a square lattice (indicated by the dashed lines). The filled black circles denote the six NN of the HCB depicted by the white circle, whereas the filled gray circles stand for next-nearest-neighbor (NNN) sites. The half-filled gray circles are next-to-next-nearest-neighbor (NNNN) sites for which the repulsion is half of the one felt for the filled gray sites.

4.3 $t_1 - V_1 - V_2 - V_3$ **hard-core-boson model on a checkerboard lattice**

In the correlated singlet phase, each NN singlet can be represented as a HCB located at the center of the singlet. Thus, the system of NN singlets on a periodic square lattice transforms into a system of HCBs on a checkerboard lattice; the resulting checkerboard lattice is constructed by joining the midpoints of the edges of the underlying square lattice (see Fig. 4.2). Now, there are two processes by which the singlets can transport in the system. The first process corresponds to NN hopping of spin-pair $\sigma\bar{\sigma}$ and is represented by $h_{\sigma\bar{\sigma}}$ (without spins flipping) and $h'_{\sigma\bar{\sigma}}$ (involving flipping the spins). The second process is a consequence

of the presence of the NN hopping h_{t_1} in H_{hh}^{eff}; this is a second order process which involves breaking of a bound singlet state (with binding energy $E_B = -J + 2V = -J + t^2/g^2\omega_0$) and hopping of the constituent spins. Now, the spins can hop in two different ways: (a) each spin hops to its NN site sequentially [in a manner given by Figs. 4.1(f) and 4.1(g)] and generating the corresponding term $-t_b h_{\sigma\bar\sigma}$ with $t_b \equiv t^2 e^{-2g^2}/|E_B|$; and (b) any one of the two constituent spins hops to its NN site (along x or y directions) and comes back [yielding the corresponding term $-t_b h_{nn}$]. All these processes effectively describe the NN hopping (t_1) of the HCBs in the checkerboard lattice. For example, in Fig. 4.2, a HCB residing at the site denoted by a white circle can hop to its six NN sites represented by the filled black circles. Now, no pair of singlets can share a common site. Therefore, the NN repulsion (V_1) between two HCBs in the checkerboard lattice is essentially infinity. Next, the NN repulsion between two electrons in the square lattice (coming from the terms Jh_S and $-Vh_{nn}$ in the expression of H_{hh}^{eff}) gives rise to the NNN repulsion and the NNNN repulsion between two HCBs in the checkerboard lattice. To understand this, in Fig. 4.2, consider two HCBs residing at the white and any one of the two filled gray sites. Corresponding to this situation, in the original square lattice there will be two pairs of electrons which are NN, thus increasing the energy of the system by an amount $2(2V - J/4)$. In other words, repulsion $V_2 = 2(2V - J/4)$ is felt between the HCBs residing at the white circle and its NNN sites denoted by filled gray circles. On the other hand, the repulsion felt between the white circle and its fourteen NNNN sites, depicted by the half-gray circles, is $V_3 = V_2/2$.

Finally the effective Hamiltonian governing the HCBs in the checkerboard lattice is given by

$$H_b = -t_1 \sum_{\langle i,j \rangle} \left(b_i^\dagger b_j + \text{H.c.} \right) + V_1 \sum_{\langle i,j \rangle} n_i n_j + V_2 \sum_{\langle\langle i,j \rangle\rangle} n_i n_j + V_3 \sum_{\langle\langle\langle i,j \rangle\rangle\rangle} n_i n_j \,, \quad (4.16)$$

where b_j $(b_j^\dagger)$ denotes the destruction (creation) operator for a HCB at site j with $n_j = b_j^\dagger b_j$ being the number operator. Here, the symbol $\langle i, j \rangle$ stands for a NN pair of sites, whereas $\langle\langle i, j \rangle\rangle$ and $\langle\langle\langle i, j \rangle\rangle\rangle$ represent NNN pair and NNNN pair, respectively. The coefficients of the different terms of H_b are given as follows: $t_1 = (t_2 + 2J_3 + t_b)$, $V_1 = \infty$, $V_2 = 2(2V - J/4)$ and $V_3 = V_2/2$.

4.4 Numerical Calculations

To study the system of HCBs in the checkerboard lattice depicted by Fig. 4.2, we employ quantum Monte Carlo (QMC) simulation involving stochastic-series-expansion (SSE) technique [44, 112] with directed loop updates [79, 80]. To achieve the above end, first we rewrite the Hamiltonian H_b in terms of spin-1/2 operators by identifying $b_j^\dagger = S_j^+$, $b_j = S_j^-$ and $n_j = S_j^z + \frac{1}{2}$. We recast the effective Hamiltonian H_b for HCBs as an extended XXZ spin-1/2 Hamiltonian, which, in units of $2t_1$, is given by

$$H = \sum_{\langle i,j \rangle} \left[-\frac{1}{2} \left(S_i^+ S_j^- + \text{H.c.} \right) + \Delta_1 S_i^z S_j^z \right] + \sum_{\langle\langle i,j \rangle\rangle} \Delta_2 S_i^z S_j^z + \sum_{\langle\langle\langle i,j \rangle\rangle\rangle} \Delta_3 S_i^z S_j^z - h \sum_i S_i^z ,$$

(4.17)

where $\Delta_1 = V_1/2t_1$, $\Delta_2 = V_2/2t_1$, and $\Delta_3 = V_3/2t_1$. Furthermore, we have introduced the variable h (a dimensionless external magnetic field); upon tuning h, we can access different magnetizations (or filling-fractions) of the system.

Due to the presence of a hopping term in the Hamiltonian, superfluidity is expected; on the other hand, large repulsions indicate the possibility of a CDW. Hence, to study the competition or coexistence of these two long-range orders, we choose two order parameters: structure factor $S(\vec{Q})$ (for diagonal long-range order) and superfluid density ρ_s (for

off-diagonal long-range order). The expression for the structure factor per site, used in this chapter, is given as

$$S(\vec{Q}) = \frac{4}{N_s^2} \sum_{i,j} e^{i\vec{Q}\cdot(\vec{R}_i - \vec{R}_j)} \langle S_i^z S_j^z \rangle \tag{4.18}$$

where $\langle \cdots \rangle$ represents ensemble average and N_s is the total number of sites. We study $S(\vec{Q})$ for all possible values of $\vec{Q}$ and identify the ones that produce peaks in the structure factor.

As discussed in Sec. 3.3, the superfluid density, in terms of the fluctuation of winding numbers, is expressed as

$$\rho_s = \frac{1}{2\beta} \langle W_x^2 + W_y^2 \rangle \tag{4.19}$$

where W_x and W_y denote the winding numbers along x and y directions, respectively; β is the inverse temperature. Furthermore, W_x can be calculated from the total number of operators transporting spin in the positive and negative x directions (i.e., N_x^+ and N_x^-) using the expression $W_x = \frac{1}{L_x}(N_x^+ - N_x^-)$, where L_x is the linear dimension of the lattice along the x direction.

Now, due to particle-hole symmetry, Eq. (4.16) corresponds to HCB particles (holes) for particle density between 0 and 1/2 (1/2 and 1). The NN repulsion between two HCB particles or holes [i.e., V_1 in Eq. (4.16)] is infinity. In the filling-fraction range 1/4 and 1/2 (1/2 and 3/4), the HCB particles (holes) cannot be arranged so that no two HCB particles (holes) are on neighboring sites. In other words, for fillings of HCB particles (holes) between 1/4 and 1/2 (1/2 and 3/4) on a checkerboard lattice, which corresponds to fillings of electrons between 1/2 and 1 (1 and 3/2) on a square lattice, our theory of

h	70.0	75.0	85.25	92.0
τ_{int}	1154	56182	420361	3747

Table 4.1: Autocorrelation times calculated for $\Delta_1 = 16$, $\Delta_2 = 10$ and $\Delta_3 = 5$ with $\epsilon_1 = 8$, $\epsilon_2 = 10/4$ and $\epsilon_3 = \epsilon_2/2$; the magnetic fields are chosen close to the transitions as well as far from the transitions (see Fig. 4.10 for details).

correlated singlet phase of electrons does not hold. Therefore, on a checkerboard lattice of HCBs, we restrict our interest to particle fillings in the range 0 and 1/4 (or 3/4 and 1). In this chapter, we vary the magnetization from 1/4 to 1/2 which means decreasing the hole density from 1/4 to 0.

Next, in the presence of large anisotropy (i.e., large values of Δ_1, Δ_2 and Δ_3) SSE suffers from significant slowing down, as we have already seen in Chapter 3. Therefore, due to numerical restrictions we cannot use the actual values of the longitudinal couplings; instead, we use large enough cutoff values so that the physics remains unaltered. These cutoff values must be chosen keeping Δ_1 sufficiently larger than the other Δ_i's so that the HCBs always avoid NN occupation. On the other hand, Δ_2 and Δ_3 must be large compared to t_1, but certainly smaller than Δ_1. We will discuss the cutoff values for the longitudinal couplings in the next section.

As discussed in Ref. [113], simulating at low enough temperatures such that $\beta \sim L$ with L being the linear dimension of the $L \times L$ square lattice, we can capture the ground-state properties of a system using SSE. Since the values of the measured observables were the same (within the error bars of our calculations) for both $\beta = 3L/2$ and $\beta = 2L$, we report the results for $\beta = 3L/2$ in our simulations. From the discussion in Sec. 3.3, one can recall that, in SSE, a parameter ϵ_i is introduced to make the matrix elements positive. This parameter is usually very small. However, in cases with large anisotropy, value of ϵ_i can affect the autocorrelation times. Therefore, similar to Chapter 3, we need to use larger

values of ϵ_i to take care of the autocorrelation times. To make sure that the bin size is always much larger than the autocorrelation times, we calculate the autocorrelation time (τ_{int}) given by the following formula

$$\tau_{\mathrm{int}}[m] = \frac{1}{2} + \sum_{t=1}^{\infty} A_m(t) \tag{4.20}$$

where

$$A_m(t) = \frac{\langle m(i+t)m(i) \rangle - \langle m(i) \rangle^2}{\langle m(i)^2 \rangle - \langle m(i) \rangle^2} \tag{4.21}$$

with i and t representing the Monte Carlo steps and $\langle \cdots \rangle$ the average over the time i. Based on the autocorrelation times obtained, for Δ_1 we use $\epsilon_1 = \Delta_1/2$; whereas $\epsilon_2 = \Delta_2/4$ ($\epsilon_3 = \Delta_3/4$) is good enough to restrict the autocorrelation time within affordable limits. An estimate of the autocorrelation time for $\Delta_1 = 16$, $\Delta_2 = 10$ and $\Delta_3 = 5$ is given in Table 4.1. The magnetic fields are chosen close to the transitions, where the autocorrelation time is expected to be larger, as well as away from them. The bin size used for all numerical calculations is $16,00,000$ to make sure that the autocorrelation time is well within the bin size for all magnetic fields.

4.5 Results and discussions

For numerical simulations, we can consider two types of lattices. A checkerboard lattice, constructed from an underlying $L \times L$ square lattice (see Fig. 4.2), contains $2 \times L \times L$ number of sites. Alternately, an $L \times L$ checkerboard lattice, as shown in Fig. 4.3, can be obtained via a $45°$ rotation of the lattice of Fig. 4.2. In the thermodynamic limit, either of the choices is supposed to yield the correct results; we have checked that even for a
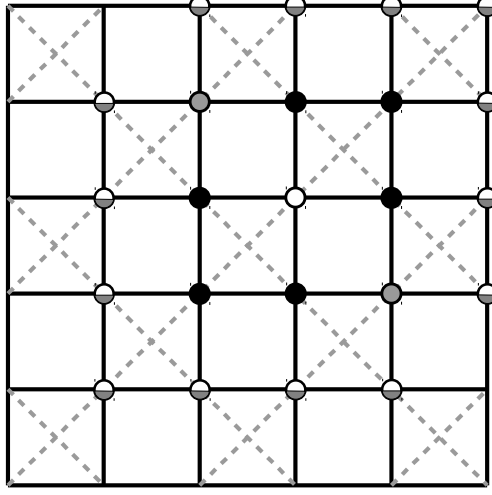
Figure 4.3: Checkerboard lattice of second type which is a part of the original checkerboard lattice (in Fig. 4.2) and rotated by $45°$ angle. The filled black circles denote the six NN of the HCB depicted by the white circle, whereas the filled gray circles stand for NNN sites. The half-filled gray circles are NNNN sites for which the repulsion is half of the one felt for the filled gray sites.

small system size with $L = 8$, both the lattices produce the same results. Thus, at large anisotropies, simulation time can be lowered by considering a $L \times L$ checkerboard lattice. In this chapter, we present the results for HCBs on a 16×16 checkerboard lattice of the second type, as depicted in Fig. 4.3.

To determine the various phases of the two dimensional Hubbard-Holstein model, we first set the cutoff values of the anisotropies to be $\Delta_1 = 16$, $\Delta_2 = 10$ and $\Delta_3 = 5$; we calculate the order parameters for magnetization m values ranging from 0.25 to 0.5. The requirement that $\Delta_1 \to \infty$ is implemented via a suitable choice of large but finite value of Δ_1 so as to avoid computational problems. Fig. 4.4 shows the variation of the structure factor $S(\vec{Q})$ and superfluid density ρ_s as the magnetization of the system is varied from 0.25 to 0.5; this corresponds to the variation of filling fraction of HCBs from 3/4 to 1.
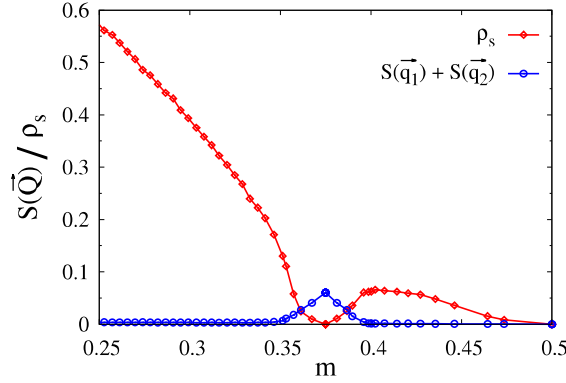
Figure 4.4: Plots of structure factor $S(\vec{Q})$ and superfluid density ρ_s vs magnetization m for HCBs on a 16×16 checkerboard lattice with $\Delta_1 = 16$, $\Delta_2 = 10$ and $\Delta_3 = 5$. The figure demonstrates the existence of supersolidity in the vicinity of $m = 0.375$. The results are obtained by averaging over simulations for three different random number seeds.

Due to the particle-hole symmetry of the Hamiltonian, the physics at filling fraction $3/4$ is the same as the one revealed at filling fraction $1/4$. Hence, in the text, we use them interchangeably at our convenience. From Fig. 4.4, at filling $7/8$ (i.e., $m = 3/8$), we see that the system manifests a CDW state, whereas the superfluid (SF) order ceases to exist. At filling fraction $1/8$, the HCBs arrange themselves so that no repulsion is felt; the resulting state is an insulating CDW, characterized by a peak in the structure factor at wavevectors $\vec{q_1} = (\pi/4, 3\pi/4)$ [as shown in Fig. 4.5(a)] or $\vec{q_2} = (\pi/4, 5\pi/4)$ [as depicted in Fig. 4.5(b)]. We call this CDW state a diagonal striped solid (dsS). One should note that, unlike the well-known checkerboard solid identified by the peak in the structure factor $S(\pi, \pi)$ (see Figs. 3.4 and 3.5 of Chapter 3), a single wavevector is inadequate to characterize the two equally probable CDW states at filling $1/8$. Whenever the system manifests a dsS equivalent to that in Fig. 4.5(a), $S(\vec{q_1})$ acquires a non-zero value while $S(\vec{q_2})$ concomitatntly vanishes. On the other hand, for a dsS corresponding to Fig. 4.5(b), the situation is reversed with $S(\vec{q_2})$ taking a non-zero value whereas $S(\vec{q_1})$ now vanishing. Therefore, to identify the insulating dsS at filling $1/8$, we should plot the sum $[S(\vec{q_1}) + S(\vec{q_2})]$ of these two structure factors.

130
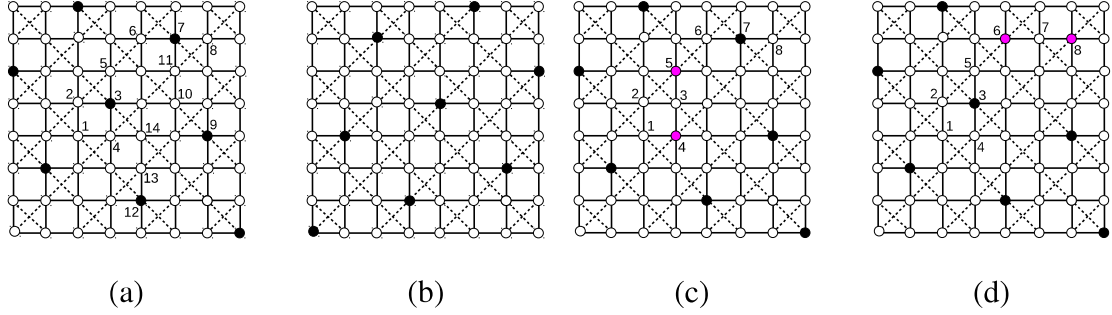
Figure 4.5: Two different types of CDWs: (a) diagonal striped solid (dsS) indicated by a peak in the structure factor at wavevector $\vec{q}_1 = (\pi/4, 3\pi/4)$; (b) dsS characterized by ordering wavevector $\vec{q}_2 = (\pi/4, 5\pi/4)$. (c) A minimum energy configuration obtained after rearrangement when an extra HCB is added at site 1 in Fig. 4(a). The rearranged particles are indicated in magenta. (d) A resulting configuration when the pair of HCBs at sites 4 and 5 in Fig. 4(c) flows through the system.

Now, when we add one extra particle to the system at filling $1/8$, one would normally think of two different possible scenarios. The extra particle can either occupy any empty site along the half-filled stripes or an empty one between any two stripes. First, let us assume that the particle occupies site 1 (i.e., a site along one of the half-filled stripes) in Fig. 4.5(a). The repulsion felt by this particle is $2V_2 + 2V_3 = 3V_2$. Instead of this configuration, if the particle at site 3 is moved to site 5 and the extra particle occupies site 4, the resulting configuration [see Fig. 4.5(c)] is energetically favored because the repulsion felt in this case is $5V_3 = 2.5V_2$. Now, by the following third-order process superflow of particles can take place in the system given by Fig. 4.5(c). First, the particle at site 7 can hop to site 8 which increases the energy of the system by V_3. Next, the particle at site 5 can hop to site 6 with the energy of the system being the same as that after the first process. Finally, the particle at site 4 can hop to site 3 resulting in the configuration depicted in Fig. 4.5(d). The energy of this final configuration is the same as that of the starting configuration shown in 4.5(c). The energy of this third-order perturbation process is thus proportional to $t_1{}^3/V_3^2$. There may also be other processes by which the system manifests supersolidity when the
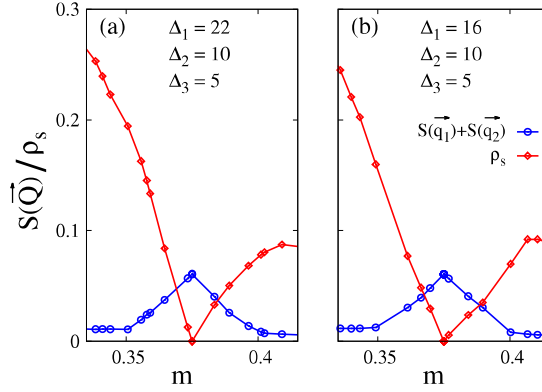
Figure 4.6: Comparison of the behavior of the order parameters, structure factor $S(\vec{Q})$ and superfluid density ρ_s, as functions of magnetization m on an 8×8 checkerboard lattice for two different sets of anisotropy values: (a) $\Delta_1 = 22$, $\Delta_2 = 10$, $\Delta_3 = 5$ and (b) $\Delta_1 = 16$, $\Delta_2 = 10$, $\Delta_3 = 5$. The figures demonstrate that the essential coexistence features are not altered much when Δ_1 is increased beyond 16.

dsS is doped with particles. Nevertheless, this particular process is one of the possible mechanisms which gives rise to supersolidity on the interstitial side of the CDW at filling 1/8.

Next, in the second possible scenario (where the extra particle occupies an empty site between any two half-filled stripes), let us assume that the extra particle occupies site 2 in Fig. 4.5(a). Then, the repulsion felt by this particle is $V_1 + 2V_3 = V_1 + V_2$. It is important to note that in this case there is no way to avoid NN occupation of HCBs; this is not allowed because two singlets cannot share an electron. Although the cutoff values of the repulsions used in our simulation makes the first scenario energetically favorable, the energy difference between these two situations is marginal. Moreover, in the second case the extra particle can hop to any of its unoccupied NN sites leading to lower energy and eventually to supersolidity. Therefore, unless the energy difference between these two scenarios is reasonable we can not rule out the possibility of the second one. As mentioned earlier, numerical restrictions do not allow us to use anisotropies larger than the cutoff

132
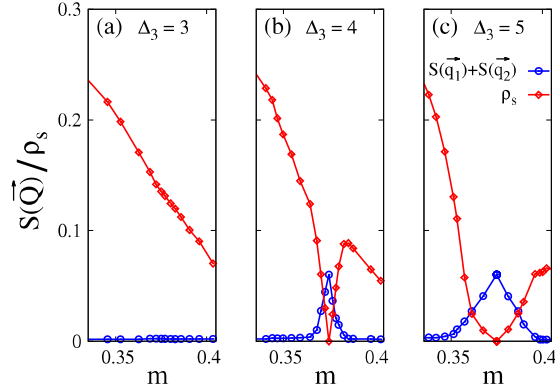
Figure 4.7: Variation of structure factor $S(\vec{Q})$ and superfluid density ρ_s as functions of magnetization m in the vicinity of filling fraction $1/8$ at three different values of Δ_3 (with $\Delta_2 = 2\Delta_3$) and for a fixed $\Delta_1 = 16$: (a) $\Delta_3 = 3$; (b) $\Delta_3 = 4$; and (c) $\Delta_3 = 5$. The figures depict evolution of supersolidity around $m = 0.375$.

values used in our simulations on 16×16 lattices. Therefore, to avoid prohibitively large simulation times, we considered a smaller 8×8 system and calculated the order parameters for two different sets of parameters: $\Delta_1 = 22$, $\Delta_2 = 10$, and $\Delta_3 = 5$; $\Delta_1 = 16$, $\Delta_2 = 10$, and $\Delta_3 = 5$. Fig. 4.6 compares the plots of the structure factor $S(\vec{Q})$ and superfluid density ρ_s as a function of magnetization m for these two different sets of anisotropies. For the first set of parameters (i.e., $\Delta_1 = 22$, $\Delta_2 = 10$, and $\Delta_3 = 5$), the energy of the system with an additional particle at site 2 in Fig. 4.5(a) (with $V_1 + V_2 = 64t_1$) is much larger than the energy corresponding to the situation in Fig. 4.5(c) (with $2.5V_2 = 50t_1$). Hence, we can definitely rule out the possibility of the second scenario involving the extra particle occupying any empty site between any two half-filled stripes. Since Fig. 4.6 demonstrates that both the parameter sets yield similar results, we can capture the essential physics of the two-dimensional Hubbard-Holstein model by using $\Delta_1 = 16$, $\Delta_2 = 10$ and $\Delta_3 = 5$ as the cutoff values of the anisotropies in the simulations. It should be noted that, in Fig. 4.6, the non-zero value of the structure factor $S(\vec{Q})$, below $m \approx 0.35$ and beyond $m \approx 0.4$, is just an artifact of the small system size.

133
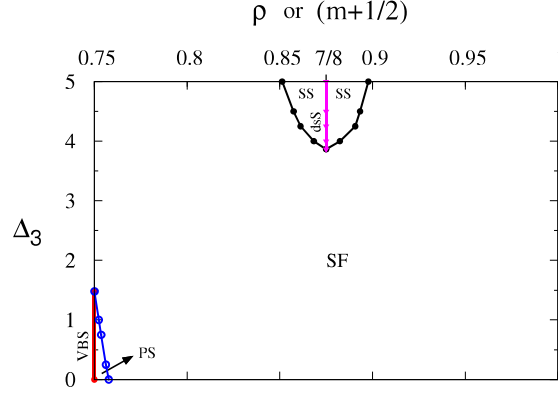
Figure 4.8: Ground-state phase diagram in terms of filling fraction ρ (or magnetization m) for HCBs on a 16×16 checkerboard lattice. Here dsS represents diagonal striped solid, SS stands for the supersolid phase corresponding to dsS, VBS denotes valence-bond solid and PS represents the phase-separated region.

As regards the vacancy side of the half-filled diagonal striped phase, the mechanism responsible for supersolidity can be explained as follows. Let us assume that we remove two HCBs from sites 3 and 7 in the configuration depicted in Fig. 4.5(a). Then, the HCB at site 9 can hop to site 10 without altering the potential energy of the system; next, this HCB at site 10 can hop to site 7 by hopping via site 11 and again the overall potential energy of the system remains unaltered at the end of each hopping process. Similarly, again through a three-step hopping process, without any additional potential energy cost, the particle at site 12 can hop to site 3 by sequentially hopping through sites 13 and 14. Effectively, the pair of holes at sites 3 and 7, moves from one stripe to another one (where they occupy sites 12 and 9), and thereby the coexistence of superfluidity and CDW is manifested.

Next, we perform a general study of the supersolid phase as a function of NNNN anisotropy Δ_3, at a fixed value of $\Delta_1 = 16$. We vary Δ_3 (with $\Delta_2 = 2\Delta_3$) and calculate the order parameters for magnetization values ranging from 0.25 to 0.5. Fig. 4.7 displays the variation of the structure factor $S(\vec{Q})$ and the superfluid density ρ_s as the magnetization of the system is varied in the vicinity of filling fraction 1/8 for three different values of Δ_3.

134
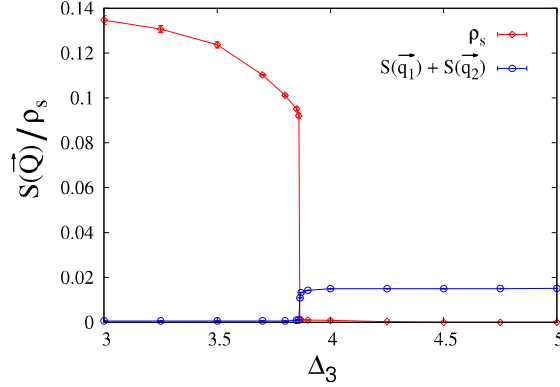
Figure 4.9: Plots of the order parameters, structure factor $S(\vec{Q})$ and superfluid density ρ_s, as functions of the NNNN anisotropy Δ_3 at magnetization $m = 0.375$ (corresponding to 7/8 filling), $\Delta_2 = 2\Delta_3$ and $\Delta_1 = 16$. First order transition is depicted through jumps in both order parameters at $\Delta_3 \approx 3.865$.

For $\Delta_3 = 3$ there is no signature of any CDW at the filling $1/8$, instead only superfluidity exists [as demonstrated in Fig. 4.7(a)]. Fig. 4.7(b) shows that, as we increase the Δ_3 value to 4.0, a diagonal striped solid (dsS) appears at HCB density $\rho = 1/8$ and a supersolid (SS) region, of small width, grows on both sides of the CDW. As the NNNN anisotropy is increased further to $\Delta_3 = 5$, the width of the supersolid region increases further.

The ground-state phase diagram is displayed in Fig. 4.8 for HCBs on a 16×16 checkerboard lattice. At $\rho = 1/8$, the system manifests the existence of a dsS when $\Delta_3 \gtrsim 3.865$. On both sides of this CDW we have a supersolid region (SS), i.e., a homogeneous coexistence of half-filled diagonal striped solid and superfluid; further away from $\rho = 1/8$ and beyond the supersolid region, a superfluid (SF) region exists. For $\Delta_3 \gtrsim 3.865$, as the value of NNNN anisotropy is increased, the width of the SS region increases.

In our simulations, since we can not fix the magnetization or density of the system, we tune the magnetic field h to access various magnetization values. Usually, for a fixed value of magnetic field, the resulting magnetization fluctuates during the simulation. Therefore, in the phase diagram we can not usually study the nature of the phase transition by varying

135
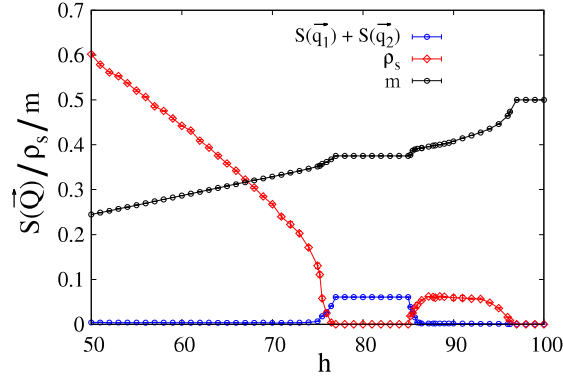
Figure 4.10: Variation of the order parameters (magnetization m, structure factor $S(\vec{Q})$, and superfluid density ρ_s) in terms of the magnetic field h for the set of anisotropy values $\Delta_1 = 16$, $\Delta_2 = 10$, and $\Delta_3 = 5$. Plots depict continuous SF-SS and SS-dsS transitions.

the Δ_3 value at a fixed magnetization (or density). However, in the CDW state, we always have a plateau in the magnetization curve (where the magnetization of the system does not change) when plotted as a function of the magnetic field; thus, by choosing a magnetic field in the plateau, we can ensure a constant magnetization of the system for different values of Δ_3.

For the filling $7/8$ (corresponding to $m = 0.375$), as we increase the Δ_3 value from 3 to 5, Fig. 4.9 shows that the structure factor $S(\pi/4, 3\pi/4) + S(\pi/4, 5\pi/4)$ jumps dramatically from 0 to almost its maximum value at $\Delta_3 \approx 3.865$; concomitantly, the superfluid density ρ_s drops to zero value. In the phase diagram, this signifies a first-order transition from a superfluid to CDW state as we move along the Δ_3 axis at $m = 0.375$. It is worth mentioning here that this transition, from a $U(1)$ symmetry broken SF phase to a translational symmetry broken CDW phase, is consistent with Landau's picture of phase transition. An important point to note is that the magnetization can be fixed exactly at 0.375 only after the transition to the CDW state; before the transition, i.e., in the superfluid region, the magnetization can be estimated as $m = 0.375 \pm 0.0001$.
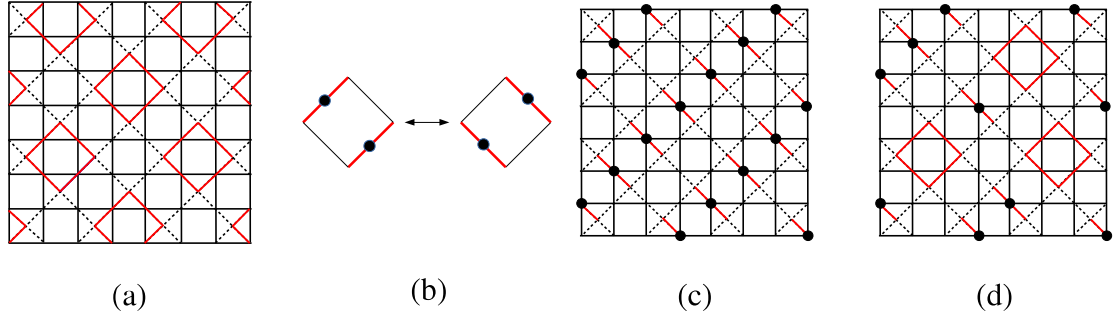
Figure 4.11: Different types of valence bond solids: (a) The ideal plaquette state on the checkerboard lattice where the red diamonds indicate resonance via the ring-exchange process depicted in Fig. 11(b); (c) the ideal columnar state with the black circles representing the HCBs; and (d) a mixed columnar-plaquette state.

Next, excluding the special point ($m = 0.375$, $\Delta_3 \approx 3.865$), we study the nature of the transitions along the m-axis of the phase diagram. Now, Fig. 4.7 indicates that, at a fixed value of Δ_3, the order parameters change continuously as a function of the magnetization m, thereby depicting continuous phase transitions between various phases. A more reliable procedure, for detecting the nature of the phase transitions along the magnetization axis of the phase diagram, is to study the behavior of the order parameters magnetization, structure factor and superfluid density as a function of the magnetic field h. In Fig. 4.10, we demonstrate that the order parameters change continuously as the magnetic field h is varied; this rules out the possibility of a first-order phase transition. Therefore, we conclude that all superfluid-supersolid and supersolid-solid transitions, encountered while moving along the m-axis of the phase diagram, are of continuous nature. Here, it is important to note that, whenever there is a flat region in the magnetization curve, the superfluid density vanishes. Usually, a magnetization plateau indicates the presence of a gapped phase in the system [161]. In Fig. 4.10, the first plateau in the magnetization curve signifies the existence of the insulating CDW state dsS; consequently, the superfluid density drops down to zero. On the other hand, the second flat portion in the magnetization curve corresponds

137
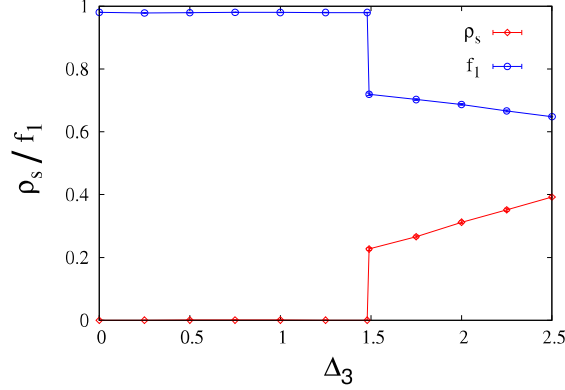
Figure 4.12: Plots of superfluid density ρ_s and the fraction f_1 (representing the relative number of singly occupied non-void plaquettes) in terms of the NNNN anisotropy Δ_3 at magnetization $m = 0.25$ which corresponds to $1/4$ filling of HCBs in a 16×16 checkerboard lattice. The NN anisotropy is fixed at $\Delta_1 = 16$; NNN anisotropy $\Delta_2 = 2\Delta_3$. The figure depicts VBS-SF first-order transition at $\Delta_3 \approx 1.48$.

to a fully-filled system (or equivalently an empty lattice) which is not a Mott insulator. In both the cases, it is not possible for the particles to move, thus producing a zero superfluid density.

We now concentrate on the filling fraction $1/4$ (corresponding to $m = 0.25$) in the phase diagram depicted in Fig. 4.8. The quarter-filled checkerboard lattice has been studied by various authors using different types of Hamiltonians. Sen *et al.* [162] and Wessel [163] considered a Hamiltonian involving NN repulsion between HCBs but omitting the hopping along the diagonals of the non-void plaquettes . In Ref. [116], Wessel studied the quarter-filled checkerboard lattice using a Hamiltonian consisting of NN hopping and NN repulsion. The study showed that beyond some particular repulsion value, the system goes through a quantum phase transition from a superfluid to an insulating valence bond solid (VBS). The VBS can be the ideal plaquette type [shown in Fig. 4.11(a)], the ideal columnar type [depicted in Fig. 4.11(c)], or a mixed columnar-plaquette phase [such as in Fig. 4.11(d)]. To characterize these VBS states, besides employing superfluid density ρ_s,
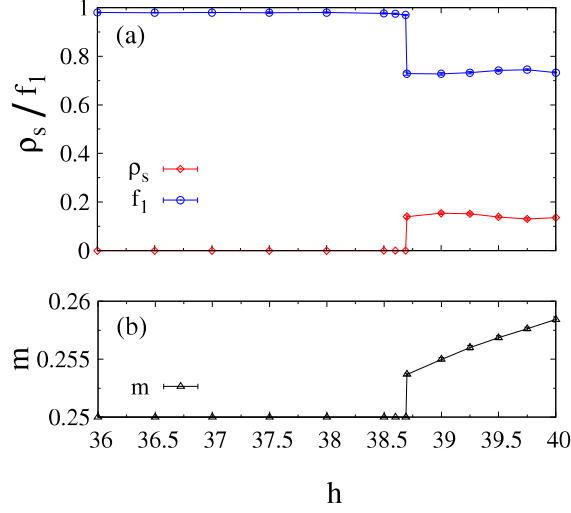
Figure 4.13: Plots of (a) superfluid density ρ_s and fraction f_1 (representing the relative number of singly occupied non-void plaquettes) and (b) magnetization m vs magnetic field h at a fixed NNNN anisotropy $\Delta_3 = 0.75$ on a 16×16 checkerboard lattice. The NN anisotropy is again fixed at $\Delta_1 = 16$, while the NNN anisotropy $\Delta_2 = 2\Delta_3$. The sharp jump in the magnetization curve indicates the existence of a phase-separated (PS) region involving superfluid and VBS (identified by $f_1 \approx 1$). Furthermore, the plateau corresponds to a Mott insulating region.

different order parameters were used by various authors. A common feature among all the VBS states is that each non-void plaquette is occupied by a single HCB. Therefore, along with the superfluid density, we calculate a fraction f_1 which denotes the relative number of non-void plaquettes that are occupied by a single HCB. For the VBS phases this fraction f_1 will have a peak value 1, whereas for any other phase it will assume a smaller non-zero value.

Fig. 4.12 depicts the variation of the superfluid density ρ_s and the fraction f_1 on a 16×16 checkerboard lattice as the NNNN anisotropy Δ_3 is varied from 0 to 2.5 (with $\Delta_2 = 2\Delta_3$ and $\Delta_1 = 16$). For lower values of Δ_3, at one-fourth filling, the system manifests a VBS phase demonstrated by the close-to-unity value of the fraction f_1 and the zero value of the superfluid density ρ_s. As we increase the value of Δ_3, a first-order

phase transition, from VBS to superfluid, is realized beyond $\Delta_3 = 1.48$; the transition is indicated by a jump in the superfluid density ρ_s and an accompanying sudden drop in the fraction f_1 from its maximum value 1 to some smaller non-zero value. In the phase diagram depicted in Fig. 4.8, this signifies a first-order phase transition, along the Δ_3 axis and at $\Delta_3 = 1.48$, when the magnetization remains fixed at $m = 0.25$. Interestingly, while tuning Δ_3, the magnetization remains fixed at 0.25 only in the insulating VBS phase; whereas, after the transition to the superfluid region, the magnetization fluctuates and is estimated as $m = 0.25 \pm 0.000051$). On the other hand, as magnetization is changed from $m = 0.25$ while keeping Δ_3 fixed, we can identify a phase-separated (PS) region where a jump in m as well as in f_1 and ρ_s occurs. In Fig. 4.13, the superfluid density ρ_s, the fraction f_1, and the magnetization m of the system is shown as a function of the applied magnetic field h at a fixed NNNN anisotropy $\Delta_3 = 0.75$. The sharp jump in the magnetization clearly manifests the existence of a PS region in the vicinity of the VBS. The PS window in the phase diagram becomes narrower as Δ_3 is increased from zero and vanishes at $\Delta_3 \approx 1.48$.

4.6 Conclusions

In the present work, we concerned ourselves with understanding the competition and/or cooperation of various orders within the correlated singlet phases in the two-dimensional Hubbard-Holstein model. Strictly speaking, correlated-singlet phase requires singlets that are separated which is only possible at fillings $\leq 1/4$ in the Hubbard-Holstein model (i.e., fillings $\leq 1/8$ of HCBs on a checkerboard lattice). Extending the results of Refs. [53] and [54], we arrived at the $t_1 - V_1 - V_2 - V_3$ Hamiltonian for HCBs on a checkerboard lattice with the NN repulsion V_1 being infinity. We showed that the essential physics of the system can be captured even when cutoff values of the repulsions are used. Unlike the one-

dimensional Hubbard-Holstein model, the two-dimensional version revealed the existence of a supersolid region. Around filling fraction $1/8$, supersolidity is realized; whereas at filling $1/8$, only CDW order results. This result demonstrates how the dimensionality plays an important role in stabilizing the supersolid phase. We also provide an intuitive explanation for the mechanism behind the formation of CDW as well as the occurrence of supersolidity on the interstitial side as well as on the vacancy side of the CDW.

Next, we performed a general study of the $t_1 - V_1 - V_2 - V_3$ model; by varying the NNNN repulsion V_3, we derived the complete phase diagram of the system in terms of the filling fraction (or magnetization) of the system. At filling fraction $1/8$, the system reveals the existence of a half-filled diagonal striped solid. Contrastingly, a quarter-filled system manifests the valence bond solid consistent with the literature [116]. We also show that, in the phase diagram, first-order transitions are realized while going from superfluid to dsS at filling fraction $1/8$ and from VBS to superfluid phase at filling $1/4$. On the other hand, the superfluid-supersolid or the supersolid-solid transition at fixed NNNN repulsions, when we vary the magnetization of the system around filling $1/8$, turned out to be of continuous nature. Lastly, by varying the magnetization of the system around quarter filling, a PS region is identified next to the VBS phase.

A unique feature of our model, compared to many other models, is that the checkerboard lattice naturally emerges out of the square lattice governed by the two-dimensional Hubbard-Holstein Hamiltonian in the parameter regime where correlated singlets are produced. Furthermore, unlike a number of other checkerboard models studied in the literature, the parameter values used in our model can be either obtained from first-principle calculations or determined from experiments.

Lastly, it should be emphasized that the model that we consider (i.e., the Hubbard-Holstein model) involves a combination of electron-electron and electron-phonon interac-

tions in their simplest forms. In a restricted parameter regime, this simple model is shown to manifest lattice supersolidity. Since real materials exhibiting lattice supersolidity generally involve more complexities, further investigations are needed to figure out the relevance of our model for such systems. Additionally, with the rapid advancements in artificially engineered systems, we hope that our model can be experimentally realized, thus advancing the overall understanding of different lattice-supersolid phases.

CHAPTER 5

SUMMARY

In this thesis, we had started off with three different systems having either strong e-ph or strong HCB-ph interactions and arrived at three different models of HCBs. Our primary interest was the study of two long-range orders, namely, CDW and superfluidity. To investigate the different phases arising out of the competition or coexistence of these two orders and explain their origin based on the interactions present in the system, constitute the main goals of this thesis.

Since we are dealing with strong e-ph or HCB-ph couplings, the usual Migdal-type perturbative treatment was not applicable. To derive the effective Hamiltonian, we adopted a non-perturbative approach which involves the well-known Lang-Firsov transformation of the starting Hamiltonian. This transformation, just like a duality transformation, maps the strong coupling problem to a weak coupling one, in which the small parameter is simply inversed. While carrying out this transformation, the generator had to be carefully modified such that the nature of the distortions present in the system was captured by it. By virtue of this transformation, we could split the transformed Hamiltonian into an unperturbed part

143

(H_0) and a perturbative term (H_1). It is important to note that, in the two-dimensional Hubbard-Holstein model, we had two strong-coupling limits; strong e-ph interaction, as well as strong e-e interaction. Therefore, to arrive at the stage where we could split the Hamiltonian into H_0 and H_1, we had to further apply a standard canonical transformation on the Lang-Firsov transformed Hamiltonian, in the large-Hubbard-interaction limit. Once we have H_0 and H_1, we perform a non-trivial perturbation theory up to second order in the basis of the unperturbed eigenstates, as described in Sec. 1.6.

In Chapter 2, the one-dimensional $t_2 - V$ model of HCBs involving NNN hopping and NN repulsion, which generically depicts the dominant transport mechanism in cooperative strong e-ph interaction systems, was studied numerically as well as analytically. Employing modified Lanczos algorithm, we showed that, as the repulsion is tuned, the system undergoes a first-order transition from superfluid to either a CDW or a checkerboard supersolid. The highlight of this work was the use of Green's function technique to exactly obtain the critical repulsion for two limiting cases, i.e., the two-HCB case (corresponding to zero filling in the thermodynamic limit) and the half-filled system. However, for the intermediate filling fractions, a finite-size scaling analysis was done. It would be very interesting to see if the critical repulsion for these intermediate fillings can as well be obtained using Green's function technique. We hope that this technique, whose utility is shown in this work, will also be useful to solve more complicated problems in the future. Finally, we would like to emphasize that in 1D, $t_2 - V$ model is indeed the minimum model to realize checkerboard supersolid phase, thereby adding to the significance of this apparently simple model. Moreover, with advancements in artificially engineered systems such as optical lattices, this system is potentially realizable in experiments as well.

In the next chapter, we have studied a two-dimensional square lattice system of HCBs coupled to archetypal cooperative/coherent normal-mode distortions such as those in per-

ovskites. At strong HCB-ph coupling, the effective Hamiltonian was obtained to be of the form $t_1 - t_2 - t_3 - V_1 - V_2 - V_3$ involving NN, NNN, and NNNN hoppings and repulsions. Using stochastic series expansion (SSE) quantum Monte Carlo, we constructed the phase diagram of the system. As the coupling strength was increased, we found that the system undergoes a first-order quantum phase transition from a superfluid to a checkerboard solid at half-filling and from a superfluid to a diagonal striped solid [with crystalline ordering wave vector $\vec{Q} = (2\pi/3, 2\pi/3)$ or $(2\pi/3, 4\pi/3)$] at one-third filling without showing any evidence of supersolidity. On tuning the system away from these commensurate fillings, checkerboard supersolid was generated near half-filling whereas a rare diagonal striped supersolid was realized near one-third filling. Possible mechanisms behind the formation of the CDWs as well as supersolid regions were also discussed based on the interactions of the system. We have also showed that $t_1 - V_1 - V_2 - V_3$ is the minimum model for realization of the diagonal striped supersolid phase on a square lattice. The success of this work lies in the fact that, based on our HCB model, we could explain the experimentally observed charge ordering in $La_{2-x}Sr_xNiO_4$ (LSNO) for hole doping $x = 1/2$ and $x = 1/3$. Considering cooperative Jahn-Teller (CJT) effect, we showed that the Hamiltonian governing LSNO involves same interaction terms as those in our model; however, LSNO deals with electrons instead of HCBs. Since, repulsion was the main reason behind the formation of the CDWs at those two fillings and hopping did not play any role, our HCB model was able to reproduce the experimental results of the electronic system. Thus our work led to the resolution of a prolonged controversy regarding the necessity of CJT distortions to explain the observed diagonal-stripe charge order at one-third doping in LSNO. Because of the so-called sign problem of quantum Monte Carlo methods, we could not simulate the model with electrons. It would be fascinating to examine if the $t_1 - t_2 - t_3 - V_1 - V_2 - V_3$ model with electrons could capture the experimental observations of LSNO at other fillings

as well, including the metal-insulator transition at $x \sim 0.9$.

Lastly in Chapter 4, we have dealt with the two-dimensional Hubbard-Holstein model in the regimes of strong e-e and strong e-ph interactions. In the parameter region where the system manifests the existence of a correlated singlet phase, the effective Hamiltonian was shown to transform to a $t_1 - V_1 - V_2 - V_3$ Hamiltonian for HCBs on a checkerboard lattice. Employing SSE, we observed that for large off-site repulsions, at filling $1/8$, the system manifests a diagonal striped solid with ordering wavevector $\vec{Q} = (\pi/4, 3\pi/4)$ or $(\pi/4, 5\pi/4)$. In striking contrast to the one-dimensional situation, our results in the two-dimensional case reveal a supersolid phase (corresponding to the diagonal striped solid) around filling $1/8$. We were able to explain intuitively the mechanism responsible for the formation of the CDW as well as the supersolid regions, both in the interstitial side and the vacancy side of the CDW. Varying the NNNN repulsion V_3 (where NNN repulsion $V_2 = 2V_3$) and the density of particles with a fixed NN repulsion, we also performed a general study of the model, which does not necessarily correspond to the correlated singlet phase of the Hubbard-Holstein model, and constructed the ground state phase diagram. We observed that as the NNNN repulsion is decreased, at filling $1/8$, the system undergoes a first-order transition from a diagonal striped solid to a superfluid phase. Furthermore, for small off-site repulsions, we witnessed a valence bond solid at one-fourth filling and tiny phase-separated regions at slightly higher fillings.

In the last two chapters, Chapter 3 and Chapter 4, we have used SSE to investigate the various properties of the systems. It is widely known that SSE works well for systems with comparable energy scales of diagonal and off-diagonal terms. In our systems, the energy scales had large disparity with the repulsions being almost infinity compared to the hopping terms. If we had to use the exact values of the repulsions, simulation times for SSE would have been prohibitively large. Therefore, based on physical reasoning, we used

146

cutoff values for the repulsions such that the essential physics is still captured. Although large values of repulsion slows down the simulation, we kept the cutoff values as high as possible within our time-frame. As discussed in Chapter 3, the small parameter ϵ affects the autocorrelation times of observables. While increasing the value of ϵ helps in reducing the autocorrelation, making it larger or comparable to the repulsion values may lead to unphysical results. Keeping these in mind, we optimized the parameter ϵ to obtain the best results while handling the large repulsion problem.

FINITE SIZE SCALING ANALYSIS FOR HCBS IN $t_2 - V$ MODEL FOR E-RINGS

In this section, we will outline our approach to carrying out finite size scaling analysis for a system with even number of sites. Let us first consider a non-interacting system (with $2N$ sites and N_p particles) described by a tight-binding Hamiltonian. For even number of particles, the ground state has particles occupying momenta $\frac{(2m+1)\pi}{2N}$ with $-N_p/2 \leq m \leq N_p/2 - 1$; whereas for odd number of particles the ground state is represented by particle momenta $\frac{(2m)\pi}{2N}$ with $-(N_p - 1)/2 \leq m \leq (N_p - 1)/2$. Thus the ground state wavefunction (due to the occupied momenta) is an even function of $1/2N$. Now, for the case corresponding to after the phase transition where all the particles are in the same sublattice C, the energy of the ground state $|\phi_0\rangle$ is given by

$$E_I = \sum_{i=1}^{N} \langle \phi_0 | - t_2 (c_i^\dagger c_{i+1} + \text{H.c.}) | \phi_0 \rangle, \qquad (A.1)$$

148

where c is the destruction operator for a HCB in sublattice C. Upon taking into account discrete translational symmetry, we get

$$\frac{E_I}{N} = \langle \phi_0 | - t_2 (c_i^\dagger c_{i+1} + \text{H.c.}) | \phi_0 \rangle. \tag{A.2}$$

Since $|\phi_0\rangle$ is even in $1/2N$, we note that $\frac{E_I}{N}$ is also even in $1/2N$.

Next, consider the interacting system characterized by the following $t_2 - V$ Hamiltonian in rings with even number of sites $(2N)$ and with periodic boundary conditions:

$$H \equiv \quad -t_2 \sum_{i=1}^{N} (c_i^\dagger c_{i+1} + \text{H.c.}) - t_2 \sum_{i=1}^{N} (d_i^\dagger d_{i+1} + \text{H.c.})$$
$$+ V \sum_{i=1}^{N} d_i^\dagger d_i (c_i^\dagger c_i + c_{i-1}^\dagger c_{i-1}), \tag{A.3}$$

where c (d) is the destruction operator for HCB in sublattice C (D) and $V \geq 0$. Upon invoking reflection symmetry, we note that the ground state will be invariant when the sign of momenta is reversed; equivalently the ground state $|\psi_0\rangle$ is an even function of $1/2N$. The ground state energy, before the phase transition, is given by

$$E_{II} = \sum_{i=1}^{N} \langle \psi_0 | - t_2 [(c_i^\dagger c_{i+1} + \text{H.c.}) + (d_i^\dagger d_{i+1} + \text{H.c.})] | \psi_0 \rangle$$
$$+ \sum_{i=1}^{N} \langle \psi_0 | V d_i^\dagger d_i (c_i^\dagger c_i + c_{i-1}^\dagger c_{i-1}) | \psi_0 \rangle. \tag{A.4}$$

Upon recognizing discrete translational invariance, we see that

$$\frac{E_{II}}{N} = \langle \psi_0 | - t_2 [(c_i^\dagger c_{i+1} + \text{H.c.}) + (d_i^\dagger d_{i+1} + \text{H.c.})] | \psi_0 \rangle$$
$$+ \langle \psi_0 | V d_i^\dagger d_i (c_i^\dagger c_i + c_{i-1}^\dagger c_{i-1}) | \psi_0 \rangle. \tag{A.5}$$

Since, $|\psi_0\rangle$ is even in $1/2N$, it follows that $\frac{E_{II}}{N}$ is also even in $1/2N$.

Now, at the transition point (corresponding to a critical interaction V_c), $\frac{E_{II}}{N} - \frac{E_I}{N} = 0$; this implies that

$$
\begin{aligned}
V_c &= \frac{\langle\psi_0|t_2[(c_i^\dagger c_{i+1} + \text{H.c.}) + (d_i^\dagger d_{i+1} + \text{H.c.})]|\psi_0\rangle}{\langle\psi_0|d_i^\dagger d_i(c_i^\dagger c_i + c_{i-1}^\dagger c_{i-1})|\psi_0\rangle} \\
&\quad - \frac{\langle\phi_0|t_2(c_i^\dagger c_{i+1} + \text{H.c.})|\phi_0\rangle}{\langle\psi_0|d_i^\dagger d_i(c_i^\dagger c_i + c_{i-1}^\dagger c_{i-1})|\psi_0\rangle}.
\end{aligned}
\tag{A.6}
$$

In the above equation, because both numerator and denominator of all the terms on the right-hand side are even in $1/2N$, it follows that V_c is also even in $1/2N$. Thus, for e-rings at various fillings, we relate $V_c(2N)$ (critical repulsion at $N_s = 2N$) to $V_c(\infty)$ as follows:

$$
V_c(2N) - V_c(\infty) = \frac{A}{N^2} + \frac{B}{N^4} + \ldots,
\tag{A.7}
$$

where A, B,... are constants.

It is also important to note that we used general arguments to show that the ground state energy $\frac{E_{II}}{N}$ is even in $1/2N$; these arguments can be extended to show that the ground state energies of other interacting systems such as the $t - V$ model are also even functions of $1/2N$. The fact that the ground state energy of the $t - V$ model is an even function of $1/2N$ has been used in Ref. [41].

NEAREST-NEIGHBOR REPULSION

The second order perturbation term is given by

$$H^{(2)} = -\sum_m \sum_{i,j,k,l} \frac{\langle 0|_{ph} H_{1i,j} |m\rangle_{ph} \langle m|_{ph} H_{1k,l} |0\rangle_{ph}}{E_0^{ph} - E_m^{ph}}$$

$$= -t_1^2 \sum_m \sum_{i,j,k,l} \frac{1}{\Delta E_m^{ph}} \Big[\Big(d_{i+1,j}^\dagger d_{i,j} \langle 0|_{ph} (\tau_{-x}^{ij} - 1) |m\rangle_{ph}$$

$$+ d_{i,j}^\dagger d_{i+1,j} \langle 0|_{ph} (\tau_{+x}^{ij} - 1) |m\rangle_{ph}$$

$$+ d_{i,j+1}^\dagger d_{i,j} \langle 0|_{ph} (\tau_{-y}^{ij} - 1) |m\rangle_{ph}$$

$$+ d_{i,j}^\dagger d_{i,j+1} \langle 0|_{ph} (\tau_{+y}^{ij} - 1) |m\rangle_{ph} \Big)$$

$$\times \Big(d_{k+1,l}^\dagger d_{k,l} \langle m|_{ph} (\tau_{+x}^{kl\,\dagger} - 1) |0\rangle_{ph}$$

$$+ d_{k,l}^\dagger d_{k+1,l} \langle m|_{ph} (\tau_{-x}^{kl\,\dagger} - 1)) |0\rangle_{ph}$$

$$+ d_{k,l+1}^\dagger d_{k,l} \langle m|_{ph} (\tau_{+y}^{kl\,\dagger} - 1)) |0\rangle_{ph}$$

$$+ d_{k,l}^\dagger d_{k,l+1} \langle m|_{ph} (\tau_{-y}^{kl\,\dagger} - 1)) |0\rangle_{ph} \Big) \Big], \qquad \text{(B.1)}$$

where $t_1 = te^{-(E_p + V_p)/\omega_0}$ and $\Delta E_m^{ph} = E_0^{ph} - E_m^{ph}$.

As already mentioned in Sec. 3.2.1, the NN repulsion results from a process where a particle hops to its neighboring site and returns back, which in 2D consists of two terms:

$$\sum_{i,j} \left[n_{i,j}(1 - n_{i+1,j}) + n_{i+1,j}(1 - n_{i,j}) \right] \text{ and } \sum_{i,j} \left[n_{i,j}(1 - n_{i,j+1}) + n_{i,j+1}(1 - n_{i,j}) \right].$$

Since, $\sum_{i,j} n_{i,j}(1 - n_{i+1,j}) = \sum_{i,j} n_{i+1,j}(1 - n_{i,j})$ and $\sum_{i,j} n_{i,j}(1 - n_{i,j+1}) = \sum_{i,j} n_{i,j+1}(1 - n_{i,j})$, so the process is effectively given by $\sum_{i,j} \left[n_{i,j}(1 - n_{i+1,j}) + n_{i,j}(1 - n_{i,j+1}) \right]$ with the coefficient being twice.

Now, we can rewrite the term $\sum_{i,j} n_{i,j}(1 - n_{i+1,j})$ as

$$\sum_{i,j} d_{i,j}^\dagger d_{i,j}(1 - d_{i+1,j}^\dagger d_{i+1,j}) = \sum_{i,j} d_{i,j}^\dagger d_{i,j} d_{i+1,j} d_{i+1,j}^\dagger = \sum_{i,j} d_{i,j}^\dagger d_{i+1,j} d_{i+1,j}^\dagger d_{i,j}.$$

Looking at the expression of $H^{(2)}$, one can figure out that the above term comes from the multiplication of the terms $d_{i,j}^\dagger d_{i+1,j}$ and $d_{k+1,l}^\dagger d_{k,l}$ for $k = i$ and $l = j$. So, the coefficient of this term is given by

$$t_1^2 \sum_m \frac{\langle 0|_{ph}(\tau_{+x}^{ij} - 1)|m\rangle_{ph}\langle m|_{ph}(\tau_{+x}^{ij}{}^\dagger - 1)|0\rangle_{ph}}{\Delta E_m^{ph}}, \tag{B.2}$$

where

$$\tau_{+x}^{ij} = \exp\left[g(2a_{i,j} - a_{i-1,j} - a_{i+1,j}) + g(b_{i+1,j-1} + b_{i,j} - b_{i,j-1} - b_{i+1,j}) + \gamma g(c_{i,j} - c_{i+1,j}) \right];$$

consequently, the coefficient simplifies exactly to be $\frac{t_1^2}{\omega_0} G_9(4, 1, 1, 1, 1, 1, 1, \gamma^2, \gamma^2)$. Now, the general form $G_n(\alpha_1, \alpha_2, \cdots, \alpha_n)$ can be expressed as

$$G_n(\alpha_1, \alpha_2, \cdots, \alpha_n) = \sideset{}{'}\sum_{m_1, m_2, \ldots, m_n} \frac{(\alpha_1 g^2)^{m_1} \cdots (\alpha_n g^2)^{m_n}}{m_1! \cdots m_n!(m_1 + \cdots + m_n)},$$

where $m_i = 0, 1, 2, ..., \infty$ and the prime in $\sum'$ implies the case $m_1 = m_2 = ... = m_n = 0$ is excluded from the summation. It is important to note that for large values of g^2, G_n can be approximately expressed as

$$G_n(\alpha_1, \alpha_2, \cdots, \alpha_n) \approx \frac{\exp\left(\sum\limits_{i=1}^{n} \alpha_i g^2\right)}{\sum\limits_{i=1}^{n} \alpha_i g^2}.$$

(B.3)

Then, the NN repulsion is given by

$$-V_z \sum_{i,j} [n_{i,j}(1 - n_{i+1,j}) + n_{i,j}(1 - n_{i,j+1})],$$

(B.4)

where

$$V_z = \frac{2t^2 e^{-2(E_p + V_p)/\omega_0}}{\omega_0} G_9(4, 1, 1, 1, 1, 1, 1, \gamma^2, \gamma^2) \approx \frac{2t^2}{2E_p + 2V_p}.$$

(B.5)

Now, in arriving at Eq. (B.4), we did not take into account the occupancy of the neighbors of the intermediate site. For example, when the particle hops from site (i, j) to NN site $(i+1, j)$ and back, we have not considered the occupancy of the sites $(i+2, j)$, $(i+1, j+1)$ and $(i+1, j-1)$, which are the neighboring sites of the intermediate site $(i+1, j)$ (as can be seen from Fig. 3.1). We will consider this occupancy in the next appendix.

NNN REPULSION AND NNNN

REPULSION

In this appendix we first outline the procedure of calculating the coefficient of next-nearest-neighbor (NNN) repulsion which occurs along the diagonals. Consider the case where a particle hops to its neighboring site and returns back yielding the term $\propto \sum_{<i,j>} n_i(1 - n_j)$ with $< i,j >$ indicating nearest-neighbor (NN) pairs of sites. In this process we have to take into account the occupancy of the neighboring sites of the intermediate site j. For example, in Fig. C.1, if a particle at site 1 hops to site 2 and comes back, then the coefficient of this process depends on the occupancy of the sites 3, 4, and 5. If all the three sites are empty, then this term can be expressed as $-V_z n_1(1 - n_3)(1 - n_4)(1 - n_5)$ where $V_z \approx \frac{2t^2}{2E_p + 2V_p}$; here, we have omitted the term $(1 - n_2)$ because the possibility of NN occupancy (for particle at site 1) is already excluded from the process due to the large value of NN repulsion $2V_p$. Due to numerical difficulties in our simulations using SSE, we need to simplify the four-operator term into a two-operator one by applying mean field to

154
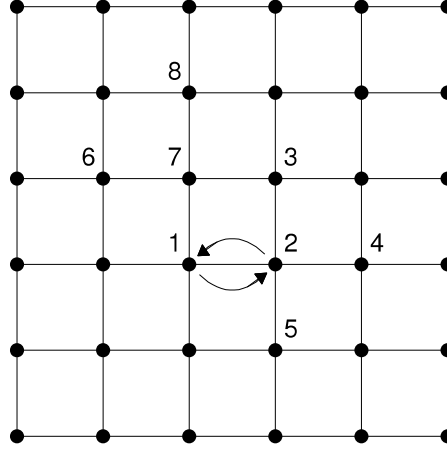
Figure C.1: Pictorial description of the process where a particle at site 1 hops to site 2 and comes back.

the remaining two operators. One can easily see that this mean-field procedure leaves us with a term which represents NNN repulsion (which acts along the diagonals) or NNNN repulsion (which acts along the axes).

We will now calculate the NNN repulsion coefficient which pertains to the diagonals of the square lattice in Fig. C.1. To this end, we consider all the possible processes yielding the operator $n_1 n_3$ and add all the corresponding terms to evaluate its coefficient. The following are the relevant cases.

Case 1 : NNN interaction, when all the three neighboring sites of the intermediate site are unoccupied, involves the following.

(i) The contribution of particle hopping from site 1 to site 2 and coming back:

$$
\begin{aligned}
&= -\frac{2t^2}{(2E_p + 2V_p)} n_1(1 - n_3)(1 - n_4)(1 - n_5) \\
&\approx -\frac{2t^2}{(2E_p + 2V_p)} n_1(1 - n_3)\langle 1 - n_4\rangle\langle 1 - n_5\rangle \\
&\approx -\frac{2t^2}{(2E_p + 2V_p)} n_1(1 - n_3)\left(\frac{1}{2} - m\right)^2,
\end{aligned}
\tag{C.1}
$$

155

where $\langle ... \rangle$ implies mean value and $\langle 1 - n_4 \rangle = \langle 1 - n_5 \rangle = (\frac{1}{2} - m)$ with m being the magnetization of the system.

(ii) The contribution of particle hopping from site 1 to site 7 and returning back involves a similar situation as (i) and is given as:

$$\approx -\frac{2t^2}{(2E_p + 2V_p)} n_1 (1 - n_3) \langle 1 - n_6 \rangle \langle 1 - n_8 \rangle$$
$$\approx -\frac{2t^2}{(2E_p + 2V_p)} n_1 (1 - n_3) \left(\frac{1}{2} - m \right)^2 . \tag{C.2}$$

(iii) The contribution of particle hopping from site 3 to site 2 and coming back:

$$\approx -\frac{2t^2}{(2E_p + 2V_p)} n_3 (1 - n_1) \langle 1 - n_4 \rangle \langle 1 - n_5 \rangle$$
$$\approx -\frac{2t^2}{(2E_p + 2V_p)} n_3 (1 - n_1) \left(\frac{1}{2} - m \right)^2 . \tag{C.3}$$

(iv) The particle hopping from site 3 to site 7 and returning back is similar to (iii) and yields the same expression as Eq. (C.3).

(v) The contribution of particle hopping from site 4 to site 2 and coming back:

$$\approx -\frac{2t^2}{(2E_p + 2V_p)} (1 - n_3)(1 - n_1) \langle n_4 \rangle \langle 1 - n_5 \rangle$$
$$\approx -\frac{2t^2}{(2E_p + 2V_p)} (1 - n_3)(1 - n_1) \left(\frac{1}{4} - m^2 \right)^2 . \tag{C.4}$$

(vi) The contribution of particle hopping from site 5 to site 2 and coming back is similar to (v) and is given by Eq.(C.4).

(vii) The particle hopping from site 6 to site 7 and returning back is also similar to (v) and the contribution is again given by Eq.(C.4).

(viii) The contribution of particle hopping from site 8 to site 7 and coming back is also similar to (v) and hence is given by Eq.(C.4).

Adding all the contributions for case 1, we get the coefficient of $n_1 n_3$ to be

$$\frac{2t^2}{(2E_p + 2V_p)} \left[4\left(\frac{1}{2} - m\right)^2 - 4\left(\frac{1}{4} - m^2\right) \right]. \tag{C.5}$$

Case 2: We consider contribution to NNN interaction when, among the three sites that are NN to the intermediate site, one of them is occupied and the other two are empty. Thus, compared to case 1, there is an extra repulsion term $2V_p$ in the denominator of the coefficient. Then, NNN interaction involves the following.

(i) The particle hops from site 1 to site 2 and comes back. Any one of the three neighboring sites of site 2, i.e., 3, 4, or 5, is occupied; then, the contribution is:

$$\approx -\frac{2t^2}{(2E_p + 4V_p)} \Big[n_1 n_3 \langle 1 - n_4 \rangle \langle 1 - n_5 \rangle + n_1 (1 - n_3) \langle n_4 \rangle \langle 1 - n_5 \rangle$$

$$+ n_1 (1 - n_3) \langle 1 - n_4 \rangle \langle n_5 \rangle \Big]$$

$$\approx -\frac{2t^2}{(2E_p + 4V_p)} \left[n_1 n_3 \left(\frac{1}{2} - m\right)^2 + 2n_1 (1 - n_3) \left(\frac{1}{4} - m^2\right) \right]. \tag{C.6}$$

(ii) The particle hops from site 1 to site 7 and comes back. The situation is similar to (i) and hence the contribution is given by Eq. (C.6).

(iii) The particle hops from site 3 to site 2 and comes back. The resulting contribution is

$$\approx -\frac{2t^2}{(2E_p + 4V_p)} \Big[n_3 n_1 \langle 1 - n_4 \rangle \langle 1 - n_5 \rangle + n_3 (1 - n_1) \langle n_5 \rangle \langle 1 - n_4 \rangle$$

$$+ n_3 (1 - n_1) \langle n_4 \rangle \langle 1 - n_5 \rangle \Big]$$

$$\approx -\frac{2t^2}{(2E_p + 4V_p)} \left[n_1 n_3 \left(\frac{1}{2} - m \right)^2 + 2 n_3 (1 - n_1) \left(\frac{1}{4} - m^2 \right) \right]. \qquad (C.7)$$

(iv) The particle hops from site 3 to site 7 and returns back. Since the situation is similar to (iii), the contribution is expressed by Eq. (C.7).

(v) The particle hops from site 4 to site 2 and comes back. The contribution is

$$\approx -\frac{2t^2}{(2E_p + 4V_p)} \Big[\langle n_4 \rangle (1 - n_1) n_3 \langle 1 - n_5 \rangle + \langle n_4 \rangle n_1 (1 - n_3) \langle 1 - n_5 \rangle$$

$$+ \langle n_4 \rangle (1 - n_1)(1 - n_3) \langle n_5 \rangle \Big]$$

$$\approx -\frac{2t^2}{(2E_p + 4V_p)} \left[n_1 (1 - n_3) \left(\frac{1}{4} - m^2 \right) + n_3 (1 - n_1) \left(\frac{1}{4} - m^2 \right) \right.$$

$$\left. + (1 - n_1)(1 - n_3) \left(\frac{1}{2} + m \right)^2 \right]. \qquad (C.8)$$

(vi) The particle hops from site 5 to site 2 and comes back. The situation being similar to (v) leads to the contribution being given by Eq. (C.8).

(vii) The particle hops from site 6 to site 7 and comes back; this circumstance is also similar to (v) and hence contribution same as in Eq. (C.8).

(viii) The particle hops from site 8 to site 7 and comes back. Here too the contribution is given by Eq. (C.8) since the circumstance is again similar to (v).

Therefore, for case 2, the sum total of the above contributions yields the coefficient of $n_1 n_3$

to be

$$\frac{2t^2}{(2E_p + 4V_p)} \left[16 \left(\frac{1}{4} - m^2 \right) - 4 \left(\frac{1}{2} - m \right)^2 - 4 \left(\frac{1}{2} + m \right)^2 \right]. \qquad \text{(C.9)}$$

Case 3: Contribution to NNN interaction when the intermediate site has any two of the three NN sites occupied with the other being empty. Then, compared to case 2, the coefficient has an extra repulsion term $2V_p$ in the denominator; consequently, NNN interaction involves the following.

(i) The particle hops from site 1 to site 2 and comes back; the resulting contribution is:

$$\approx -\frac{2t^2}{(2E_p + 6V_p)} \left[n_1 n_3 \langle n_4 \rangle \langle 1 - n_5 \rangle + n_1 n_3 \langle 1 - n_4 \rangle \langle n_5 \rangle + n_1 (1 - n_3) \langle n_4 \rangle \langle n_5 \rangle \right]$$

$$\approx -\frac{2t^2}{(2E_p + 6V_p)} \left[2n_1 n_3 \left(\frac{1}{4} - m^2 \right) + n_1 (1 - n_3) \left(\frac{1}{2} + m \right)^2 \right]. \qquad \text{(C.10)}$$

(ii) The particle hops from site 1 to site 7 and comes back. This situation is similar to (i) with the contribution being expressed by Eq. (C.10).

(iii) The particle hops from site 3 to site 2 and returns; the ensuing contribution is:

$$\approx -\frac{2t^2}{(2E_p + 6V_p)} \left[n_3 n_1 \langle 1 - n_4 \rangle \langle n_5 \rangle + n_3 n_1 \langle n_4 \rangle \langle 1 - n_5 \rangle + n_3 (1 - n_1) \langle n_4 \rangle \langle n_5 \rangle \right]$$

$$\approx -\frac{2t^2}{(2E_p + 6V_p)} \left[2n_1 n_3 \left(\frac{1}{4} - m^2 \right) + n_3 (1 - n_1) \left(\frac{1}{2} + m \right)^2 \right]. \qquad \text{(C.11)}$$

(iv) The particle hops from site 3 to site 7 and comes back. The situation is similar to (iii) with the contribution being given by Eq. (C.11).

(v) The particle hops from site 4 to site 2 and returns. This produces the contribution:

$$
\approx -\frac{2t^2}{(2E_p + 6V_p)}\Big[\langle n_4\rangle n_1 n_3\langle 1 - n_5\rangle + \langle n_4\rangle(1 - n_1)n_3\langle n_5\rangle + \langle n_4\rangle n_1(1 - n_3)\langle n_5\rangle\Big]
$$

$$
\approx -\frac{2t^2}{(2E_p + 6V_p)}\left[n_1 n_3\left(\frac{1}{4} - m^2\right) + n_1(1 - n_3)\left(\frac{1}{2} + m\right)^2 + n_3(1 - n_1)\left(\frac{1}{2} + m\right)^2\right].
$$

$$(C.12)$$

(vi) The particle hops from site 5 to site 2 and comes back. The circumstance, being similar to (v), yields the contribution expressed in Eq. (C.12).

(vii) The particle hops from site 6 to site 7 and comes back. The situation is also similar to (v) with the contribution being also given by Eq. (C.12).

(viii) The particle hops from site 8 to site 7 and returns. Again the situation is similar to (v) with the contribution being again given by Eq. (C.12).

Therefore, on adding all the various contributions for case 3, we get the coefficient of $n_1 n_3$ to be

$$
\frac{2t^2}{(2E_p + 6V_p)}\left[12\left(\frac{1}{2} + m\right)^2 - 12\left(\frac{1}{4} - m^2\right)\right]. \qquad (C.13)
$$

Case 4: Contribution to NNN interaction when all of the three neighboring sites of the intermediate site are occupied. Here, compared to case 3, the coefficient has an extra repulsion term $2V_p$ in the denominator. Then, NNN interaction involves the following.

(i) The particle hops from site 1 to site 2 and comes back. Consequently, the contribution is

$$
\approx -\frac{2t^2}{(2E_p + 8V_p)}n_1 n_3\langle n_4\rangle\langle n_5\rangle \approx -\frac{2t^2}{(2E_p + 8V_p)}n_1 n_3\left(\frac{1}{2} + m\right)^2. \qquad (C.14)
$$

For all the following also the contribution is expressed by Eq. (C.14) because the situation is similar to (i).

(ii) The particle hops from site 1 to site 7 and comes back. (iii) The particle hops from site 3 to site 2 and returns. (iv) The particle hops from site 3 to site 7 and comes back. (v) The particle hops from site 4 to site 2 and comes back. (vi) The particle hops from site 5 to site 2 and returns. (vii) The particle hops from site 6 to site 7 and comes back. (viii) The particle hops from site 8 to site 7 and returns.

Therefore, for case 4, the coefficient of $n_1 n_3$ is given by

$$-\frac{2t^2}{(2E_p + 8V_p)} \times 8 \left(\frac{1}{2} + m \right)^2.$$

(C.15)

Combining Eqs. (C.5), (C.9), (C.13) and (C.15), we finally get the coefficient of NNN repulsion (which acts along the diagonals) to be

$$\begin{aligned}
V_2 = 2t^2 \Bigg[&\left(\frac{1}{2} - m \right)^2 \frac{2V_p}{(E_p + V_p)(E_p + 2V_p)} \\
&+ \left(\frac{1}{4} - m^2 \right) \frac{4E_p V_p}{(E_p + V_p)(E_p + 2V_p)(E_p + 3V_p)} \\
&+ \left(\frac{1}{2} + m \right)^2 \frac{2E_p V_p}{(E_p + 2V_p)(E_p + 3V_p)(E_p + 4V_p)} \Bigg].
\end{aligned}$$

(C.16)

To calculate the NNNN repulsion along the x axis (y axis), we have to consider all the processes from which a term $n_1 n_4$ ($n_1 n_8$) can appear. Adding all those terms, we can see that the coefficient of NNNN repulsion is just half of the coefficient of NNN repulsion. The reason for this is that the relevant contributions are from only half of the eight situations considered in each of the above four occupancy cases (i.e, the four cases involving different number of occupied neighbors for the intermediate site).

NNN HOPPING AND NNNN HOPPING

There are two possible hopping paths for a particle to arrive at a NNN site along the diagonals of the square lattice. For example, in Fig. D.1, consider a particle hopping from site 1 to site 3. It can either hop to site 2 first and then to site 3 or it can hop to site 4 followed by a hop to site 3. Now, the coefficient of this process gets modified by the occupancy of the neighboring sites of the intermediate site. Without taking into account this effect, the process along any one path [on using Eq. (B.1)] is given exactly by

$$-\frac{t^2 e^{-2(E_p + V_p)/\omega_0}}{\omega_0} G_5(2, 2, 1, 1, \gamma^2) \sum_{<<i,j>>} (d_i^\dagger d_j + \text{H.c.}),$$

where $<< i, j >>$ denotes NNN pairs of sites along the diagonals. For large values of g^2, we have the following simplification for the coefficient in the above expression:

$$\frac{t^2 e^{-2(E_p + V_p)/\omega_0}}{\omega_0} G_5(2, 2, 1, 1, \gamma^2) \approx \frac{t^2 e^{-E_p/\omega_0}}{E_p + 2V_p}.$$

Path 1: The particle hops from site 1 to site 3 via site 2. The coefficient of this process

162
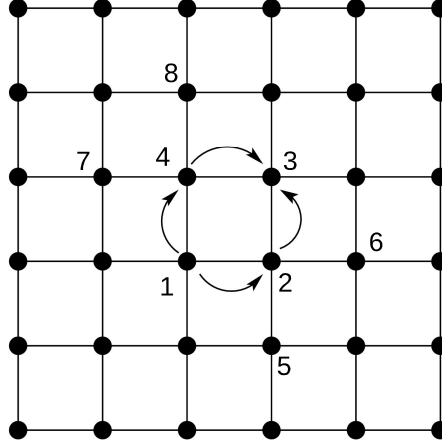
Figure D.1: Pictorial depiction of the process where a particle at site 1 hops to site 3 which is its NNN site along diagonal. The two possible paths for this process are indicated: hopping to site 3 via site 2 and site 4.

depends on the occupancy of the sites 5 and 6 which are the two neighboring sites of the intermediate site 2.

Case 1: Contribution to NNN hopping when both the neighboring sites are empty:

$$-\frac{t^2 e^{-E_p/\omega_0}}{E_p + 2V_p} d_3^\dagger d_1 (1 - n_5)(1 - n_6) \approx -\frac{t^2 e^{-E_p/\omega_0}}{E_p + 2V_p} d_3^\dagger d_1 \langle 1 - n_5 \rangle \langle 1 - n_6 \rangle$$

$$\approx -\frac{t^2 e^{-E_p/\omega_0}}{E_p + 2V_p} \left(\frac{1}{2} - m \right)^2 d_3^\dagger d_1. \qquad (D.1)$$

Case 2: Contribution when any one of the neighboring sites is occupied (giving an extra repulsion $2V_p$ in the denominator) and the other site is empty:

$$\approx -\frac{t^2 e^{-E_p/\omega_0}}{E_p + 4V_p} d_3^\dagger d_1 \left[\langle n_5 \rangle \langle 1 - n_6 \rangle + \langle 1 - n_5 \rangle \langle n_6 \rangle \right]$$

$$\approx -\frac{2t^2 e^{-E_p/\omega_0}}{E_p + 4V_p} \left(\frac{1}{4} - m^2 \right) d_3^\dagger d_1. \qquad (D.2)$$

163

Case 3: Contribution when both the NN sites are occupied:

$$\approx -\frac{t^2 e^{-E_p/\omega_0}}{E_p + 6V_p} d_3^\dagger d_1 \langle n_5 \rangle \langle n_6 \rangle \approx -\frac{t^2 e^{-E_p/\omega_0}}{E_p + 6V_p} \left(\frac{1}{2} + m\right)^2 d_3^\dagger d_1. \tag{D.3}$$

Therefore, for path 1, we get the coefficient of $d_3^\dagger d_1$ to be

$$-t^2 e^{-E_p/\omega_0} \left[\left(\frac{1}{2} - m\right)^2 \frac{1}{E_p + 2V_p} + \left(\frac{1}{4} - m^2\right) \frac{2}{E_p + 4V_p} \right.$$
$$\left. + \left(\frac{1}{2} + m\right)^2 \frac{1}{E_p + 6V_p} \right]. \tag{D.4}$$

Path 2: The particle hops from site 1 to site 4 first and then to site 3. The coefficient of this process gets modified depending on whether the sites 7 and 8 (NN to the intermediate site 4) are occupied or not.

Case 1 : Contribution when both the neighboring sites are empty. This situation is similar to case 1 of path 1; hence, the contribution is given by Eq. (D.1).

Case 2 : Contribution when any one of the neighboring sites is occupied and the other one is empty. This is similar to case 2 of path 1; consequently, the contribution is expressed by Eq. (D.2).

Case 3 : Contribution when both the NN sites are occupied. This circumstance is similar to case 3 of path 1; thus, the contribution is given by Eq. (D.3).

Thus we see that path 2 yields the same coefficient [given by Eq. (D.4)] for $d_3^\dagger d_1$ as path 1. Combining the contributions from both the paths, a particle hopping to its NNN along diagonals can be expressed as $-t_2 \sum_{<<i,j>>} (d_i^\dagger d_j + \text{H.c.})$, where the coefficient t_2 is

164

given by

$$t_2 = 2t^2 e^{-E_p/\omega_0} \left[\left(\frac{1}{2} - m \right)^2 \frac{1}{E_p + 2V_p} + \left(\frac{1}{4} - m^2 \right) \frac{2}{E_p + 4V_p} \right.$$
$$\left. + \left(\frac{1}{2} + m \right)^2 \frac{1}{E_p + 6V_p} \right]. \qquad (D.5)$$

For the case of NNNN hopping (which occurs along the axes), there is only one possible path. Hence, the relevant coefficient t_3 for NNNN hopping is half of the coefficient for NNN hopping, i.e., $t_3 = \frac{t_2}{2}$.

SSE BOND HAMILTONIAN

Our effective Hamiltonian for HCBs, written in units of $2t_1$, can be expressed in terms of bond operators as follows:

$$H = -\sum_{i=1}^{3}\sum_{B_i} H_{B_i},$$

(E.1)

where B_1, B_2 and B_3 represent NN, NNN and NNNN bonds in our system, respectively. In the above expression H_{B_i} can further be written as a sum of diagonal (H_{1,B_i}) and off-diagonal (H_{2,B_i}) parts, i.e., $H_{B_i} = H_{1,B_i} + H_{2,B_i}$. The expressions for the diagonal and off-diagonal parts are given as

$$H_{1,B_i} = C_i - \Delta_i S_{j(B_i)}^z S_{k(B_i)}^z + h_B \left(S_{j(B_i)}^z + S_{k(B_i)}^z \right)$$
$$H_{2,B_i} = \frac{J_i}{2} \left(S_{j(B_i)}^+ S_{k(B_i)}^- + \text{H.c.} \right),$$

(E.2)

where $J_1 = 1$, $C_i \equiv \Delta_i/4 + h_B + \epsilon_i$, $\epsilon_i \geq 0$ and $h_B = h/Z$; the coordination number $Z = 12$ for our problem. Furthermore, $j(B_i)$ and $k(B_i)$ refer to sites connecting the bond

B_i. The parameter ϵ_i is introduced to ensure that the two-spin matrix elements always stay positive.

BIBLIOGRAPHY

[1]   R. Peierls, *Annalen der Physik* **396** (1930) 121–148.

[2]   M. Boninsegni and N. V. Prokof'ev, *Rev. Mod. Phys.* **84** (May, 2012) 759–776.

[3]   E. Kim and M. H. W. Chan, *Nature* **427** (Jan, 2004) 225–227.

[4]   A. Gabovich, A. Voitenko and M. Ausloos, *Physics Reports* **367** (2002) 583 – 709.

[5]   S. H. Blanton, R. T. Collins, K. H. Kelleher, L. D. Rotter, Z. Schlesinger, D. G. Hinks et al., *Phys. Rev. B* **47** (Jan, 1993) 996–1001.

[6]   R. L. Withers and J. A. Wilson, *Journal of Physics C: Solid State Physics* **19** (1986) 4809.

[7]   J. Merino and R. H. McKenzie, *Phys. Rev. Lett.* **87** (Nov, 2001) 237002.

[8]   W. W. Fuller, P. M. Chaikin and N. P. Ong, *Phys. Rev. B* **24** (Aug, 1981) 1333–1338.

[9]   A. Rusydi, W. Ku, B. Schulz, R. Rauer, I. Mahns, D. Qi et al., *Phys. Rev. Lett.* **105** (Jul, 2010) 026402.

168

[10]   P. Abbamonte, G. Blumberg, A. Rusydi, A. Gozar, P. G. Evans, T. Siegrist et al.,
        Nature **431** (Oct, 2004) 1078–1081.

[11]   G. Bilbro and W. L. McMillan, *Phys. Rev. B* **14** (Sep, 1976) 1887–1892.

[12]   R. Landig, L. Hruby, N. Dogra, M. Landini, R. Mottl, T. Donner et al., *Nature* **532**
        (Apr, 2016) 476–479.

[13]   G. G. Batrouni and R. T. Scalettar, *Phys. Rev. Lett.* **84** (Feb, 2000) 1599–1602.

[14]   F. Hébert, G. G. Batrouni, R. T. Scalettar, G. Schmid, M. Troyer and A. Dorneich,
        Phys. Rev. B **65** (Dec, 2001) 014513.

[15]   L. Dang, M. Boninsegni and L. Pollet, *Phys. Rev. B* **78** (Oct, 2008) 132512.

[16]   B. Capogrosso-Sansone, C. Trefzger, M. Lewenstein, P. Zoller and G. Pupillo,
        Phys. Rev. Lett. **104** (Mar, 2010) 125301.

[17]   Y.-C. Chen, R. G. Melko, S. Wessel and Y.-J. Kao, *Phys. Rev. B* **77** (Jan, 2008)
        014524.

[18]   P. Sengupta, L. P. Pryadko, F. Alet, M. Troyer and G. Schmid, *Phys. Rev. Lett.* **94**
        (May, 2005) 207202.

[19]   G. Schmid and M. Troyer, *Phys. Rev. Lett.* **93** (Aug, 2004) 067003.

[20]   S. Kar and S. Yarlagadda, *Annals of Physics* **375** (2016) 322 – 336.

[21]   S. Datta and S. Yarlagadda, *Solid State Communications* **150** (2010) 2040 – 2044.

[22]   X. Huo, Y.-Y. Cui, D. Wang and J.-P. Lv, *Phys. Rev. A* **95** (Feb, 2017) 023613.

[23]   S. Wessel and M. Troyer, *Phys. Rev. Lett.* **95** (Sep, 2005) 127205.

[24] D. Heidarian and K. Damle, *Phys. Rev. Lett.* **95** (Sep, 2005) 127206.

[25] A. Sen, P. Dutt, K. Damle and R. Moessner, *Phys. Rev. Lett.* **100** (Apr, 2008) 147204.

[26] R. G. Melko, A. Paramekanti, A. A. Burkov, A. Vishwanath, D. N. Sheng and L. Balents, *Phys. Rev. Lett.* **95** (Sep, 2005) 127207.

[27] M. Boninsegni and N. Prokof'ev, *Phys. Rev. Lett.* **95** (Nov, 2005) 237204.

[28] R. G. Melko, A. Del Maestro and A. A. Burkov, *Phys. Rev. B* **74** (Dec, 2006) 214517.

[29] L. Pollet, J. D. Picon, H. P. Büchler and M. Troyer, *Phys. Rev. Lett.* **104** (Mar, 2010) 125302.

[30] S. Wessel, *Phys. Rev. B* **75** (May, 2007) 174301.

[31] J. Y. Gan, Y. C. Wen, J. Ye, T. Li, S.-J. Yang and Y. Yu, *Phys. Rev. B* **75** (Jun, 2007) 214509.

[32] T. Mishra, R. V. Pai and S. Mukerjee, *Phys. Rev. A* **89** (Jan, 2014) 013615.

[33] T. Bilitewski and N. R. Cooper, *Phys. Rev. A* **94** (Aug, 2016) 023630.

[34] A. Taraphder, R. Pandit, H. R. Krishnamurthy and T. V. Ramakrishnan, *International Journal of Modern Physics B* **10** (1996) 863–955.

[35] B. Lau, M. Berciu and G. A. Sawatzky, *Phys. Rev. B* **76** (Nov, 2007) 174305.

[36] G. L. Goodvin and M. Berciu, *Phys. Rev. B* **78** (Dec, 2008) 235120.

[37] B. Pahari, K. Ghoshray, R. Sarkar and A. Ghoshray, *Phys. Rev. B* **77** (Jun, 2008) 224429.

[38] S. Datta, A. Das and S. Yarlagadda, *Phys. Rev. B* **71** (Jun, 2005) 235118.

[39] R. Pankaj and S. Yarlagadda, *Phys. Rev. B* **86** (Jul, 2012) 035453.

[40] A. Ghosh and S. Yarlagadda, *Phys. Rev. B* **90** (Jul, 2014) 045140.

[41] E. R. Gagliano, E. Dagotto, A. Moreo and F. C. Alcaraz, *Phys. Rev. B* **34** (Aug, 1986) 1677–1682.

[42] C. M. Varma, *Phys. Rev. Lett.* **61** (Dec, 1988) 2713–2716.

[43] A. Ghosh and S. Yarlagadda, *Phys. Rev. B* **96** (Sep, 2017) 125108.

[44] A. W. Sandvik, *Phys. Rev. B* **56** (Nov, 1997) 11678–11690.

[45] H. Ulbrich and M. Braden, *Physica C: Superconductivity* **481** (2012) 31 − 45.

[46] C. H. Chen, S.-W. Cheong and A. S. Cooper, *Phys. Rev. Lett.* **71** (Oct, 1993) 2461–2464.

[47] S.-W. Cheong, H. Y. Hwang, C. H. Chen, B. Batlogg, L. W. Rupp and S. A. Carter, *Phys. Rev. B* **49** (Mar, 1994) 7088–7091.

[48] K. Ishizaka, Y. Taguchi, R. Kajimoto, H. Yoshizawa and Y. Tokura, *Phys. Rev. B* **67** (May, 2003) 184418.

[49] R. Kajimoto, T. Kakeshita, H. Yoshizawa, T. Tanabe, T. Katsufuji and Y. Tokura, *Phys. Rev. B* **64** (Sep, 2001) 144432.

[50] H. Yoshizawa, T. Kakeshita, R. Kajimoto, T. Tanabe, T. Katsufuji and Y. Tokura, *Phys. Rev. B* **61** (Jan, 2000) R854–R857.

[51] P. G. Freeman, A. T. Boothroyd, D. Prabhakaran, M. Enderle and C. Niedermayer, *Phys. Rev. B* **70** (Jul, 2004) 024413.

[52] L. Rademaker, Y. Pramudya, J. Zaanen and V. Dobrosavljević, *Phys. Rev. E* **88** (Sep, 2013) 032121.

[53] S. Reja, S. Yarlagadda and P. B. Littlewood, *Phys. Rev. B* **84** (Aug, 2011) 085127.

[54] S. Reja, S. Yarlagadda and P. B. Littlewood, *Phys. Rev. B* **86** (Jul, 2012) 045110.

[55] A. Ghosh, S. Kar and S. Yarlagadda, *ArXiv: 1803.03174* (Mar., 2018) , [1803.03174].

[56] G. Grüner, *Density waves in solids*, *Westview Press, 2000* .

[57] J. G. Bednorz and K. A. Müller, *Zeitschrift für Physik B Condensed Matter* **64** (Jun, 1986) 189–193.

[58] M. Fiebig, *Journal of Physics D: Applied Physics* **38** (2005) R123.

[59] A.-M. Haghiri-Gosnet and J.-P. Renard, *Journal of Physics D: Applied Physics* **36** (2003) R127.

[60] M. Greiter, *Physics Letters B* **336** (1994) 48 – 53.

[61] M. Udagawa and Y. Motome, *Phys. Rev. Lett.* **98** (May, 2007) 206405.

[62] V. Vescoli, L. Degiorgi, H. Berger and L. Forró, *Phys. Rev. Lett.* **81** (Jul, 1998) 453–456.

172

[63] W. Z. Hu, G. Li, J. Yan, H. H. Wen, G. Wu, X. H. Chen et al., *Phys. Rev. B* **76** (Jul, 2007) 045103.

[64] S. V. Borisenko, A. A. Kordyuk, A. N. Yaresko, V. B. Zabolotnyy, D. S. Inosov, R. Schuster et al., *Phys. Rev. Lett.* **100** (May, 2008) 196402.

[65] P. Kapitza, *Nature* **141** (Jan, 1938) 74.

[66] J. F. Allen and A. D. Misener, *Nature* **141** (Jan, 1938) 75.

[67] A. Altland and B. Simons, *Condensed matter field theory*, *Cambridge University Press, 2008* .

[68] D. J. Thouless, *Annals of Physics* **52** (May, 1969) 403–427.

[69] A. J. Andreev and I. Lifshitz, *JETP* **29** (1969) 1107–1113.

[70] E. Kim and M. H. W. Chan, *Science* **305** (2004) 1941–1944.

[71] Z. Nussinov, A. V. Balatsky, M. J. Graf and S. A. Trugman, *Phys. Rev. B* **76** (Jul, 2007) 014530.

[72] C.-D. Yoo and A. T. Dorsey, *Phys. Rev. B* **79** (Mar, 2009) 100504.

[73] J. T. West, O. Syshchenko, J. Beamish and M. H. W. Chan, *Nature Physics* **5** (Jul, 2009) 598–601.

[74] M. P. A. Fisher, P. B. Weichman, G. Grinstein and D. S. Fisher, *Phys. Rev. B* **40** (Jul, 1989) 546–570.

[75] D. Jaksch, C. Bruder, J. I. Cirac, C. W. Gardiner and P. Zoller, *Phys. Rev. Lett.* **81** (Oct, 1998) 3108–3111.

[76] C. Orzel, A. K. Tuchman, M. L. Fenselau, M. Yasuda and M. A. Kasevich, *Science* **291** (2001) 2386–2389.

[77] M. Greiner, O. Mandel, T. Esslinger, T. W. Hänsch and I. Bloch, *Nature* **415** (Jan, 2002) 39–44.

[78] L.-M. Duan, E. Demler and M. D. Lukin, *Phys. Rev. Lett.* **91** (Aug, 2003) 090402.

[79] O. F. Syljuåsen and A. W. Sandvik, *Phys. Rev. E* **66** (Oct, 2002) 046701.

[80] O. F. Syljuåsen, *Phys. Rev. E* **67** (Apr, 2003) 046701.

[81] H. Y. Hwang, Y. Iwasa, M. Kawasaki, B. Keimer, N. Nagaosa and Y. Tokura, *Nat Mater* **11** (Feb, 2012) 103–113.

[82] T. Hotta, *Reports on Progress in Physics* **69** (2006) 2061.

[83] A. Lanzara, P. V. Bogdanov, X. J. Zhou, S. A. Kellar, D. L. Feng, E. D. Lu et al., *Nature* **412** (Aug, 2001) 510–514.

[84] G.-H. Gweon, T. Sasagawa, S. Y. Zhou, J. Graf, H. Takagi, D.-H. Lee et al., *Nature* **430** (Jul, 2004) 187–190.

[85] A. Damascelli, Z. Hussain and Z.-X. Shen, *Rev. Mod. Phys.* **75** (Apr, 2003) 473–541.

[86] A. Lanzara, N. L. Saini, M. Brunelli, F. Natali, A. Bianconi, P. G. Radaelli et al., *Phys. Rev. Lett.* **81** (Jul, 1998) 878–881.

[87] A. J. Millis, P. B. Littlewood and B. I. Shraiman, *Phys. Rev. Lett.* **74** (Jun, 1995) 5144–5147.

[88] F. Massee, S. de Jong, Y. Huang, W. K. Siu, I. Santoso, A. Mans et al., *Nature Physics* **7** (Sep, 2011) 978–982.

[89] M. E. Fisher, M. N. Barber and D. Jasnow, *Phys. Rev. A* **8** (Aug, 1973) 1111–1124.

[90] M. Berciu, *Phys. Rev. Lett.* **107** (Dec, 2011) 246403.

[91] A. Lenard, *Journal of Mathematical Physics* **5** (1964) 930–943.

[92] M. Rigol and A. Muramatsu, *Phys. Rev. A* **72** (Jul, 2005) 013604.

[93] C. K. Majumdar and D. K. Ghosh, *Journal of Mathematical Physics* **10** (1969) 1388–1398.

[94] C. K. Majumdar, *Journal of Physics C: Solid State Physics* **3** (1970) 911.

[95] W. P. Su, J. R. Schrieffer and A. J. Heeger, *Phys. Rev. Lett.* **42** (Jun, 1979) 1698–1701.

[96] W. P. Su, J. R. Schrieffer and A. J. Heeger, *Phys. Rev. B* **22** (Aug, 1980) 2099–2111.

[97] D. Rossini, V. Lante, A. Parola and F. Becca, *Phys. Rev. B* **83** (Apr, 2011) 155106.

[98] J. Struck, C. Ölschläger, R. Le Targat, P. Soltan-Panahi, A. Eckardt, M. Lewenstein et al., *Science* **333** (2011) 996–999.

[99] T. Mishra, R. V. Pai, S. Mukerjee and A. Paramekanti, *Phys. Rev. B* **87** (May, 2013) 174504.

[100] J. Chakhalian, A. J. Millis and J. Rondinelli, *Nature Materials* **11** (Jan, 2012) 92–94.

[101] A. Y. Ganin, Y. Takabayashi, P. Jeglic, D. Arcon, A. Potocnik, P. J. Baker et al., *Nature* **466** (May, 2010) 221–225.

[102] M. Capone, M. Fabrizio, C. Castellani and E. Tosatti, *Rev. Mod. Phys.* **81** (Jun, 2009) 943–958.

[103] O. Gunnarsson, *Rev. Mod. Phys.* **69** (Apr, 1997) 575–606.

[104] T. Hotta and E. Dagotto, *Phys. Rev. Lett.* **92** (Jun, 2004) 227201.

[105] S. Yamamoto, T. Fujiwara and Y. Hatsugai, *Phys. Rev. B* **76** (Oct, 2007) 165114.

[106] K. Rociszewski and A. M. Oleś, *Journal of Physics: Condensed Matter* **23** (2011) 265601.

[107] A. Ghosh and S. Yarlagadda*(unpublished)* .

[108] *In one dimension, it has been shown in Ref. [40] that $t_2 - V_1$ model yields a cSS. In 2D, it has been demonstrated in Ref. [20] that $t_2 - t_3 - V_1$ model generates a cSS; using similar logic, it can be shown that $t_2 - V_1$ model also manifests cSS.* .

[109] P. B. Allen and V. Perebeinos, *Phys. Rev. B* **60** (Oct, 1999) 10747–10753.

[110] I. Lang and Y. A. Firsov, *Sov. Phys. JETP* **16** (1963) 1301.

[111] A. Dey, M. Q. Lone and S. Yarlagadda, *Phys. Rev. B* **92** (Sep, 2015) 094302.

[112] A. W. Sandvik, *AIP Conference Proceedings* **1297** (2010) 135–338.

[113] G. G. Batrouni, R. T. Scalettar, G. T. Zimanyi and A. P. Kampf, *Phys. Rev. Lett.* **74** (Mar, 1995) 2527–2530.

[114] O. Nguyen and L. Dang, *The European Physical Journal B* **90** (Apr, 2017) 71.

[115] A. Kuklov, N. Prokof'ev and B. Svistunov, *Phys. Rev. Lett.* **93** (Nov, 2004) 230402.

[116] S. Wessel, *Phys. Rev. B* **86** (Oct, 2012) 140501.

[117] *The nature of the special points (i.e., whether they represent triple points, etc.) needs further investigation.* .

[118] R. J. Cava, B. Batlogg, T. T. Palstra, J. J. Krajewski, W. F. Peck, A. P. Ramirez et al., *Phys. Rev. B* **43** (Jan, 1991) 1229–1232.

[119] T. Katsufuji, T. Tanabe, T. Ishikawa, S. Yamanouchi, Y. Tokura, T. Kakeshita et al., *Phys. Rev. B* **60** (Aug, 1999) R5097–R5100.

[120] I. A. Zaliznyak, J. P. Hill, J. M. Tranquada, R. Erwin and Y. Moritomo, *Phys. Rev. Lett.* **85** (Nov, 2000) 4353–4356.

[121] M. Cwik, M. Benomar, T. Finger, Y. Sidis, D. Senff, M. Reuther et al., *Phys. Rev. Lett.* **102** (Feb, 2009) 057201.

[122] A. T. Boothroyd, P. Babkevich, D. Prabhakaran and P. G. Freeman, *Nature* **471** (Mar, 2011) 341–344.

[123] E. C. Andrade and M. Vojta, *Phys. Rev. Lett.* **109** (Oct, 2012) 147201.

[124] T. Lancaster, S. R. Giblin, G. Allodi, S. Bordignon, M. Mazzani, R. De Renzi et al., *Phys. Rev. B* **89** (Jan, 2014) 020405.

[125] N. Hollmann, M. W. Haverkort, M. Cwik, M. Benomar, M. Reuther, A. Tanaka et al., *New Journal of Physics* **10** (2008) 023018.

[126] J. E. Hirsch and E. Fradkin, *Phys. Rev. B* **27** (Apr, 1983) 4302–4316.

[127] J. E. Hirsch, *Phys. Rev. B* **31** (May, 1985) 6022–6031.

[128] E. Berger, P. Valášek and W. von der Linden, *Phys. Rev. B* **52** (Aug, 1995) 4806–4814.

[129] Z. B. Huang, W. Hanke, E. Arrigoni and D. J. Scalapino, *Phys. Rev. B* **68** (Dec, 2003) 220507.

[130] R. P. Hardikar and R. T. Clay, *Phys. Rev. B* **75** (Jun, 2007) 245103.

[131] A. Macridin, G. A. Sawatzky and M. Jarrell, *Phys. Rev. B* **69** (Jun, 2004) 245111.

[132] A. Dobry, A. Greco, J. Lorenzana and J. Riera, *Phys. Rev. B* **49** (Jan, 1994) 505–513.

[133] A. Dobry, A. Greco, J. Lorenzana, J. Riera and H. T. Diep, *EPL (Europhysics Letters)* **27** (1994) 617.

[134] B. Bäuml, G. Wellein and H. Fehske, *Phys. Rev. B* **58** (Aug, 1998) 3663–3676.

[135] M. Tezuka, R. Arita and H. Aoki, *Phys. Rev. B* **76** (Oct, 2007) 155114.

[136] S. Sota and T. Tohyama, *Phys. Rev. B* **82** (Nov, 2010) 195130.

[137] J. K. Freericks and M. Jarrell, *Phys. Rev. Lett.* **75** (Sep, 1995) 2570–2573.

[138] M. Capone, G. Sangiovanni, C. Castellani, C. Di Castro and M. Grilli, *Phys. Rev. Lett.* **92** (Mar, 2004) 106401.

[139] W. Koller, D. Meyer, Y. no and A. C. Hewson, *EPL (Europhysics Letters)* **66** (2004) 559.

[140] W. Koller, D. Meyer and A. C. Hewson, *Phys. Rev. B* **70** (Oct, 2004) 155103.

[141] G. S. Jeon, T.-H. Park, J. H. Han, H. C. Lee and H.-Y. Choi, *Phys. Rev. B* **70** (Sep, 2004) 125114.

[142] G. Sangiovanni, M. Capone, C. Castellani and M. Grilli, *Phys. Rev. Lett.* **94** (Jan, 2005) 026401.

[143] G. Sangiovanni, M. Capone and C. Castellani, *Phys. Rev. B* **73** (Apr, 2006) 165123.

[144] J. Bauer and A. C. Hewson, *Phys. Rev. B* **81** (Jun, 2010) 235113.

[145] J. Bauer and G. Sangiovanni, *Phys. Rev. B* **82** (Nov, 2010) 184535.

[146] M. Grilli and C. Castellani, *Phys. Rev. B* **50** (Dec, 1994) 16880–16898.

[147] J. Keller, C. Leal and F. Forsthofer, *Physica B: Condensed Matter* **206-207** (1995) 739 – 741.

[148] E. Koch and R. Zeyher, *Phys. Rev. B* **70** (Sep, 2004) 094510.

[149] U. Trapper, H. Fehske, M. Deeg and H. Büttner, *Zeitschrift für Physik B Condensed Matter* **93** (Dec, 1994) 465–478.

[150] C. A. Perroni, V. Cataudella, G. De Filippis and V. M. Ramaglia, *Phys. Rev. B* **71** (Mar, 2005) 113107.

[151] Y. Takada and A. Chatterjee, *Phys. Rev. B* **67** (Feb, 2003) 081102.

[152] H. Fehske, D. Ihle, J. Loos, U. Trapper and H. Büttner, *Zeitschrift für Physik B Condensed Matter* **94** (Mar, 1994) 91–100.

[153] R. Zeyher and M. L. Kulić, *Phys. Rev. B* **53** (Feb, 1996) 2850–2862.

[154] A. Di Ciolo, J. Lorenzana, M. Grilli and G. Seibold, *Phys. Rev. B* **79** (Feb, 2009) 085101.

[155] P. Barone, R. Raimondi, M. Capone, C. Castellani and M. Fabrizio, *Phys. Rev. B* **77** (Jun, 2008) 235115.

[156] A. Payeur and D. Sénéchal, *Phys. Rev. B* **83** (Jan, 2011) 033104.

[157] *A half-filled Hubbard-Holstein model on a two-dimensional square lattice, where the Coulomb interaction was treated in terms of static-auxiliary fields and the phonons were considered in the adiabatic limit, was studied in Ref. [159] .*

[158] *For a lucid treatment of the electronic interaction using static-auxiliary fields and the phonons using the adiabatic limit, see Refs. [164] and [165] .*

[159] S. Pradhan and G. V. Pai, *Phys. Rev. B* **92** (Oct, 2015) 165124.

[160] T. Barnes and E. S. Swanson, *Phys. Rev. B* **37** (Jun, 1988) 9405–9409.

[161] I. Bose, *Current Science* **88** (2005) 62–70.

[162] A. Sen, K. Damle and T. Senthil, *Phys. Rev. B* **76** (Dec, 2007) 235107.

[163] S. Wessel, *Phys. Rev. B* **78** (Aug, 2008) 075112.

[164] R. Tiwari and P. Majumdar, *EPL (Europhysics Letters)* **108** (2014) 27007.

[165] S. Kumar and P. Majumdar, *The European Physical Journal B - Condensed Matter and Complex Systems* **50** (Apr, 2006) 571–579.